HYPERSPECTRAL ASSESSMENT OF *Acer saccharum* FOREST STRUCTURE

by

VALERIE ANNE THOMAS

A thesis submitted to the Department of Geography
in conformity with the requirements for
the degree of Master of Science

Queen's University
Kingston, Ontario, Canada
December, 2001

ABSTRACT

Hyperspectral remote sensing potentially allows for the development of image processing techniques that could be applied over large areas to assess forest condition. Current hyperspectral research for forestry tends to focus on deriving and modelling plant physiological responses. Structural information is typically derived from a very different type of image processing, using spatial techniques on high spatial resolution data. This research involved the incorporation of hyperspectral and spatial processing techniques to derive structural indices from Compact Airborne Spectrographic Imager (CASI) hyperspectral data that were correlated with structural characteristics of sugar maple stands.

Data collection for this work involved a field campaign to characterize the stand and canopy structure of selected sugar maple stands in southeastern and central Ontario. These stands covered a variety of canopy conditions ranging from varied silviculture treatments applied in the Algoma region of central Ontario to various levels of damage resulting from the 1998 ice storm in eastern Ontario. Hyperspectral CASI reflectance data were collected for these areas in 1998 and 2000 respectively.

Hyperspectral image processing involved the calculation of first- and second-derivative images from the reflectance data and subsequent semivariogram analysis to characterize range and anisotropic information for each calibration site. These range values were used to derive texture features from the reflectance and derivative data. Correlation analysis was used to identify spectral, derivative, and texture indices that

were correlated to ground-based structural metrics. Indices that showed strong correlations were then applied to validation sites to assess robustness.

Results illustrate that the integration of spatial and hyperspectral techniques improve the relationships with ground-based structural metrics over what could be derived using either technique alone for these data. For example, a dissimilarity texture index applied to the second derivative of the 505 nm channel has strong correlations with percent canopy openness (significant at 95% confidence intervals) at the calibration sites ($r=0.83$) and the control sites in the validation study area ($r=0.82$). By identifying correlation patterns on the spectral and derivative curves (a technique that is not possible with multispectral data), it has been demonstrated that hyperspectral data has unique and valuable information to add to remote sensing of forest structure.

Acer saccharum,

You reach up to the sky and release the breath of life through your open arms.
It grieves me that we butcher you, we carelessly poison you, slowly eliminate you.
How poorly we understand you.

Whisper the secrets of centuries through your leaves. I am listening.
Have patience, gentle ones, as I struggle with your lessons.
I will not abandon you. I am your sister.

V. Thomas
August 19, 2000

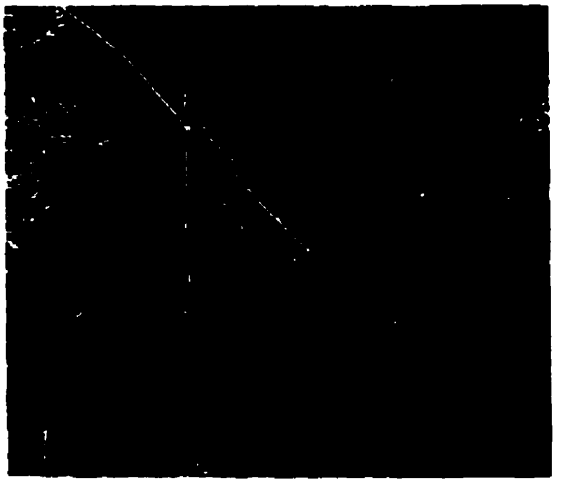

ACKNOWLEDGEMENTS

I would like to extend my heart-felt appreciation to my supervisor, Dr. Paul Treitz. Paul's encouragement and enthusiasm for my work, and in remote sensing in general, has been a remarkable source of inspiration. Thank-you, Paul.

I want thank Dr. Dennis Jelinski for sharing advice and insights about landscape ecology and the environment, as well as for serving on my committee. Thanks also to Dr. Harry McCaughey, and Dr. Lonnie Aarssen for their participation on the examining committee. To the people in the Department of Geography at Queen's University I would like to acknowledge the friendly and supportive atmosphere you have created. My life has been enriched by my experience here.

For assistance with field site selection and sampling I want to thank: Craig Sheriff; Bjorn Prenzel; David Mazzucchi; Christine McLeod; Paul Sampson; Driss Haboudane; Geoff McVey; Tom Noland; Gina Mohammed; Kevin Lim; Brandon Beierle; Ken Baldwin; and Denzil Irving. For CASI data planning and acquisition, I want to thank: John Miller; Pablo Zarco-Tejada; Jim Freemantle; Lawrence Gray; Paul Shepherd; Phil Brasher; and Heidi Beck. I would also like to gratefully acknowledge the financial support provided for this research through: Geomatics for Informed Decisions (GEOIDE) - A Canadian Centre of Excellence; the Centre for Research in Earth and Space Technologies (CRESTech) - a Provincial Centre of Excellence; the Ontario Ministry of Natural Resources; and a Natural Sciences and Engineering Research (NSERC) Operating Grant to Paul Treitz.

Finally, I owe more than I can ever say to my family and friends. I love you all. I would like to thank Jen, Nicole, and Bob for showing me by example how to be a better person. Mom, Dad, Rocky, Dee, and Patti - you have been the source of my strength for my entire life.

TABLE OF CONTENTS

LIST OF TABLES

LIST OF FIGURES

1.0 INTRODUCTION

There are approximately 418 million hectares of forest in Canada, almost half of this nation's land mass. Maintaining the sustainability, biodiversity, and long-term health of Canada's forests through effective management is a subject of interest for a variety of groups, including the federal and provincial governments, industry, environmental groups, and the Canadian public in general. *The National Forest Strategy (1998-2003) – Sustainable Forests: A Canadian Commitment* (Canadian Council of Forest Ministers (CCFM), 1998) identified the need for a national framework of criteria and indicators for sustainable forest management. This has been extended to the forest industry in Ontario, through the Crown Forest Sustainability Act, 1994 and the Policy Framework for Sustainable Forests (Ontario Ministry of Natural Resources (OMNR), 1998); which require that Crown forests be managed in a way that will meet the social, economic, and environmental needs of both present and future generations. In 1999, a strong emphasis was placed on intensive silvicultural treatment practices, with recommendations put forward in Canada's Senate Subcommittee Report on the boreal forest and in Ontario's Living Legacy (Taylor, 1999; OMNR, 1999; Lautenschlager, 2000). Unfortunately, current limitations in field survey techniques with regards to high costs, subjectivity, and low spatial and temporal coverage severely limit decision making by forest resource managers. Remote sensing and related technologies offer significant potential for classification and monitoring of ecosystem classes, and the estimation of ecological/biophysical parameters at multiple scales. This increases the ability of foresters to consider the emerging concepts of landscape ecology when adopting management strategies, and to research the importance of spatial arrangements of forests

and processes within them for the functioning of organisms, groups, and ecosystems (Farina, 1998).

There are several definitions of landscapes and numerous disciplines have adopted the concepts of landscape ecology in an attempt to understand some of the complex spatial interactions of life on Earth. Haber (in Farina, 1998, p. 2) came up with a general definition of the landscape as "a piece of land which we perceive comprehensively around us, without looking closely at single components, and which looks familiar to us." This broad definition of a landscape (i.e., based on perception) is suitable for remote sensing research, since the whole field of remote sensing is based on obtaining different views or perceptions of the surface of the earth. Without the use of remote sensing, human perception of the landscape is restricted to that which can be viewed from the ground. Foresters survey field sites containing what they perceive to be a reasonably homogeneous assemblage of plants to obtain average measurements for the area. They then extrapolate to the larger surrounding area assuming that their definition of homogeneity is maintained and that the larger area can be considered as a unit or stand. Remote sensing has opened the door to allow the study of the forest ecosystem at many levels, and to extend our perception of the forest landscape to regional, provincial, national, and even global spatial scales. The potential for monitoring process and function within the landscape at various temporal (and spatial) scales has also been greatly enhanced with this technology. This is particularly true of spaceborne sensors, which can provide continuous coverage of large portions of the Earth's surface.

Currently in the remote sensing community there is a divided research focus on the potential of very high spatial and spectral (hyperspectral) resolution data for the

analysis of forest ecosytems in terms of structural and physiological response. The majority of current hyperspectral research focuses on deriving and modelling plant physiological characteristics and responses. This is typically done at the laboratory/leaf scale and is often "upscaled" to the canopy level using a variety of geometric-optical canopy reflectance modelling techniques (Zarco-Tejada *et al.*, 1999; Peddle and Johnson, 2000). In this manner, the goal of many research initiatives is to relate quantifiable leaf-scale spectral response to the spectral reflectance captured at the airborne/canopy scales. The driving goal behind typical hyperspectral research is to eventually move to satellite platforms, without losing the integrity of detailed physiological information available at the laboratory/leaf scale. Structural information, on the other hand, is typically derived from spatial information available at high resolution airborne or satellite platforms, with less consideration given to detailed spectral response. In this scenario, the focus has been on spatial patterns within the image, often incorporating texture, geostatistics, or component fraction techniques in an attempt to quantify the spatial arrangement and pattern of the landscape.

With current technology, most hyperspectral data is obtained using airborne platforms. A hyperspectral data cube contains information both on the detailed physiological canopy response and the spatial patterns and variations of canopy spectra. However, the potential benefits of having detailed spectral information to supplement high spatial resolution data have been largely ignored for structural research. There has been little work done towards the integration of spatial and hyperspectral techniques for the extraction of structural information. The focus of this research has been on the

integration of hyperspectral and spatial techniques to extract spectral derivatives over spatial extents that quantify structural information about the forest canopy.

Research questions on forest physiology and structure can be addressed by hyperspectral remote sensing through the analysis of the electromagnetic response that is captured by the sensor. The interaction between electromagnetic energy and the leaf has been studied at both the laboratory and canopy scales for physiological research. Relationships between the first and second derivatives of the spectral curve and cellular biochemical processes have been established (i.e., Belanger, *et al.* 1995; Zarco-Tejada and Miller, 1999; Treitz and Howarth, 1999; Sampson, 2000). By assessing the spatial distribution and pattern of these processes as well as the pattern of shadow and gaps in the canopy, this research relates the electromagnetic response to forest structure.

1.1 Hypothesis

It is hypothesized that there are quantifiable relationships between the spatial distribution of hyperspectral response measured at airborne scales and ground-based biophysical variables measured at the stand level. By incorporating both hyperspectral and spatial techniques, structural indices can be derived from airborne hyperspectral data to estimate biophysical characteristics of sugar maple stands.

1.2 Objectives

To test the stated hypothesis, the following research objectives were addressed:

1. to develop a digital database of stand structural data for control sites and those that have undergone natural or silvicultural-induced change;

2. to explore the use of hyperspectral image processing techniques, geostatistics and texture analysis for identifying relationships between airborne hyperspectral data and ground-based data; and
3. to derive empirical indices that are correlated with sugar maple biophysical characteristics and demonstrate potential for predicting forest structural parameters.

1.3 Study Sites

Ideally, in order to assess the utility of hyperspectral data for the monitoring of forest biophysical parameters, one would hope to study the relationships under varying structural conditions. In practice, this is quite difficult to achieve, since scientists are often constrained to the forest conditions that exist at their study site at the time the remote sensing data are collected. However, for this study, a unique opportunity existed to access a range of forest structural conditions for sugar maple stands throughout Ontario. Various sugar maple canopy structural conditions resulting from differing silviculture treatment practices were available for study at the Turkey Lakes Watershed study area north of Sault Ste. Marie. In addition, the destructive 1998 ice storm that affected large portions of eastern Ontario and southern Quebec provided a range of natural occurring structural changes to sugar maple canopies. Finally, sugar maple stands in central Ontario were studied. These had not been logged and were located outside the area of damage from the 1998 ice storm. Combined, these sites encompassed the range of canopy structural conditions most likely to be found in Ontario's sugar maple stands. This provided a comprehensive "testing ground" for the utility of hyperspectral remote

sensing for the monitoring of forest biophysical parameters. The approximate locations of the study sites within Ontario are shown in Figure 1.

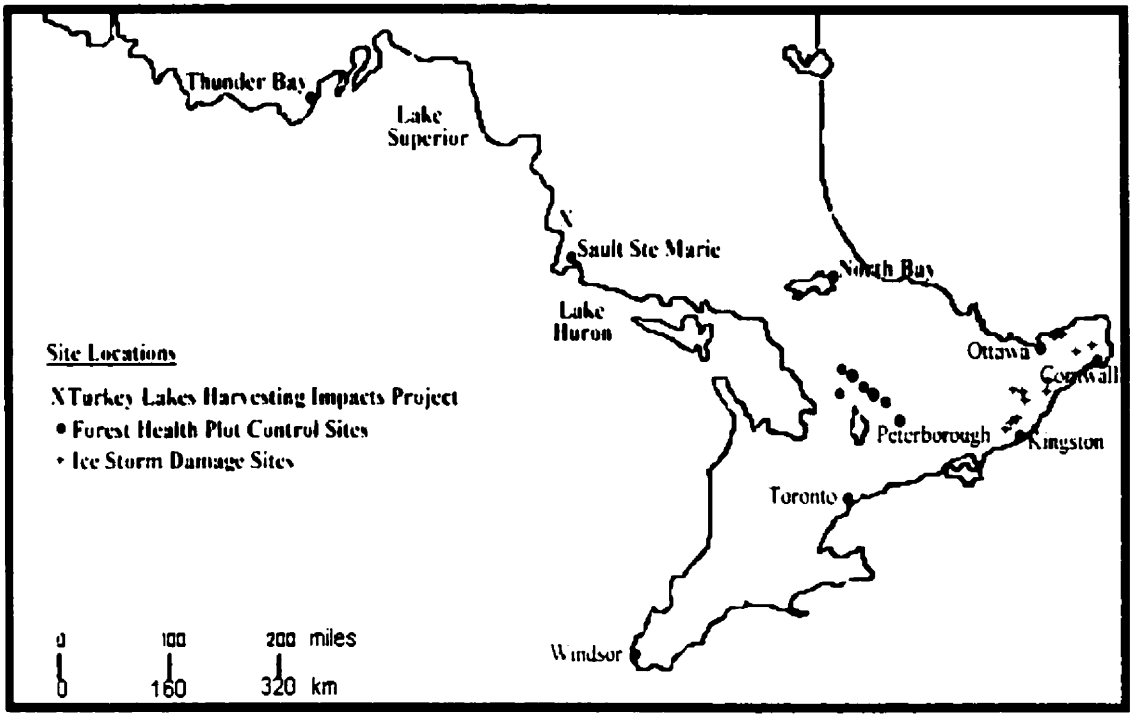

Figure 1: Locations Of Study Sites Used For Calibration (Index Development) And Validation

1.3.1 Calibration Sites

Calibration sites included unmanaged sites (that were used as controls in the development of indices) and managed sites that were damaged by the 1998 ice storm (used as damaged sites for the development of indices). These sites were all selected from previously studied forest plots set up by the Ontario Forest Research Institute (OFRI). In 1996, OFRI created the Bioindicators of Forest Condition Project to "develop a Forest Condition Rating (FCR) System to classify condition on a quantitative scale from healthy to stressed, relative to an acceptable range of values" (Sampson, 2000, p.1). This was an interdisciplinary project that involved the use of remote sensing and ground-

based measurements of structural and physiological components of forest condition. One of the aims of the project was to use airborne hyperspectral remote sensing to overcome the conventional labour-intensive approach required to measure the physiological response of individual trees. As part of the Bioindicators of Forest Condition Project, multiple sites were selected across Ontario that covered a range of canopy conditions, including sites damaged by the 1998 ice storm. The goal was to collect hyperspectral data in the summer of 2000, which would correspond to a field campaign to characterize physiological response. Through cooperation with OFRI, a concurrent field campaign was designed to characterize the ground-based structural parameters for these sites. OFRI then provided hyperspectral data for consideration of structural conditions.

1.3.1.1 1998 Ice Storm Damage (ISD) Sites

The ice storm of January 5-10, 1998 was one of the most destructive natural disturbances ever recorded in North America (Lautenschlager and Nielson, 1999). Throughout the St. Lawrence and Ottawa River valleys, as well as upstate New York, parts of New England, and the Maritimes, extended periods of supercooled rain, which froze on contact, caused extensive damage to the forest canopy (Lautenschlager and Nielsen, 1999). Since that time, a variety of short- and long-term socio-economic and ecological concerns have been raised about dealing with the loss and damage caused by the storm, as well as preventing future damage caused by similar storms.

The sugar maple stands in this area were severely damaged by the storm, resulting in considerable effort being placed on understanding the impacts of the storm on the production of maple syrup. In 1998, the Ontario Ministry of Natural Resources (OMNR)

assessed and categorized the damage of the ice storm to sugar maple stands privately owned by maple syrup producers. Depending on the extent of the structural damage, each location was categorized as having light, moderate, or severe damage. An interdisciplinary sugar maple study was then established to:

> "document how tapping effects sugar maple recovery probabilities; the potential of cost-effective remedial treatments to speed recovery of, and mitigate further damage to sugar maple stands; the effects of damage and potential remedial treatments on sap production (volume and sweetness); and some ecological consequences of damage and potential remedial treatments (Lautenschlager and Nielson, 1999, p.636)."

The experiment consisted of 35 one-hectare plots on privately owned maple syrup farms that accounted for the range of canopy damage classes. Each plot was 100 m x 100 m, divided into 50 m x 50 m quadrants. The quadrants were used to test the effect of remedial fertilizer treatments, including: 1) no treatment; 2) the addition of phosphorus and potassium; 3) the addition of lime and magnesium; and 4) the addition of phosphorus, potassium, lime, and magnesium (Lautenschlager and Nielson, 1999).

Of these 35 plots, twelve were selected for the Bioindicators of Forest Condition Project for the airborne hyperspectral mission (Figure 1). These plots covered the entire range of canopy damage as assessed by the OMNR, with four plots in each category of low, moderate, and severe damage. Stand structural data were collected for each of these twelve plots in June and July of 2000. The hyperspectral data for these plots were collected in July, 2000. Due to poor flight conditions, two of the original twelve plots were dropped from the mission, leaving ten ISD plots for the development of structural indices.

1.3.1.2 Forest Health (FH) Sites

In 1985, a network of over 100 permanent hardwood Forest Health (FH) sites (each containing a 60 m x 60 m plot) was established by the Ontario Ministry of the Environment and Energy (OMEE), whose purpose was to assess acid rain and low-level ozone damage to stands throughout Ontario (Sampson *et al.*, 2000). Annual assessments of these stands were completed to develop a historical database of crown condition in the form of a Decline Index (DI). This index incorporated information on proportion of dead branches in the canopy with chlorosis information to calculate a numerical value used to categorize crown damage as low, moderate, or severe (Sampson *et al.*, 2000). The DI values were used to select six hardwood FH plots that covered a range of canopy conditions. These six sugar maple stands were not used for the production of maple syrup and were located outside of the area affected by the 1998 ice storm (Figure 1). For the purpose of this research, they served as control or "natural" condition sites for the development of structural indices.

1.3.2 Validation Site

1.3.2.1 Turkey Lakes Harvesting Impacts Project

The Turkey Lakes watershed (TLW) is located in the southern portion of the Boreal Shield Ecozone, approximately 60 km north of Sault Ste. Marie, Ontario. Characteristic tree species in the area include sugar maple (*Acer saccharum* Marsh.), yellow birch (*Betula allegheniensis* Arnold), red maple (*Acer rubrum* L.), white spruce (*Picea glauca*), ironwood (*Ostrya virginiana*), balsam fir (*Abies balsamea*), and eastern white cedar (*Thuja occidentalis*) (Natural Resources Canada (NRCan), 1998). The forest

in this watershed consists of tolerant hardwoods that have in the past been high-graded for quality logs, resulting in a present day forest that is "an uneven-aged, generally mature-to-overmature, old growth tolerant community. ...The percentage composition of *Acer spp.* and *Betula spp.* is quite high (ca. >90% in total) (Sampson, 2000, p.33)." The topography in this area of the Algoma Region is rugged, with shallow, Precambrian-derived till soil (NRCan, 1998).

In 1979, a 1000 ha study area was established in the TLW by the Canadian Forest Service (CFS) and other interest groups as part of a project to study the impacts of the long-range transport of air pollutants on aquatic and terrestrial ecosystems (NRCan, 1998). Emerging from this project in 1997, the Turkey Lakes Harvesting Impacts Project (TLHIP) was developed for the lower part of the watershed "to examine the impacts of harvesting practices on the ecosystem and to calibrate a range of harvesting prescriptions to this important forest type" (NRCan, 1998, http://www.glfc.forestry.ca/index-en/research-e/forest_ecology-e/turkeylakes-e.html). In particular, the TLHIP was designed to study the effects of human induced variations to the light regime, which is a dominant growing force in closed canopy forest environments. As stated by NRCan (1998; http://www.glfc.forestry.ca/index-en/research-e/forest_ecology-e/turkeylakes-e.html), "any disturbance process that increases light penetration sets off a chain of events, many of them interrelated, that change the structure, composition, function and process within the stand."

The TLHIP sites consisted of four silviculture treatment methods; control, selected cut, shelterwood, and clear cut. Control sites were untreated in the experiment, and consist of old-growth closed-canopy conditions. The selected cut (also referred to as

selection) treatment is a system in which individual trees are selected and removed over a large area, resulting in an uneven-aged stand. This system tends to be more common on productive logging sites (Sampson, 2000). Shelterwood harvesting involves two or more successive cuts which provide a source of protection and seed for regeneration. This results in an even-aged stand, and tends to be more common on less productive sites (Sampson, 2000). For this experiment, only the first cut had been made, meaning that the shelterwood and selected cut sites would have very similar characteristics. Clear cut harvesting involved the removal of most or all stems, in this case everything with a diameter greater than 10 centimeters. Obviously this is not the preferred harvesting method if the goal is to achieve a sustainable forest management practice. However, for the purpose of the TLHIP, it served as the maximum site disturbance, with almost complete canopy removal. For this research, 36 plots with an 11.3 m radius were sampled within the TLW. The layout of the sample plots within the TLHIP site is illustrated in Figure 2. These plots were used for validation (i.e., to test the robustness of the derived indices on an independent dataset with different structural conditions in the canopy).

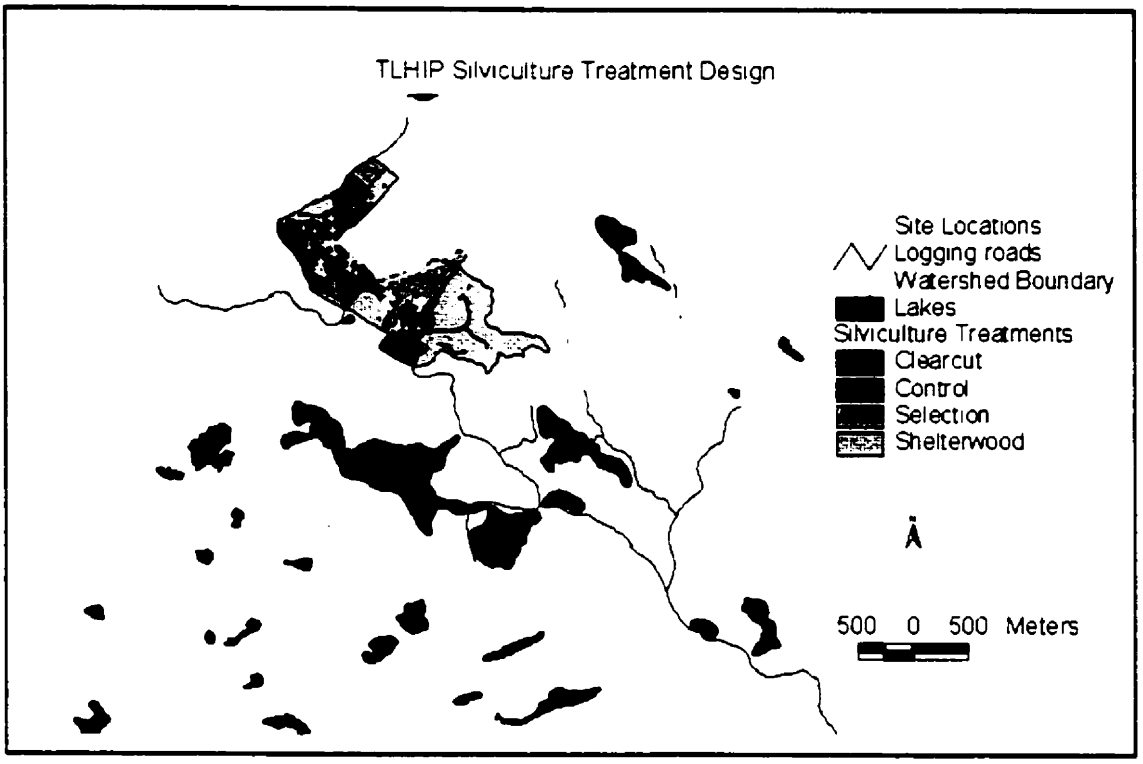

Figure 2: Validation Plots Within TLHIP Site

1.4 Thesis Outline

This research consists of four main components: 1) a comprehensive literature search to determine the current state of research regarding hyperspectral remote sensing of forest biophysical parameters; 2) an intensive field campaign to characterize the forest biophysical parameters for the identified study site; 3) compilation of a digital database containing the raw field data as well as calculated metrics; and 4) an image processing phase used to relate the field parameters to the airborne hyperspectral data and various derivatives/indices. The key information derived from the literature review is presented in Chapter 2. Methods utilized for the field campaign, digital database compilation, and image processing are presented in Chapter 3, followed by a presentation of major results in Chapter 4. A discussion of these results and their implications for remote sensing of

forest ecosystems is presented in Chapter 5. Finally, the major conclusions drawn from this work and recommendations for future research are presented in Chapter 6.

2.0 BACKGROUND

Before discussing some of the issues that have arisen around hyperspectral remote sensing and its potential for monitoring forest structure, it may prove useful to briefly examine how hyperspectral remote sensing fits within the context of remote sensing in general, and why it has generated such interest for forest ecosystem monitoring.

Lillesand and Kiefer (1994, p.1) define remote sensing as:

> *"the science and art of obtaining information about an object, area, or phenomenon through the analysis of data acquired by a device that is not in contact with the object, area, or phenomenon under investigation."*

This includes the collection of any form of data, with common types including force, acoustics, and electromagnetic (EM) energy. The research for this thesis concerns the collection of EM energy for the purpose of monitoring the Earth's surface, in particular forest ecosystems. With such a broad definition, it becomes apparent that various aspects of remote sensing science and the study of EM energy can be traced throughout human history, perhaps as far back as ancient Greek civilization. As early as 300 BC, Aristotle theorized about the nature of light and the transparency of certain objects in its presence (Estes, 1997). Remote sensing using EM energy has existed since the evolution of vision, which is simply a way for the body to sense EM energy in the visible portion of the EM spectrum, convert this energy into signals for the brain, and process these signals to allow humans and animals to study their surroundings.

Recent technological advances have allowed for the study of EM energy outside the visible range, through the use of such devices as spectroradiometers, sonar, radar, etc. As early as the 1950's, multispectral sensor technology allowed for the relatively crude

spectral characterization of reflected and emitted EM energy (Estes, 1997). These sensors collected digital imagery in 3 to 10 spectral bands, each of which contained broad averages of EM energy (bandwidths of approximately 70-400 nm). Multispectral satellites were launched in the 1960's and 1970's, with rapid progress made in the development of analytical techniques for the image data collected (Landgrebe, 1998). Earth scientists have found multispectral remote sensing useful for a variety of applications, including forestry, agriculture, geology, oceanology – essentially any application that could benefit from monitoring the landscape from different perspectives (and scales) than is possible with human vision at the ground level.

Since the 1980's, the development of airborne hyperspectral sensors has allowed for the shift from the analysis of a few broad bands of noncontiguous, multispectral imagery to the more complex reflectance spectroscopy (Goetz *et al.*, 1985; Vane *et al.*, 1993, Landgrebe, 1998; Clark, 1999). Imaging spectroscopy has been performed in a laboratory setting for the past 100 years, and can be defined as the study of reflected or scattered light as a function of wavelength through use of a spectrometer (Clark, 1999). In this sense, a hyperspectral remote sensing scanner is a special type of multispectral scanner that records many bands of imagery at very narrow bandwidths. To create an image, multiple spectrometers are aligned in an array to cover a ground area, creating a recognizable image at any one spectral wavelength. This allows the spatial information to be collected in the x-y dimension, with spectral information contained in the z dimension, forming what is referred to as a data cube.

There are usually around 100 to 300 spectral bands of relatively narrow bandwidths (i.e., 5-10 nm) in a hyperspectral dataset. Compared to the earth monitoring

remote sensing platforms developed prior to hyperspectral sensors, this represents a dramatic increase in the amount and detail of spectral information available for any given location on the surface of the earth. It has allowed for the generation of a spectral signature for a given location, compared to the broad approximation based on the few bands in a traditional multispectral sensor.

There are distinct advantages associated with hyperspectral data that have been observed in the laboratory setting for some time. With a more complete spectral signature, it is possible to identify different groups of materials on the Earth's surface based on their characteristic spectral response and, in many cases, it is possible to determine the identity of individual members of such groups. Individual materials that occur within a class (for example, specific minerals within a broader mineral group or individual species of trees within a forest) often express their variations in composition as slight shifts in the peaks and troughs within the spectral curve continuum. In addition, hyperspectral sensors have the ability to detect very subtle changes in the spectral response of an object over time. This has led to considerable research into the utility of hyperspectral remote sensing for the detection of vegetative stress and the eventual detailed monitoring of vegetative health from satellite platforms.

Progress in the analysis of hyperspectral data has not been as rapid or successful as originally anticipated (Landgrebe, 1998). This has been due to a variety of factors, which relate to the size and complexity of hyperspectral datasets, limitations in computer processing capabilities, environmental conditions introducing noise, and the sensitivity of surface materials to environmental conditions causing variations in spectral reflectance. To cover the same spatial extent as would be seen with a multispectral scanner, the

datasets become very large, requiring the development of new processing techniques. Ironically, most of these techniques have focused on extracting the most appropriate wavelength ranges for a particular study, in order to eliminate redundant or less useful bands. This then allows for analyses using processing techniques developed for multipspectral data.

There are further complexities introduced when attempting to study vegetated environments. Within-species reflectance from a vegetated surface will vary depending on season, illumination, nutrient regime, availability of water, etc. Some studies have illustrated that despite the original expectations of many remote sensing scientists, it has not been possible to uniquely identify and separate all vegetative species (Hoffbeck and Landgrebe, 1996), mainly due to the variability of vegetative response across space and time. In response to the potentials and problems outlined above, hyperspectral research with regards to vegetation analysis has been narrowly focused on deriving and modelling plant physiological responses. This has been done by examining subtle variations in the spectral signature and developing very specialized spectral indices. The complexities introduced by the examination of structural information, which is a spatial phenomenon, have curtailed research in this area. Research towards the utility of hyperspectral data for the extraction of structural information for a forest ecosystem, specifically sugar maple forest, has been largely unexamined to date and is the focus of this research.

2.1 Spectral and Hyperspectral Techniques

Spectral indices are transformations applied to image data, including ratios and linear/nonlinear band combinations, specifically designed to enhance some aspect of the

reflectance surface (Jensen, 1996). Govaerts *et al.* (1999) describe a spectral index to be a single number derived from some multivariate function using two or more spectral observations. The result of a spectral index is a single channel of data, where each pixel contains a value that describes the characteristic for which the index was designed (Jensen, 1996). One of the overall objectives in the design of vegetation indices is the monitoring of vegetation through the measurement of spatial and temporal variations of vegetation composition and photosynthetic activity (Dawson, 1998). More specifically, the objective is the development of indirect measurements of biophysical parameters such as leaf area index (LAI), fraction of absorbed photosynthetically active radiation (faPAR or FPAR), biomass, and percent green cover (Sellers, 1985; Goward and Huemmrich, 1992; Treitz and Howarth, 1999), as well as geophysical measures of soil condition, surface wetness, and plant stress.

In general, green vegetation exhibits several spectral response characteristics in the visible and near infrared (NIR) portions of the EM spectrum that are different from other materials on the earth's surface. This includes 80–90% absorption by chlorophyll in the visible range (Jensen, 1996), with a slight peak of reflectance in the green range, known as the "green peak". The "absorption well" in the red region of the EM spectrum is followed by a dramatic increase in reflectance in the NIR of 40-50% (Jensen, 1996). The transition area of the reflectance curve between absorption in the red region and reflectance in the NIR is known as the "red-edge", which has been shown in several studies to be sensitive to vegetative stress (Mohammed *et al.*, 1997; Sampson *et al.*, 1998).

Other surface materials have spectral response curves that are dramatically different than vegetation in the visible/NIR region. Water absorbs almost all EM radiation in the NIR portion of the spectrum. Materials such as soil and litter generally exhibit a steady increase in reflectance with wavelength in this region (Goward, 1989). These consistent differences in spectral response are the basis for the assumption that indices can be designed to detect and measure the presence and condition of photosynthetically active vegetation surfaces.

2.1.1 Narrow-Band Indices

Corresponding to the development of remote sensing technology, most of the common spectral indices (e.g., Normalized Difference Vegetation Index (NDVI)) were originally designed for broad-band sensors (A summary of the common broad-band indices found in current literature is included in Appendix A1.1 and A1.2). However, standard laboratory spectroradiometer equipment and hyperspectral sensors can measure radiance at a much finer spectral resolution. Where a broad-band sensor can provide one value as an average of the most intense radiance in a certain range, a hyperspectral sensor can provide a contiguous curve for the same area. It has been shown that stressed vegetation will show a change in the red edge of the spectral reflectance curve which can be described as a shift in the inflection point from longer wavelengths (red) towards shorter wavelengths (blue). While spectroradiometers and hyperspectral sensors have the ability to record these shifts, broad-band multispectral sensors are not. In fact, most of the red edge is not even sensed for the more common broad-band sensors, which tend to focus on the red and the NIR, and not the transitional region between them. This has led

to the development of hyperspectral indices of two types. The first is the adaptation of proven broad-band indices to hyperspectral datasets, which involves the selection of appropriate narrow band(s) to use in place of the broad bandwidths discussed above. A current issue undergoing research in this area is whether or not the hyperspectral data can actually achieve higher correlations to biophysical parameters than the more general broad-band sensors. Second, hyperspectral indices have been developed to accentuate subtle spectral features on the continuous curve (Appendix A.1.3).

There has been some success in developing and relating hyperspectral indices to various forest parameters at the leaf and (to a lesser degree) canopy levels. Most of these relationships concern physiological rather than structural parameters, where changes in these measurements have been related in some way to plant stress. These physiological parameters include a variety of plant measures that can be analyzed in a controlled laboratory setting, including fluorescence, chlorophyll a & b, light absorbing pigments, proteins, nitrogen, lignin, carotenoid concentrations, and cellulose (Belanger, *et al.* 1995; Zarco-Tejada and Miller, 1999; Treitz and Howarth, 1999; Sampson, 2000). In order to understand and model such forest ecosystem processes as photosynthetic efficiency, leaf litter decomposition rates, and net primary production, knowledge of these physiological parameters is crucial (Dawson, 1998).

There has been less work done to relate spectral indices to forest structural parameters, which would include anything that describes the physical presence of forest vegetation. Most of these parameters would be very difficult to represent in a laboratory setting and are very much a function of the scale of observation. Some examples of structural parameters of interest include LAI, crown closure, tree height, tree density,

biomass, leaf and canopy density, live stem size, live/dead volumes, and live/dead stem density (Olthof and King, 1998; Treitz and Howarth, 1999; Sampson, 2000). To date, research reported in the literature regarding forest structural parameters involves the use of spatial statistics, textural analysis, and multiple regression/multivariate techniques (Yuan *et al.*, 1991; Hershey *et al.*, 1998; Olthof and King, 1998; Davison *et al.*, 1999; Phinn *et al.*, 1999; Seed *et al.*, 1999; Seed and King, 2000).

Due to the nature of hyperspectral datasets, the techniques used to derive these indices tend to be more involved than broad-band indices and very specific to a particular application. Careful consideration must be made to the biophysical parameter of interest and the best way of relating the parameter to the reflectance data. To reduce the number of bands required and select the most appropriate band combination often requires rigorous statistical procedures, which help identify the highest correlations between the parameter of interest and the wavelength(s), width of the waveband, and/or their combinations (Dawson, 1998; Merton, 1998; Schmuck *et al.*, 1998; Goveartz *et al.*, 1999).

One area of current research focuses on the geometric characteristics of the red edge and the movement of its inflection point. These relationships can be evaluated through the calculation of first- and second-order derivatives. First-order derivative transformations provide a slope curve that will help to emphasize any subtle differences on the red-edge curve, which may point to useful information regarding absorption and reflection features that would otherwise be obscurred (Elvidge and Chen, 1995; Novo *et al.*, 1995; Merton, 1998). The red-edge inflection wavelength (λ_I) can be found by calculating the second derivative, with the inflection point being the value where the

second derivative equals zero. There are a variety of theoretical applications for λ_t, including the monitoring in spectral shifts for a vegetation community over time (Merton, 1998). This has been correlated to changes in chlorophyll, LAI, leaf inclination angle, and various plant stress factors (Merton, 1998; Mohammed *et al.*, 1997; Sampson *et al.*, 1998). However, recalling the discussion above regarding the confounding factors with broad-band indices, it becomes immediately apparent that hyperspectral calculations are even more problematic beyond a laboratory setting.

First- and second-order derivatives have also been used for the development of hyperspectral indices by integrating the area under the derivative curves of discrete narrow-waveband spectra over the red-edge, or in areas that have been highlighted in first-order derivatives to be areas of subtle or rapid change in slope (Elvidge and Chen, 1995; Thenkabail *et al.*, 1999). Elvidge and Chen (1995) subtracted a local-derivative baseline from their integrated indices to remove background effects, which they found to improve the overall performance of the indices. They also reported using a Fourier transform smoothing algorithm (Press *et al.*, 1989) to smooth the reflectance spectra before differentiating.

As was the case with the broad-band spectral indices, there are many hyperspectral indices currently being developed for a variety of applications (Appendix A.1.3 and A.1.4). One of the issues of concern regarding the utility of hyperspectral datasets for vegetation indices is the overwhelming quantity of data that is associated with each image. Determining the optimal wavelength bands (i.e., feature selection) useful for the analysis of certain biophysical parameters has been a crucial technique used to reduce the original dataset to a more manageable size. This is a challenging process

and often requires the use of statistical regression and modelling techniques. Key to the success of these techniques is a good understanding of the biophysical parameters of interest. When examining the reflectance characteristics of a hyperspectral dataset in general, it has been found that high spatial resolution is more significant than high spectral resolution to identify surface types (Price, 1997). However, when analyzing the specific spectral behavior of a certain parameter, very fine spectral resolution may be required in one or more regions of the EM spectrum.

One analysis technique of interest is the use of multiple linear regression analysis to relate biophysical parameters to reflectance. Thenkabail *et al.* (1999) describe the use of a model to perform an analysis of this type, which calculated the best R^2 values for one, two, four, and n-band combinations using reflectance as the independent variable and biophysical parameters as the dependent variable (using the stepwise MAXR procedure in the statistical package SAS). Thenkabail *et al.* (1999) describe the outputs of this technique as a class of vegetation indices labeled the Optimal Multiple Narrow-Waveband Reflectivity indices (OMNBR). These models (indices) can be tested to determine how much of the variability of the biophysical parameter can be explained by the narrow-waveband variables. Significance testing can be used to determine the utility of additional wavebands, which provides a justifiable method of determining appropriate wavelengths and prevents models from "over-fitting" the dataset (Blackburn, 1998; Thenkabail, 1999). The OMNBR techniques can be very helpful in identifying regions on the spectral reflectance curves that are important for certain biophysical parameters. This would be especially useful if some optimal information about the parameter of interest is not located in the red or NIR wavebands.

Similar regression approaches can also be taken to determine the best possible band combinations to calculate narrow-band versions of the common broad-band indices (e.g., NDVI). This has been accomplished by calculating all possible combinations of NDVI and then correlating them with biophysical parameters (Merton, 1998; Thenkabail *et al.*, 1999). This provides a more rigorous procedure than simply selecting the peak bands in the red/NIR regions. As well, it allows for the probability that the bands selected for a narrow-band NDVI for one biophysical parameter (LAI for instance) may not provide the highest correlation possible for another (e.g. biomass). These considerations appear to be significant, as several authors have utilized different wavelengths for the narrow-band NDVI calculations (Merton and Harvey, 1997; Merton, 1998; Thenkabail *et al.*, 1999; Zarco-Tejada *et al.*, 1999).

It should be noted that when correlating a hyperspectral index to a biophysical parameter, it is not necessary for the most appropriate relationship to be linear. There are a variety of possible relationships between the index and the parameter of interest, which will depend on how a model can be fit to the plot trends to give the best R^2 value. However, one should view a lower R^2 value from a higher order relationship with caution when selecting an appropriate model, as the results in regions which have not been adequately sampled are highly suspect. Thenkabail *et al.* (1999) found that linear and exponential relationships were the most satisfactory models for hyperspectral crop indices. This can also be true when relating broad-band indices to biophysical parameters, as found by Friedl *et al.* (1995) when relating NDVI (from Landsat TM) to LAI and FPAR.

Other approaches to developing hyperspectral indices found in the literature revolve around modelling the spectral response curve or the soil line in spectral space (Merton, 1998; Govaertz, 1999). Merton (1998) created a linear model of the red-edge geometry of the spectral reflectance curve, where the degree of concavity between the upper portion of the red-edge curve and the linear model were used as a measure of vegetation stress. However, in this case, the index was designed to be highly interpretable and somewhat generic, where positive values indicate areas of high stress and negative values indicate low stress. Merton (1998) also had some success relating this index to NDVI for several vegetation communities. There was no report of any attempt to relate this stress index to any specific biophysical parameter.

2.1.2 General Comments on Indices

Upon examination of the characteristics of hyperspectral datasets and the techniques required to perform meaningful analysis with these data, it becomes immediately apparent that most of the problems relating to the effectiveness of broad-band indices will also affect the narrow-band indices. While the very specific nature of most narrow-band indices allows for the possibility that confounding factors can be reduced, the complexity of the datasets increases the potential for confusion. In order to successfully exploit the detailed nature of hyperspectral datasets, it is evident that detailed information on the study area at the time of observation is crucial (more so than for most broad-band studies). This would also include observation conditions that could affect the sensor, such as illumination conditions, orbital information, solar conditions, etc. It is then necessary to determine and account for the significance of these factors on

the specific study of interest. The sheer magnitude and relative novelty of this task may explain the variety of approaches noted in the literature for the development of hyperspectral indices, as the remote sensing community is attempting to address a wide range of issues in this area. Govaerts *et al.* (1999) have outlined a general approach for the design of optimal spectral indices, which could be adopted in most cases to ensure that the optimal spectral index is developed. However, the specific methodology for finding an optimal solution is still completely dependent on the question being asked and the data available to address it.

There is a key difference between the development of a hyperspectral index for forest structural parameters and physiological characteristics. As noted above, most indices derived for physiological parameters are developed in laboratory settings at the leaf scale, followed by attempts to "scale-up", usually through the use of canopy reflectance models (e.g., Grossman et al., 1994; Zarco-Tejada et al., 1999; Peddle, 1999). Structural parameters on the other hand cannot really be measured in a laboratory. If the goal is to relate an existing hyperspectral index to a parameter of interest, the procedures would generally be similar in either case. However, when deriving a new index designed specifically to enhance some structural characteristic, it would be very difficult to establish this relationship prior to image analysis. Based on the literature findings, it seems evident that hyperspectral indices for forest structure will require additional spatial considerations and inputs from a variety of processing techniques. Some of these techniques include canopy reflectance modelling, spectral unmixing analysis, spectral inversions, geostatistical analysis, multiple regression techniques, and statistical significance testing. Careful consideration must also be made regarding the scale of

observation and field analysis. While there is obviously great potential in this area, it is clear that success has been somewhat limited to date, and research is really just beginning.

2.2 Spatial Techniques

Remote sensing images of the Earth's surface have distinct spatial properties characteristic of the landscape at the scale of observation. However, for most applications traditional remote sensing research has concentrated mainly on the spectral response characteristics of objects or areas of interest. This information would then be used to assess the health, status, and/or change in the natural environment over time. Although it was recognized to be a potential contributing factor, little consideration was given to the appropriate scale of study for the process of interest and the pattern of this process across the landscape. This was, in part, due to the historical limitations on remote sensing technology, which severely restricted the options for choice in the spatial resolution of remotely sensed images from space. In many cases, the scientist would simply select the best resolution possible in order to obtain all the spectral information available for a study area. In recent years, advances in technology have enabled very high spatial- and spectral-resolution satellites to be developed for the monitoring of natural resources. This has opened the door for analysis of the landscape at many scales, which has led to a present day focus on a variety of scale issues for remote sensing analysis (e.g., Marceau, 1999).

One of the problems encountered by remote sensing scientists when using very high spatial resolution data is the increased volume of data that must be collected to cover

the same area that a coarser resolution sensor would traditionally have covered. This is due to the obvious fact that coarser spatial resolution sensors require fewer picture elements, or pixels, to cover the same area. This is compounded when considering the increased spectral resolution of a suite of hyperspectral satellites to be launched over the next ten years. With the increased number of spectral bands available for analysis, this will further increase the data quantity by over 200 times the current data sources. Without consideration of scale and pattern in datasets of this size, the sheer quantity of the information will become unmanageable.

Another consideration that has become the focus of much recent attention is the aggregation of datasets across multiple scales for the purpose of studying multi-scaled spatial phenomena in the landscape. This has led to what is commonly referred to as the Modifiable Areal Unit Problem (MAUP), described first by Openshaw and Taylor (1979). The MAUP consists of two seperate but interrelated components; i.e., scaling and zoning (Openshaw and Taylor, 1979, 1981; Openshaw, 1984; Jelinski and Wu, 1996; Marceau, 1999). The scaling problem exists because of varying results that occur when datasets are aggregated into fewer and fewer units for analysis. Zoning can be described as the variation of results that exist due to the many possible methods of aggregating data at the same scales, while still maintaining the same overall number of units (Openshaw and Taylor, 1979, 1981; Openshaw, 1984; Jelinski and Wu, 1996; Marceau, 1999). The implications of the MAUP on spatial data and its influence on spatial statistics of estimation and significance testing has been further presented by Arbia (1989). To date, one of the most promising hopes for managing the MAUP at an acceptable level has been

through the integration of spatial autocorrelation statistics with the analysis (Marceau, 1999).

2.2.1 Spatial Statistics

The main premise behind spatial statistics is the simple concept that points closer together tend to be more similar than points farther apart. This is what is commonly referred to as "The First Law of Geography", and is the basis behind the analysis of surface structure. The very concept of spatial structure implies that the fundamental assumption behind classical inferential statistics, that observations are independent of each other, cannot be applied. This means that statistical analysis of spatial data must include consideration of the dependence of observations on each other and on location.

In current statistical methods, there are two ways to consider structure in spatial data, either through trend surfaces or spatial autocorrelation statistics (Jongman *et al.*, 1995). Trend surfaces imply a gradual change with the landscape, where there is a direct relationship between points. However, in reality, random variations and spatial clustering are often present in the landscape, which confounds the assumptions behind trend surface analysis. In contrast, spatial autocorrelation statistics suggest that short-range variation is often correlated but random. In other words, points closer together tend to be more similar than points farther apart, but there is no direct relationship between them (Jongman *et al.*, 1995).

A variable is autocorrelated (or regionalized) if it is possible to predict its value at a given point in space by knowing its value at other locations (Legendre and Fortin, 1989). Typically, autocorrelation is described as being either positive or negative, where

positive autocorrelation refers to the case when close or adjacent points have very similar values and negative autocorrelation refers to the case of close or adjacent points having unlike values (Legendre and Fortin, 1989). Another measure of the spatial variation of a dataset is the semivariance. Semivariance of an increment $Z(x_1) - Z(x_2)$ can be defined as half of the variance of the increment (Jongman *et al.*, 1995). Semivariograms are used to describe spatial structure in the data or to interpolate surfaces based on a theoretical model.

A semivariogram is a graph with semivariance plotted on the ordinate axis and distance classes on the abscissa. The semivariogram is composed of three main descriptive components, namely the range, sill, and nugget. According to Curran (1988), the sill can be described as the ordinate value at which the semivariogram levels off. This corresponds to the variance of the samples. The range is defined as the distance at which the levelling off occurs. This distance describes the extent of the spatial structure, and can be considered the distance after which points are no longer correlated. The nugget variance is simply the semivariance at distance 0.0 (the intercept), where a value of non-zero implies intrinsic variability (sampling error) or variability at a smaller scale than observed (Curran, 1988).

One of the problems with scale in remote sensing and the MAUP is that it is always possible to reduce the resolution of the image pixels. When examining processes in landscape ecology, it is known that very different processes are occurring even at the microscale level. As remote sensing technology becomes capable of sensing at finer and finer resolutions, some of these smaller processes will contribute more significantly to EM response. As well, a variety of physiographic factors will influence the EM response

at many levels. For this reason, the nugget variance is not particularly useful when examining the semivariograms for a remotely sensed image. Rather it is much more common to determine the range and sill values, and evaluate the shape of the semivariogram curve in order to assess the characteristics of the landscape processes which may be causing such EM response. It should be noted that there are many instances in the natural landscape where a sill is never reached in the semivariogram being analyzed. This indicates that remote sensing data often exhibits characteristics of being non-stationary, making autocorrelogram analysis inappropriate in these cases and providing further impetus for a semivariogram approach (Curran, 1988).

The assumption that these graphs are independent of direction is called the assumption of isotropy (Jongman *et al.*, 1995), with semivariograms that assume isotropy being referred to as all-directional or isotropic. However, in many instances direction has a significant effect on the shape of these graphs. For example, when considering a repetitive landscape such as rows of planted trees, one would expect a periodic semivariogram when examining transects across the rows, but the shape along the rows could be unbounded or aspatial. This directional effect is known as anisotropy (Jongman *et al.*, 1995), and it has a significant impact on the interpretation of the semivariogram.

2.2.1.1 Optimal Sampling

One of the objectives of performing spatial autocorrelation statistics on remotely sensed data is to determine the optimal sampling size for the process under study. This is done by examining the spatial extent of the structure in different directions and choosing

the minimum extent as the optimal remote sensing resolution (Curran, 1988). This considers the effect of anistropy when determining the appropriate spatial resolution of the dataset. However, it should be noted that by collecting square pixels, true consideration of anistropy when considering optimal resolution is not possible. The ideal situation would be the capability to adjust the shape and size of the pixel according to the expected autocorrelation in the study area. However, this is an extremely impractical approach when using remotely sensed data, where sampling methods are dependent on the technological capabilities of the satellite (or airborne sensor) and the computers which process the resulting images. By taking the minimum range, all of the necessary structural information present in the data is captured while reducing the noise as much as possible.

Woodcock and Strahler (1987) describe a technique for determining the optimal sampling spacing by analyzing local variance. Here, the idea is that if the pixel size is much smaller than the size of the object on the surface, the local variance (variance between neighboring pixels) will be low. The variance will then increase as pixel size increases until an inflection point is reached and the local variance begins to decrease again. Woodcock and Strahler (1987) interpreted the inflection point to occur where the pixel size is such that it minimizes the local autocorrelation. Hypannen (1996) used the method of local variance to determine the optimal spatial resolution to study a boreal forest environment. In this study, he created ten images with pixel resolutions ranging from 1m to 10m (by spatially averaging the values from a 1 m resolution dataset). He then calculated the variance for windows of nine neighboring pixels and plotted this

against spatial resolution. This gave an indication of optimal sample size based on the aggregation of square pixels.

2.2.1.2 Theoretical Semivariograms

Theoretical semivariograms have also been shown to be very useful for extracting paramaters from the semivariogram (such as range and sill), as well as modelling surfaces through interpolation (kriging). To make use of the theoretical semivariogram, the empirical semivariogram must first be calculated using the estimator described in previous chapters of this paper. Once this has been done, the shape of the semivariogram is examined, and an appropriate theoretical model is chosen to represent the data.

There is much to be learned about using the theoretical semivariograms to model the empirical semivariogram. It can be easily shown that there is no satisfactory method for choosing the best model. Often the shape of the semivariogram is such that more than one of the theoretical models will fit the empirical semivariogram to approximately the same degree of success. For remote sensing data analysis, theoretical semivariograms are typically used to extract a variety of parameters from the image (Fleming, *et al.*, 1999). With imagery, surface interpolation is not often required, because a surface already exists as an inherent characteristic of a raster dataset. Rather, interpolation techniques are used to design appropriate field sampling campaigns (Fleming, *et al.*, 1999). The selection of the theoretical semivariogram is often not based upon the most appropriate model. Rather, various forms of the spherical and exponential models are heavily preferred because they provide an easily interpreted range and sill value (Curran, 1988; Curran and

Atkinson, 1999). In this case, parameters are adjusted to provide the best possible fit with this model.

2.2.1.3 Comments On Spatial Statistics

Applying spatial statistics to remotely sensed images is not a simple task. In addition to the complications previously mentioned, it should also be noted that different structural effects may be apparent for each wavelength band, as well as each direction. This is simply a function of current remote sensing technology and the variation in spectral response across wavelengths. To date, most remote sensing scientists consider spatial autocorrelation for each band separately, rather than trying to incorporate the bands into multivariate techniques. An exception to this trend was reported Sampson *et al.* (2000), who applied semivariogram analysis to features derived from principal component analysis.

It is apparent that remote sensing scientists are only beginning to understand some of the complexities involved with the application of spatial autocovariation techniques to very high spatial and spectral resolution remote sensing datasets. To date, multivariate techniques such as the Mantel correlogram and the partial Mantel tests (described in Legendre and Fortin, 1989) are not even being successfully applied to these types of data. In fact, the remote sensing community as a whole is struggling to fully understand the implications of autocorrelograms and semivariograms when applied to issues such as scaling of the landscape within an image.

With the problems anticipated from the huge influx of data expected with the launch of hyperspectral and high spatial resolution satellites, it is obvious that the use of

spatial autocorrelation techniques will be crucial for the elimination of data captured at inappropriate scales for the study in question. Marceau (1999, p.355) suggests that spatial statistical techniques such as autocorrelation and semivariogram analysis

> "illustrate that it is possible to control and predict the MAUP effects to some extent. But, most of all, they represent further steps toward the derivation of theoretically sound and operationally practical methods to deal with the issue."

2.2.2 Texture for Forest Structure

Texture features in an image relate intensity values of neighbouring pixels for a specified window size, usually repeated over the entire image, providing some description of the intrinsic spatial variability of the image (Raghu *et al.*, 1995; Zhou and Civco, 1998; Treitz *et al.*, 2000). Visually, this is analogous to the appearance of roughness in the image. Given this definition, there are a wide variety of algorithms that have been developed to quantify image texture, including the spatial statistics described in the section above. For the most part, texture tends to be broadly categorized into structural and statistical measures (Tian and Murphy, 1997; Zhou and Civco, 1998). Structural approaches are designed to describe repetitive patterns in terms of their primitive elements and the geometrical relationships between them (Tian and Murphy, 1997). On the other hand, statistical approaches estimate parameters of random texture that describe image roughness with neither repetitive pattern nor orientation (Tian and Murphy, 1997). Other less frequently reported textural measures include fractals, texture spectrum, spectral texture pattern matching, autoregressive models, log-normal random field models, fourier analysis, and wavelet transforms (Wang and He, 1990; Gong *et al.*, 1992; Jensen, 1996; Zhou and Civco; 1998; St.-Onge, 1999; Treitz *et al.*, 2000).

To date, the most common utility for texture analyses in remote sensing applications has been for the improvement of image classification. This has resulted in statistical texture measures being the most extensively and successfully applied, since they meet the stochastic assumption of digital image classifiers (Jensen, 1996; Zhou and Civco, 1998; Treitz *et al.*, 2000). There are many first-order image statistics that can be calculated for each band, including such measures as mean, standard deviation, variance, entropy, skewness, kurtosis, etc. (Jensen, 1996). Although these measures have shown statistically significant relationships with land cover types, second-order statistics have been shown to be a superior method of texture representation, due in most part to the fact that one or more first-order statistics are contained within the second-order measures (Yuan *et al.*, 1991; Treitz *et al.*, 2000). These second-order statistics are based on gray-level co-occurrence matrices (GLCM). As described by Zhou and Civco (1998, p. 575), a GLCM "measures within-window frequency of pairwise occurrence of brightness values of points separated by the vector defined by the inter-pixel distance and orientation." Based on the GLCM, a variety of second-order statistics can be derived, including the angular second moment, contrast, and correlation (Yuan, 1991; Jensen, 1996; Zhou and Civco, 1998). The neighbouring grey-level dependence matrix (NGLDM) is another measure that has been used to calculate the large number emphasis (LNE) and second moment texture (SMT) statistics for synthetic aperture radar (SAR) data (Rotunno *et al.*, 1996; Treitz *et al.*, 2000).

The approaches discussed in the literature for textural assessment of forest structure are quite varied, with no single technique showing a distinct superiority over others. The most prevalent in the remote sensing literature is what can be described as an

empirical/statistical approach that seems to be concentrated from research in geography, environmental, and earth-science departments. This work focuses around using regression techniques to relate field measurements such as basal area, crown closure, tree height, diameter at breast height (DBH), stem density, etc. to image spectral, textural, and structural (many researchers refer to geostatistics as a form of texture analysis) features. Most commonly reported textural techniques from this group are first- and second-order statistics (Yuan *et al.*, 1991; Hay *et al.*, 1996; Olthof and King, 1998; Seed *et al.*, 1999; Davidson *et al.*, 1999) and/or geostatistics (Cohen and Spies, 1990; Bowers *et al.*, 1994; Hay *et al.*, 1996; King, 1997; Hershey *et al.*, 1998; Butson and King, 1999; Lévesque and King, 1999; Phinn *et al.*, 1999; St.-Onge, 1999).

2.3 Integration of Hyperspectral and Spatial Techniques

It is evident that the combination of spatial techniques with hyperspectral indices is a logical extension to the assessment of forest structural parameters. Intuitively, the ideal hyperspectral/spatial analyses should allow for the exploitation of the complete spectral curve and examination of how aspects of interest on the curve vary spatially. Given the current state of computer and image processing technologies, it is now quite feasible to analyze the entire data cube without reducing it to a more "manageable" size.

One way of approaching this is to extend the spectral calculations that are normally done on point locations to cover the entire image. For example, the current method to calculate the red-edge inflection point is to select a specific pixel, extract the spectral signature for that pixel, calculate the first and second derivatives of the spectral curve and determine where within the red edge the inflection point is equal to zero

(Merton, 1998). This is normally done with samples at the same spatial location over time, to see if the location of the REIP is shifting over time. It is also possible to see if the REIP is shifting over space. This can be accomplished by repeating the calculations for the REIP for every pixel in the image, creating first- and second-derivative images, each containing the same amount of channels as the original hyperspectral image. The second-derivative image could then be used to determine the wavelength on the red edge where the inflection point is equal to zero for each pixel in the image, resulting in a REIP image. Texture and geostatistical analysis could then be completed on any or all of the images (the original hyperspectral data, the first- and second-derivative images, or the REIP image) as a way of incorporating both the spectral and spatial characteristics into index development.

By approaching the analysis in this way, it is possible to explore many more relationships than simply the spatial variations of the inflection point. Once the derivative images are created, the spatial patterns of any promising feature of the hyperspectal or derivative curves could then be examined. In this way, from an image processing perspective, the hyperspectral dataset can be fully explored in a spatial context. The predicted limiting factor when attempting to relate hyperspectral data to field-based measurements would be the suitability of the field-based measurements for hyperspectral analysis at the scale under consideration. The techniques discussed in this chapter, along with other approaches currently being examined by various researchers, promise an exciting future for the integration of remote sensing, landscape ecology, and spatial statistics.

3.0 METHODS

This chapter outlines the design and implementation of the field campaign, with the objective to collect ground-based measurements of forest structure at sites that corresponded to the collection of remotely-sensed data. Procedures used to analyze these field data; collect and process the remotely-sensed data; and derive spectral indices are described.

3.1 Field Data Acquisition

From May to July 2000, a field campaign was undertaken with the objective of characterizing the structure of sugar maple stands in eastern and central Ontario (refer to Chapter 1.3 for a description of these sites). Data collection for these sites, coincided with a Compact Airborne Spectrographic Imager (CASI) mission flown in July 2000. The field campaign was extended to the TLW in July 2000 to collect a similar database for silviculture treatment sites. The CASI data for the TLW were collected in July 1998.

3.1.1 Differential Global Positioning System (DGPS) Data

In May of 2000, initial GPS mapping was undertaken to record the plot dimensions and significant features expected to be visible in the CASI imagery. At each site, white panels were laid out as targets in locations visible from the sky. At a minimum, three targets (approximately 9 feet x 9 feet) were used at each site, distributed as evenly as possible around the exterior of the plot. Care was taken to ensure that the targets were located such that they would not be obscured by canopy growth later in the season. The precise locations of these targets were recorded using DGPS, and served as

ground control points by which the CASI hyperspectral data could be corrected and georeferenced. These data were collected using a Trimble Geoexplorer II system and differentially corrected to the Universal Tranverse Mercator (UTM) projection.

For many applications, the errors now associated with uncorrected GPS are small enough for the coordinates to be used without differential correction. However, errors associated with the ionosphere, the troposphere, ephemeris data, satellite clock drift, measurement noise, and multipath can still cause inaccuracies in the order of +/- 10 to 20 metres (Trimble Navigation Limited, 1996). Any errors that are common to both the base (i.e., reference) and roving GPS receivers can be eliminated using differential correction (i.e., DGPS). For recreational and mapping grade receivers, including the Trimble Geoexplorer used for the field campaign, this typically reduces planimetric error (i.e., x,y) to 1 to 5 m (Trimble Navigation Limited, 1996). The differentially corrected locations for the ISD and FH plots were used for planning and implementing the CASI mission, and subsequently for linking ground-based data to the CASI hyperspectral data.

3.1.2 Mensuration Data

Some experimentation was required to design the most effective sampling scheme to capture the characteristics of the trees that contributed to the forest canopy. For the ISD plots, this initially consisted of sampling all trees with diameter at breast height (DBH) > 10 cm that fell within a 17.6 m (≈0.1 ha) radius of the centre of each quadrant (described in Chapter 1.3.1.1). For each site, this would have covered approximately 0.4 ha, or about 40% of the total plot area (Figure 3).

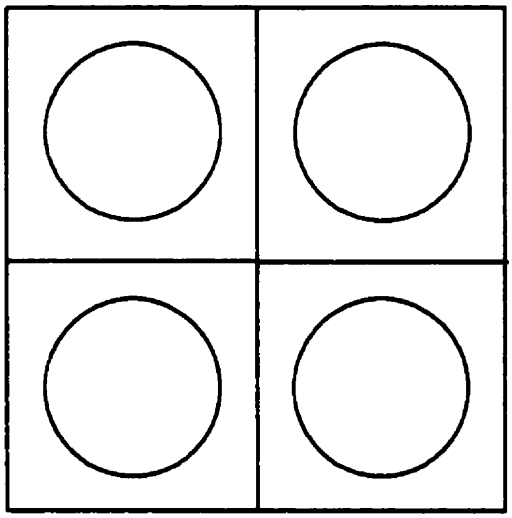

Figure 3: Initial Sampling Design

Field experience quickly illustrated that this design was prohibitively time consuming. However, ground exploration of the sites indicated that for some locations there was considerable variation between the quadrants, which would require sampling in all quadrants. It was determined that a more appropriate approach was to reduce the radius of the sampling areas, while increasing their distribution across the plots. By reducing the sampling radius to 11.3 m (≈0.04 ha, a radius also used for field measurements by foresters at the CFS (Baldwin, 2000)), and centreing 5 locations on the quadrant centres and plot centre, a 20% coverage was achieved while at the same time capturing more of the existing variation within the plot. The following figure illustrates the layout of the final sampling design. Note that due to time constraints, the centre plot was not sampled for three of the ISD plots (ISD 19, ISD 31, and ISD 40). The site averages for these three sites were derived from the quadrant sampling areas.

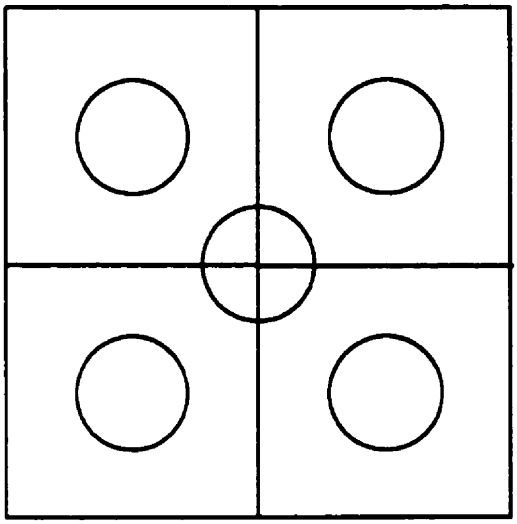

Figure 4: Sampling Design For Ice Storm Damage Sites

Within each sampling area, every tree with a DBH > 10 cm was assessed for DBH, height to the top of the crown, height to the crown base, width of maximum crown axis, width of crown perpendicular to the major width axis, and species. Measuring tapes, designed specifically for measuring stem diameter, were used to measure the diameter of the tree at approximately 1.6 m above ground (i.e., breast height). Tree heights were measured with laser vertex equipment (Haglof Vertex Hypsometer models 1 and 3), which consisted of a transponder and a receiver. To operate this equipment, the transponder was held or attached to the tree at eye level. The vertex was taken away from the tree, level to the transponder at least as far as the tree was tall. A cross-hair sighting was then used to align the receiver with the transponder to get a measurement of the distance from the tree. The vertex was then aimed at the apex of the tree crown to obtain a measurement angle, followed by a similar reading to the base of the crown. The vertex would compute height using triangle geometry.

There were several factors to be considered when using the vertex. Care was taken to ensure the vertex was properly calibrated to the height of the person sampling. Distance to the base of the tree was shown to have an impact on height calculations, with longer distances providing more consistent results. This was easily explained when considering the geometry of the calculations, where a slight variation in angle would have a larger impact when the distance to the base was shorter. For this reason, the estimated height of the tree was used as an approximate minimum guide for the base distance. It was also necessary to come up with a consistent method for determining the base of the crown. It became apparent during the field exercise that the base of a sugar maple canopy was not always distinct, with minor branches occurring all the way down the trunk to almost ground level. It was determined, in consultation with personnel of the CFS, that the most appropriate method was to select the bottom major limb as the crown base, ignoring the smaller branches that grew down the tree (Baldwin, 2000). Canopy widths were measured either using the laser vertex, with the transponder and receiver held under opposite edges of the canopy, or with a tape measure.

As mentioned, previous field work by various groups in the TLW had resulted in a considerable amount of mensuration data stored in various formats by several forest scientists. Although these data were extensive, it was not consistent across all of the sites, and did not contain all of the same measurements taken at the ISD and FH plots. Therefore, the field work at this location was mainly completed to collect data missing from the database. This included tree heights of all trees with DBH > 10 cm within an 11.3 m radius from the plot centre, as well as the two measures of canopy width. Hemispherical photos were also taken at the centre of each plot. Scientists at OFRI and

CFS provided the remainder of the data in either digital or hardcopy format. Refer to Chapter 1.3.2 for a description of the size and layout of these plots.

3.1.3 Canopy Hemispherical Photography

To determine canopy closure, hemispherical photos were taken at each quadrant and plot centre. This was done using a camera and fish-eye lens, at a height of one metre above the ground, leveled, and oriented towards north. Care was taken to ensure that there was a minimum of one metre overhead clearance from hanging branches. Photographs were taken using sky, red, and blue filters for each location, preferably in overcast conditions. In cases where the sky was clear, the camera was configured to have the sun behind the trunk of a tree, minimizing the effects of sun glare.

To catalog any general observations, ground-, eye-, and canopy-level photographs were taken at each site. Any unusual field characteristics were noted in the logs, and any unusual or unidentified features were photographed.

3.2 Field Data Processing

With the exception of the hemispherical photos, all of the mensuration data collected in the 2000 field campaign were in hardcopy format. To facilitate use of these data for analysis, all data were entered into digital spreadsheet templates and/or GIS data layers. This allowed for the calculation of forest metrics for analysis with the CASI data. Due to external interests in the TLW, this database, which was far more extensive, was developed separately in MS Access and integrated into ArcView GIS. Once all of the data were in a digital format, average forest metrics were calculated.

3.2.1 Mensuration Data

Several forest metrics were calculated from the field measurements. Due to the differences in plot size and layout between the ISD, FH, and TLW plots, there were some variations in the calculation methods for each location. For the ISD plots, average parameters were calculated for the entire plot, as well as for each quadrant (i.e. A, B, C, D as discussed in Chapter 1.3.1.1). Table 1 outlines the forest metrics used in this study, with the exception of those determined from the hemispherical photos.

Table 1: Forest Metric Equations (Adapted From Hansen *et al.*, 2001)

Metric	Equation
Number of Trees With DBH > 10 cm	Manual count
Average DBH - arithmetic mean (cm)	$DBH_{arithmetic} = \frac{\sum_{i=1}^{n} dbh_i}{n}$ (1)
Average DBH - quadratic mean (cm) *Shown to have a stronger correlation to stand volume than DBH_{mean} (Brack, 1997)*	$DBH_{quadratic} = \sqrt{\frac{\sum_{i=1}^{n} dbh_i^2}{n}}$ (2)
Stand Basal Area (m^2/ha)	$\frac{\pi}{40000} * \frac{\sum dbh^2}{plot\_area(ha)}$ (3)
Average Tree Height (m)	$Avg\_T_{height} = \frac{\sum_{i=1}^{n} T_{height(i)}}{n}$ (4)
Average Height to Base of Crown (m)	$\frac{\sum_{i=1}^{n} Crown_{base\_height(i)}}{n}$ (5)
Average Crown Depth (m)	$\frac{\sum_{i=1}^{n} (T_{height(i)} - Crown_{base\_height(i)})}{n}$ (6)
Average Stem Density (#/ha)	$\frac{Num\_trees_{(DBH>10cm)}}{sampling\_area(ha)}$ (7)

Average Major Canopy Width (m)	$\frac{\sum_{i=1}^{n} Can_{width(major)}}{n}$	(8)
Average Perpendicular Canopy Width (m)	$\frac{\sum_{i=1}^{n} Can_{width(perpendicular)}}{n}$	(9)
Average Canopy Diameter (m)	$\frac{\sum_{i=1}^{n} (Can_{width(major)} + Can_{width(perpendicular)})/2}{n}$	(10)
Crown Closure – circular (%)	$\frac{\pi \sum_{i=1}^{n} (Canopy\_Diameter)^2}{4*(sampling\_area)} * 100$	(11)
Crown Closure – ellipse (%)	$\frac{\pi \sum_{i=1}^{n} (Can_{width(major)} * Can_{width(perpendicular)})}{4*(sampling\_area)}$	(12)

3.2.2 Canopy Hemispherical Photography

Leaf area index (LAI) is an index often used to characterize the geometric structure of a plant community, and can be described as the ratio of the leaf surface area of a plant to the amount of ground surface beneath it. It is related to forest canopy light penetration, snow accumulation and melt, interception, evapotranspiration, productivity, and the carbon budget (Waring and Running, 1998). Quantifying LAI for a forest canopy site is very difficult, and it is often approximated with "effective LAI", which is calculated from some measurement of canopy gap fraction (derived in this case from hemispherical photos). Digital image analysis to compute effective LAI and percent canopy openness was completed using the Gap Light Analyzer Software v 2.0 (Frazer *et al.*, 1999). The analysis consisted of three main steps: 1) image registration, where the orientation (described above) and circular extent of the hemispherical photo were identified; 2) image classification, where thresholding was used to create a binary image

of visible and obscured sky (canopy openings and foliage); and 3) calculation of LAI and percent canopy openness based on the classified image.

Hemispherical photographs were collected so that north was at the top of the image (Figure 5). This facilitated geographic registration in a consistent manner for each photo. The circular extent of the hemispherical photo was directly identified by manual interpretation of the image.

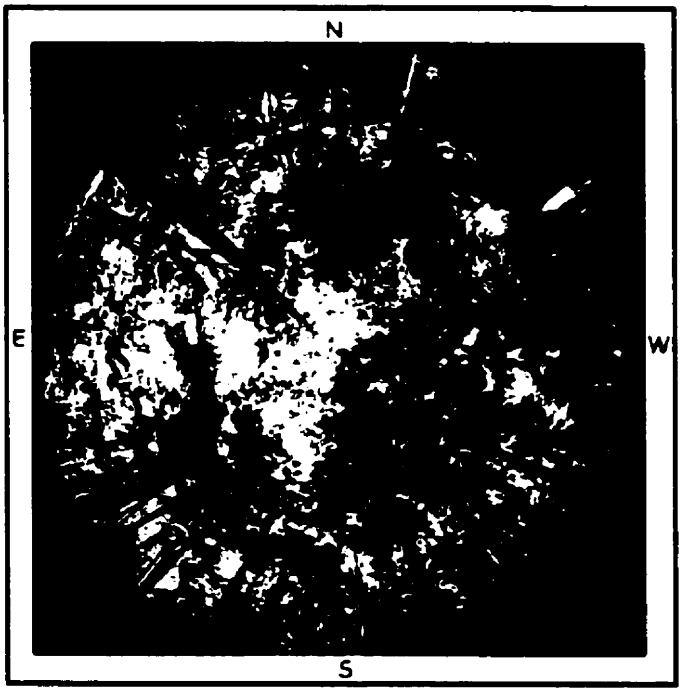

Figure 5: Orientation Of The Hemispherical Photograph

Image classification of canopy openness and foliage required some experimentation to select an appropriate threshold value. This required interpretation and judgement in each case, as results varied considerably depending on acquisition conditions. In particular, cloud cover, which ranged from completely overcast to completely cloud free, and sun angle, which ranged from low (early morning/late

afternoon) to high (mid-day), caused two types of confusion in certain areas of the image. The first and most common source of confusion occurred when leaf edges were sunlit from the side or were directly in line with the sun and were mistaken for sky, resulting in considerable underestimation of the vegetation component (Figure 6). The second source of error occurred when dark blue sky was mistaken for vegetation, which resulted in considerable overestimation of the vegetation component.

Figure 6: Leaf Edge Effects For a True Color and Threshold Image

Having three images for each site (true color, red filtered, and blue filtered) assisted considerably in the reduction of these errors. In most cases, the blue component of the blue-filtered image appeared to be the most effective for classification purposes, significantly reducing the sky and leaf-edge effects. This can be noted in the improvements with the blue component of the same image that was previously shown, along with its threshold image (Figure 7).

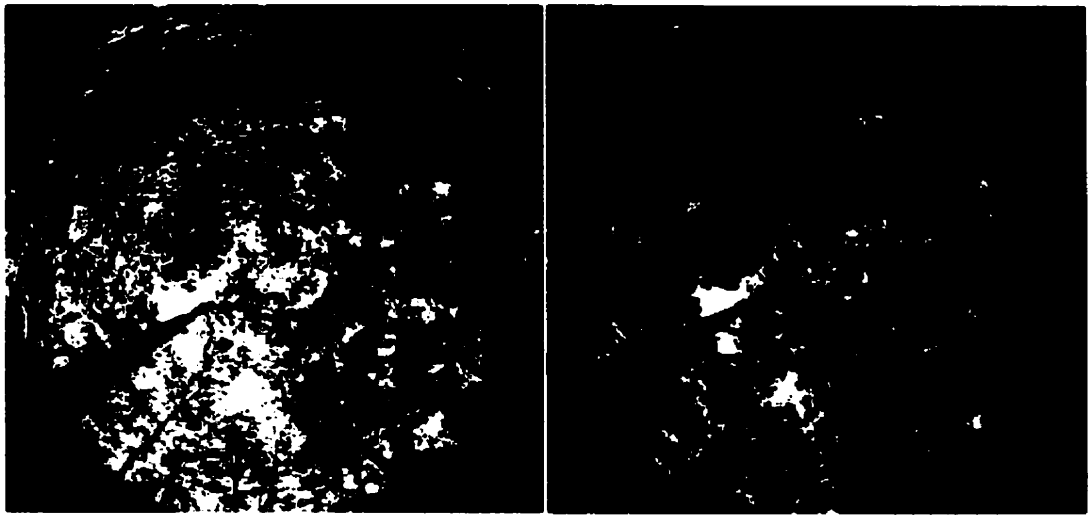

Figure 7: Blue Component and Threshold Hemispherical Image

Due to variations in acquisition conditions, it was found that there was no simple way of accounting for the confusion in an automated manner. The most effective method for producing a binary image was the manual adjustment of the thresholds, chosen by comparing the original image to the classified image and modifying the thresholds where necessary (Prenzel, 2000). Once binary images were generated, percent canopy openness was determined by calculating the proportion of the area of the hemisphere that was foliage (black) or open sky (white). This information was input to effective leaf area index algorithms to determine LAI, which were calculated based on the integration of zenith angles of 0 to 60 degrees (LAI 4^{th} ring) or 0 to 75 degrees (LAI 5^{th} ring) (Frazer *et al.*, 1999).

3.3 Compact Airborne Spectrographic Imager (CASI) Data

The Compact Airborne Spectrographic Imager (CASI) was used to collect the hyperspectral data for this research. CASI is a visible/near-infrared pushbroom imaging spectrograph with a reflection grating and a two-dimensional CCD solid-state array

measuring 512 x 288 pixels (Gray *et al.*, 1997). CASI is capable of three sensor modes, which vary in terms of spatial and spectral resolution. These include: mapping mode; hyperspectral mode (72 spectral channels); and full-spectral mode (288 spectral channels).

3.3.1 CASI Data Acquisition

CASI data were acquired from a Piper Navajo Chieftan aircraft in July, 1998 for TLW and in July, 2000 for the ISD and FH sites. Mapping and hyperspectral mode data were collected for all sites by the Centre of Research for Earth and Space Technology (CRESTech) as part of the Bioindicators of Forest Sustainability Project. Mapping mode data were collected at approximately 0.5 m spatial resolution (spatial resolution varies according to altitude and velocity of the aircraft), with 7 spectral bands (Zarco-Tejada, 2000). These data were used to locate the field sites and plan the hyperspectral mission. The hyperspectral mode data were collected at approximately 1.5 m spatial resolution for the ISD and FH sites, and at approximately 2 m spatial resolution for TLW (Zarco-Tejada, 2000). All hyperspectral data consisted of 72 spectral bands with approximately 7.5 nm spectral resolution (Appendix A.6). While the hyperspectral mode mission was being flown, ground-based aerosol optical depth data were collected by scientists from York University using a Micro-Tops III sunphotometer at multiple wavelengths (i.e., 40; 380; 440; 500; 670; 870; and 1020 nm) (Zarco-Tejada, 2000).

3.3.2 CASI Data Preprocessing

CASI data were collected at 12-bit radiometric resolution and pre-processed by CRESTech to at-sensor radiance using calibration coefficients developed at CRESTech

(Zarco-Tejada, 2000). The aerosol optical depth data collected in the field were used to derive aerosol optical depth at 550 nm. This information was used with the CAM5S atmospheric correction model to process the hyperspectral radiance data to ground reflectance (Zarco-Tejada, 2000). Finally, these data were geo-referenced using DGPS data collected on the aircraft. This process involved the resampling of the hyperspectral data to 1.5 m square pixels for all of the ISD and FH sites, and 2 m square pixels for TLW (Zarco-Tejada, 2000).

3.3.3 CASI Data Processing

The objectives of the hyperspectral image processing phase of this research were to quantify the relationships between the field measurements of forest structure to the CASI hyperspectral data. These relationships were then used to develop structural indices for the sugar maple environment. Hyperspectral and spatial techniques were explored concurrently, and then combined to take advantage of the high spatial and spectral resolution of the CASI data cube. Currently, the spectral curve and its derivatives are normally considered at a single point irrespective of spatial pattern. However, by creating calculus images, it is possible to explore the spectral curve and its derivatives to discover spatial patterns.

3.3.3.1 Calculus Images

The following calculus secondary images were generated from the original hyperspectral data: 1) first-derivative image; 2) second-derivative image; 3) red-edge inflection point image; and 4) integral image (integrated over the entire spectrum).

To generate the derivative and integral images, it was necessary to incorporate computer programming techniques to iterate through the entire hyperspectral data cube. For each spatial location, the entire spectral curve was extracted. Numerical differentiation was performed using three-point, Lagrangian interpolation to create a new derivative curve. This curve was then written to a new image, and a new derivative data cube was generated in a pixel-by-pixel fashion. The second-derivative image was generated using the same method, applied to the first-derivative cube. To generate an "integral image", a similar "pixel-by-pixel" approach was taken to extract the spectral curves. In this case, a five-point Newton-Cotes integration formula was used to approximate the single-value integral solution to the spectral curve.

As discussed in Chapter 2, the REIP is often an area of interest for vegetative analysis. To examine the spatial variations of this value, a single image channel was created, with each pixel containing the wavelength where the inflection point value of the spectral curve was equal to zero. This was determined by examining the second-derivative cube in the wavelength region where the red edge would occur, somewhere between red and NIR regions of the EM spectrum (600-800 nm). Again, a computer program was generated to examine the second derivative curve for each pixel within the 600-800 nm wavelength region. To determine the exact location of the REIP, the two consecutive image channels where the shorter wavelength had a second derivative less than zero and the longer wavelength had a second derivative greater than zero were isolated. A linear interpolation was then calculated between these wavelengths to extract the exact position where the inflection point was equal to zero. This was done for the entire image to create a new "REIP" image. Note that this calculation is only valid for

cases where the pixel actually contains vegetation. For other land-cover types, a value for the REIP, while mathematically possible, would be meaningless. To ensure that non-vegetated pixels did not confound the analysis, a value of zero was assigned to any pixel where the sign of the second-derivative did not change from positive to negative over the 600-800 nm region.

3.3.3.2 Narrow-Band Indices

There has been considerable hyperspectral work completed at the leaf scale to relate spectral reflectance to biochemical parameters such as chlorophyll a, chlorophyll fluorescence, efficiency of radiation use, pigment, % nitrogen, % lignin, vegetative stress, and photosynthetic capacity. This has resulted in a collection of narrow-band indices reported in the literature (Appendix A.1.3 and A.1.4). To date, these indices have not been correlated to forest structure parameters. To test them, the ratio-based narrow-band indices presented in Appendix A.1.3 were calculated using the most closely matching CASI channels. This resulted in 31 new channels, with each channel containing the results of one of the narrow-band indices (Table 2).

Table 2: Creation of Existing Narrow-Band Index Image

Index (Appendix A.1)	**Modified Formula (wavelength, nm)**
PRI1	(528-565)/(528+565)
PRI2	(528-573)/(528+573)
PRI3	(550-528)/(550+528)
PRI4	(573-543)/(573+543)
NDVI1	(831-671)/(831+671)
NDVI2	(778-671)/(778+671)
VOG1	740/724
VOG2	(732-747)/(717+724)
VOG3	(732-747)/(732+724)
G_M1	747/550
G_M2	747/701

LIC1	(801-679)/(801+679)
LIC2	438/694
LIC3	438/740
SRPI	431/679
NPQI	(416-438)/(416+438)
NPCI	(679-431)/(679+431)
GI	558/679
SIPI	(801-453)/(801+648)
SR	778/679
CTR1	694/424
CTR2	694/762
RVSI	[(717+755)/2]-732
VOG4	717/709 (1^{st} deriv)
LIC4	integrate 453-679
ADR	integrate 679-762
LPR	max(679-747)
LP1G	max(498-603)
LP2G	min(498-603)
RO	min(648-701)
RS	max(701-770)

3.3.3.3 Geostatistical and Texture Analysis

Geostatistical results will vary based on wavelength and spatial resolution (Sampson, 2000; Treitz, 2001). Since a single, optimal filter size does not exist across the entire data cube, geostatistical analysis was performed prior to specifying an appropriate filter size for texture calculations. To accomplish this, transects in the north-south and east-west directions were extracted for each channel at every site. For every transect, empirical semivariograms were calculated (Jongman *et al.*, 1995):

$$\hat{\gamma}(\mathbf{h}) = \frac{\sum_{i=1}^{n-\mathbf{h}} [Z(x_i + \mathbf{h}) - Z(x_i)]^2}{2(n - \mathbf{h})} \qquad (13)$$

Where: h = lag distance
Z = value at location x
N = number of data pairs separated by distance, h

Once the semivariograms were calculated, the range values were estimated by modelling the empirical semivariogram and extracting the range parameter from the theoretical model. The spherical, exponential, linear, linear to sill, and gaussian models were applied to each empirical semivariogram to estimate the range. An examination of the results indicated that the spherical model most frequently provided the best fit to the empirical semivariogram, giving the lowest residual sum of squares value and the highest regression coefficient. To be consistent, the spherical model was used to extract range values in all cases:

For $\mathbf{h} \leq A_0$:

$$\gamma_{(\mathbf{h})} = Co + C[1.5(\mathbf{h}/A_0) - 0.5(\mathbf{h}/A_0)^3 \qquad (14)$$

For $\mathbf{h} > A_0$:

$$\gamma_{(\mathbf{h})} = Co + C \qquad (15)$$

where: $\mathbf{h}$ = the lag distance interval
Co = nugget variance ≥ 0,
C = structural variance $\geq$ Co, and
A_0 = range.

For each of the selected channels, minimum range values from this analysis were used to select an appropriate filter size and shape for the generation of texture images. The following first-order texture statistics were generated: 1) range; 2) mean; 3) variance; 4) entropy; and 5) skewness. Range, mean, and variance are common first-order statistics that will not be explained further here. Entropy is a concept that is described in more than one way in the literature. To fit the context of first-order texture in digital image processing, entropy can be described as a measure of randomness or disorder in the texture filter. It is low when the image is uniform within the filter (PCI, 1998). The mathematical definition used to calculate entropy is shown below (Jensen, 1996).

$$ENT = \sum_{i=0}^{quant_k} \frac{f_i}{W} \ln \frac{f_i}{W} \qquad (16)$$

Where: f_i = frequency of value occurring in the filter window
$quant_k$ = quantization level of the image (in this case 2^{16} = 0 to 65535)
W = number of pixels in the image

First-order skewness can be described as the lack of symmetry in the filter. It is reported as the coefficient of skewness (C_s), and is calculated as follows (Rozgonyi, 1995):

$$C_s = \frac{(mean - median)}{standard\_deviation} \qquad (17)$$

Second-order statistics based on the grey-level co-occurrence matrix (GLCM), included: 1) mean; 2) variance; 3) homogeneity; 4) contrast; 5) dissimilarity; 6) entropy; 7) angular second moment; and 8) correlation. Mean, variance, and entropy are similar to the first-order statistics, except that they are calculated for the GLCM, which describes the frequency of occurrence of values relative to a specified distance and direction. For this work, the shift was one pixel in both the X and Y positive directions, which is the default (and the most common) shift reported for texture work (ENVI, 2000).

Homogeneity is a measure of local uniformity, with the reported value being high when the GLCM is uniform. It is defined by the following equation (Hall-Beyer, 2000):

$$\sum_{i,j=0}^{N-1} \frac{P_{i,j}}{1+(i-j)^2} \qquad (18)$$

Where: $P_{i,j}$ = the normalized GLCM
i,j = row, column location
n = number of pixels in the matrix

Contrast and dissimilarity are both measures of local variance (essentially the opposite of homogeneity), with high values indicating greater variance. Contrast can be calculated with the following algorithm (Hall-Beyer, 2000):

$$\sum_{i,j=0}^{N-1} P_{i,j}(i-j)^2 \qquad (19)$$

Dissimilarity is very similar to contrast, except that it uses linear weighting in the matrix:

$$\sum_{i,j=0}^{N-1} P_{i,j}\,|i-j| \qquad (20)$$

Note that because this is a linear measure, this statistic is considered to be a first-order calculation (Hall-Beyer, 2000). However, it is included with the second-order texture features because it was calculated using the GLCM.

The angular second moment is described as another measure of local homogeneity and can be considered the opposite of entropy. It incorporates the normalized GLCM as a weight in itself, and is calculated with the following equation (Hall-Beyer, 2000):

$$\sum_{i,j=0}^{N-1} P_{i,j}^{\,2} \qquad (21)$$

Finally, co-occurrence correlation measures the linear dependency of values of neighbouring pixels, and helps to assess spatial autocorrelation in an image. If the range of spatial autocorrelation is larger than the filter, this texture value tends to be high (Hall-Beyer, 2000). It is calculated as follows (PCI, 1998):

$$\sum P_{i,j}\left[\frac{(i-\mu_i)(i-\mu_j)}{\sqrt{(\sigma_i^2)(\sigma_j^2)}}\right] \qquad (22)$$

Where: μ, σ^2 = mean, variance

Once the texture images were generated, the correlation analysis was performed for these indices, in an identical manner to that described in Chapter 3.3.3.

3.4 Correlation Analysis

Correlation analysis enabled the linkage between the field metrics and the hyperspectral indices. Calibration correlation analyses involved the calculation of the Pearson correlation coefficient between each calibration index and the field metrics. These results were used to develop correlation curves, which illustrate the pattern in correlation between the index and the metric across multiple channels (i.e., reflectance, derivative, and texture). Results from this analysis allowed for the identification of promising indices that were validated using the TLW dataset.

3.4.1 Calibration Data

To examine the relation of reflectance and its derivatives to the ground-based biophysical variables, the mean, standard deviation, and variance values were extracted from the hyperspectral data cube, calculus images, and index images for each channel and correlated with the mensuration data. This was done for each of the quadrant centres as well as the centre of the plot (Note: only the plot centres were used for the FH plots, which were not divided into quadrants). The extraction technique was designed to average image values from an area that closely approximated the ground sampling effort. To extract the values, the centre coordinate obtained in the GPS mission was used as the

centre location for the extracted region. A fourteen by fourteen pixel region (21 m x 21 m; ≈0.04 ha) was then extracted, centreed around this coordinate (Figure 8).

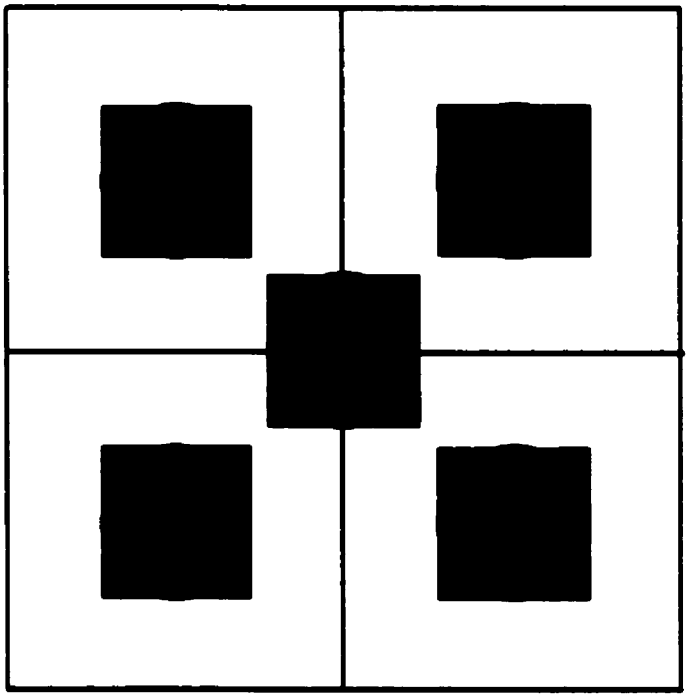

Figure 8: Reflectance Extraction Regions With Sampling Regions Overlain

This approach differed from the technique utilized by Zarco-Tejada and Miller (1999), where only the brightest pixels were selected in an attempt to reduce shadow effects. However, in this case, it was more appropriate to incorporate effects of shadow, as one would expect structural differences to be expressed as variations in reflectance. Values for mean, standard deviation, and variance were then regressed against the extracted region for each channel, to determine which regions were more closely related to each biophysical parameter.

Due to the way the ISD plots were sampled, there were a variety of ways that the image data could be related to the field metrics. Although there were five extraction areas for the ice storm damage sites, it was important at this stage to consider the spatial

dependency of the samples within each of the ice storm damage sites. Given the close physical proximity of the extraction areas and the similar environmental conditions within the entire plot, the five extraction areas could not be considered independent samples. For this reason, the extraction areas were combined to form an average measure for each ice storm damage plot, which would make up one independent sample for the correlation analysis.

3.4.2 Validation Data

The geostatistical and texture analyses of the CASI data and their derivative cubes completed the integration of spatial and hyperspectral techniques. The final stage in the analysis was the validation of the indices, and an analysis to determine whether the integration of spectral/spatial measures provided higher correlations with the field parameters than either the spatial or hyperspectral techniques alone. Validation of the optimal results was completed by testing the indices on the TLW dataset. Up to this stage, the TLW dataset was not used in the analysis and served as an independent validation site. Although the structural variations caused by silviculture treatment would be different than the ice storm damage, the strength and robustness of the relationships identified for the calibration sites (ISD and FH) could be validated.

3.4.3 Predictive Indices

The correlation analysis described above was used to identify strong relationships between the calculated metrics from the study sites and hyperspectral data. These relationships are typically reported as either the correlation coefficient (r) or the

coefficient of determination (r^2), which is a measure of explained variance. They are very useful indications of the utility of remote sensing for the application under consideration, and results are most often reported in this fashion, particularly when the relationships are unknown prior to the study, as in the case of this research. However, if a strong correlation is found, the index can be converted into a predictive measure by determining the parameters of the equation describing the correlation (Hansen *et al.*, 2001).

Considering the index in a predictive manner represents the next phase of research, which would allow discovered and proven relationships to be expressed in a fashion that is directly useful for forest managers, enabling them to predict the value of a forest metric for a certain area simply by applying the predictive index. This enables research into the spatial distribution of a particular parameter of interest mapped directly from the imagery, which could highlight change in the metric over time, or pinpoint areas of concern that would require a more detailed ground evaluation. These maps can then be integrated with other data sources using GIS, enabling very sophisticated environmental analysis. For illustrative purposes, this was done for the strongest relationship discovered in the analysis above that held for the validation data. Using a metric in this fashion allows the forest metric of interest to be quantitatively mapped with known accuracy. It should be noted that predictive measures are beyond the scope of this research, and an example is only provided to illustrate the modelling potential of these techniques.

4.0 RESULTS

4.1 Introduction

Site level field metrics for each study area can be found in Appendix A.2 (calibration sites) and A.3 (validation sites). The original mensuration and GPS data collected for this study have been digitally archived at the Laboratory for Remote Sensing of Earth and Environmental Systems (LARSEES) in the Department of Geography at Queen's University. A list and description of the metrics calculated is presented in Chapter 3.2.1.

All of the spatial data for this study are in the UTM projection, with a WGS84 datum. The study area spans three UTM zones. TLW is located in UTM zone 16, the FH sites are in UTM zone 17, and the ISD plots are in zone 18. Differentially corrected eastings and northings for the centres of each plot can be found in Appendix A.4.

Extensive computer code was developed in the Interactive Data Language (IDL) to process the data for this study at almost every stage of the analysis. Though its length prohibits its inclusion in this thesis, it has been digitally archived onto CD-ROM and can be made available upon request. These software routines were used in the analysis to calculate first- and second-derivative calculus images, texture measures, correlations, etc.

4.2 Spectral And Spatial Indices

Initial processing of the CASI data resulted in multiple spectral and spatial indices, including: the CASI reflectance images; the first- and second-derivative images; red-edge inflection point images; integral images; empirical and modelled semivariograms for each of these images; and various texture derivatives for each of

these images (refer to Chapter 3.3.3). Note that the images derived from narrow-band indices (Table 2) did not result in notable relationships (i.e., strong correlations) with structural metrics and are not discussed further.

4.2.1 Hyperspectral, Calculus, Red-Edge Inflection Point (REIP), and Integral Indices

The large volume of hyperspectral imagery and derivatives prohibits their display here. Sample images from ISD plot 21, along with extracted spectral or derivative curves, are presented in Figures 9-15. For illustration, a NIR reflectance composite, containing two channels in the red edge and one in the NIR is presented in Figure 9. The pale green illustrates the forest canopy in the middle of the image and a vegetated field in the east of the image, both of which reflect strongly in the NIR (green channel). Individual tree crowns and shadows can be identified within the 100 m x 100 m plot (outlined in yellow).

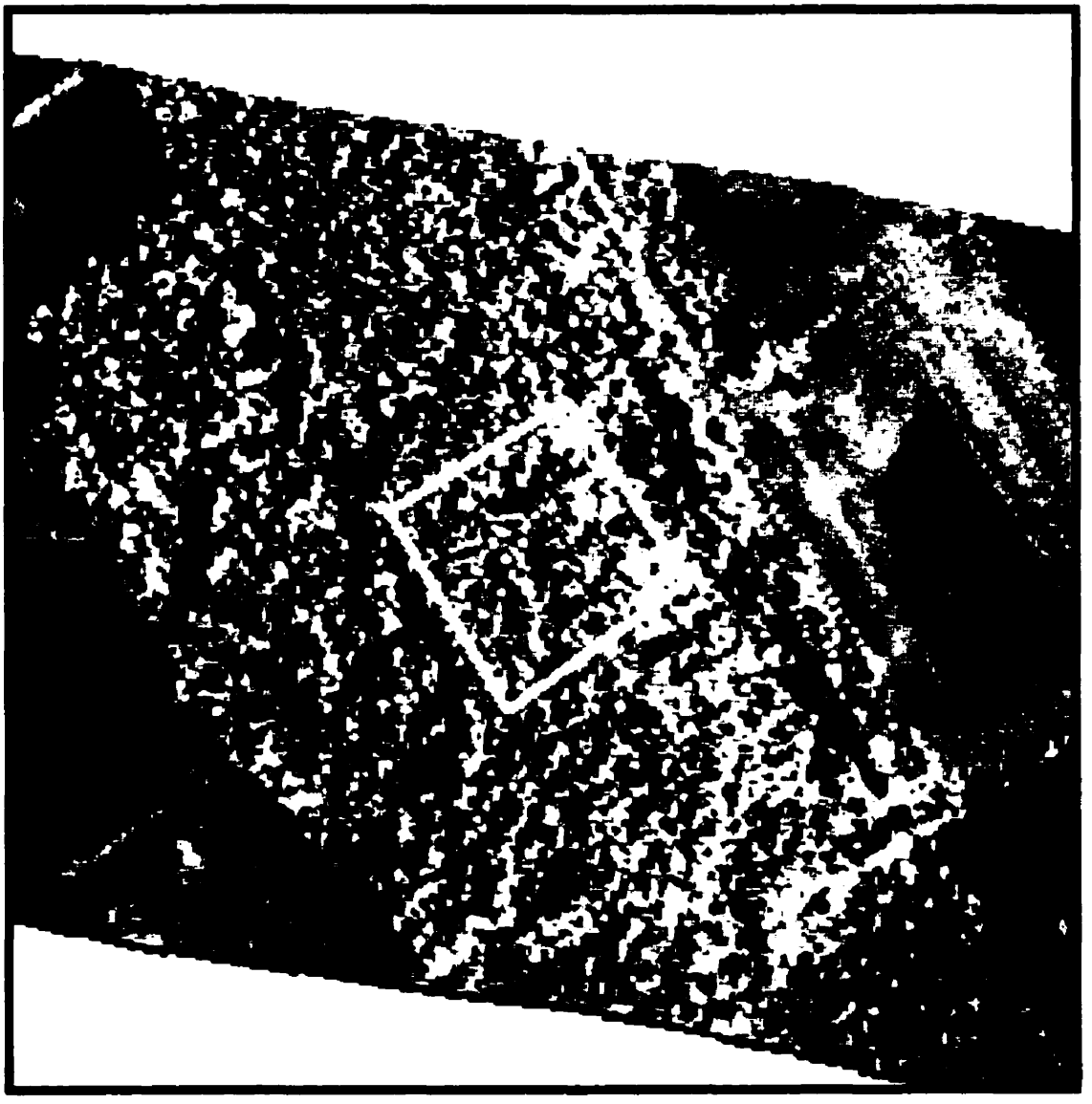

Figure 9: CASI Hyperspectral NIR Reflectance Composite - ISD 21

Red: 739 nm, Green: 816 nm, Blue: 709nm

The spectral reflectance curve for the crown in the centre of ISD 21 is illustrated in Figure 10. It is consistent with typical vegetation response (Lillesand and Kiefer, 1994). Some notable features include the green peak at approximately 558 nm, the beginning of the red edge at approximately 686 nm, the REIP in the vicinity of 724 nm, and the oxygen absorption feature at 762 nm (Adler-Golden *et al.*, 1999), which is also approximately the end of the red edge.

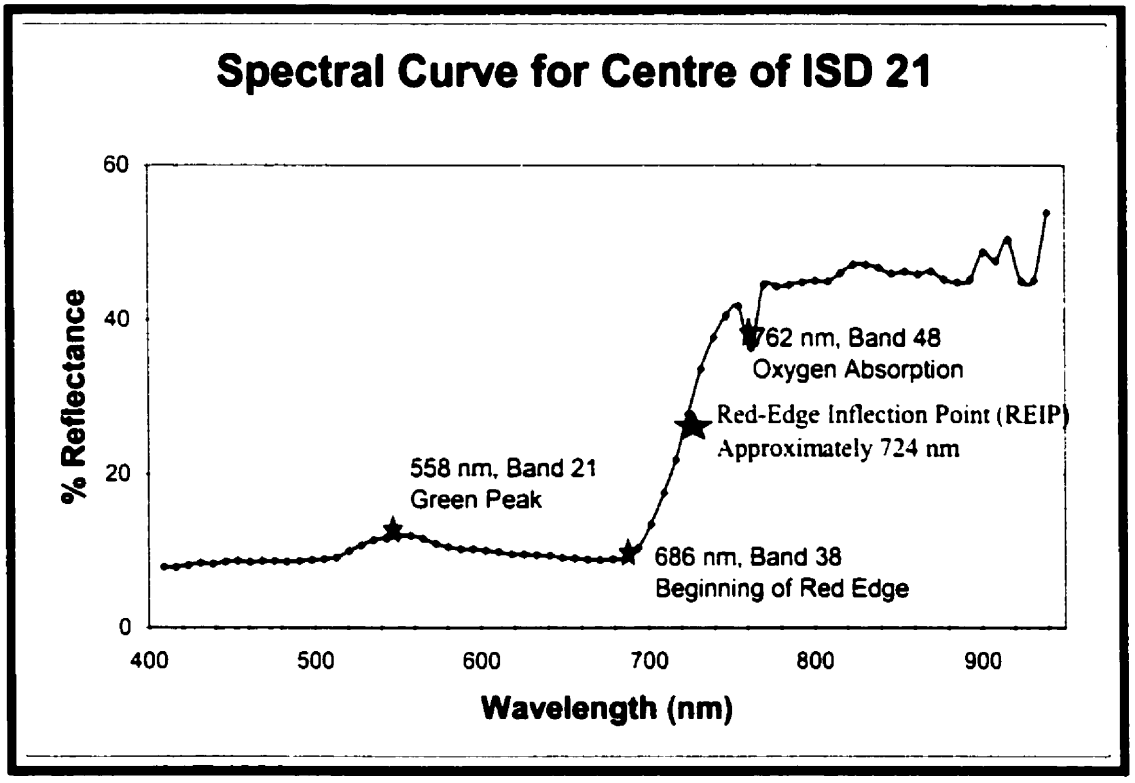

Figure 10: Spectral Reflectance Curve for Centre of ISD 21

Figure 11 presents the first- and second-derivative curves corresponding to the centre pixel (i.e., tree crown) for Figures 14 and 15 respectively. The REIP (≈724 nm) indicates the location where the reflectance curve changes from concave up to concave down (see Figure 10). It can be identified as the maximum value along the first-derivative curve (within the red-edge wavelengths: 600 – 800 nm) or the location where the second derivative is equal to zero. Note that the oxygen absorption feature (at 762 nm) is greatly exaggerated on these curves.

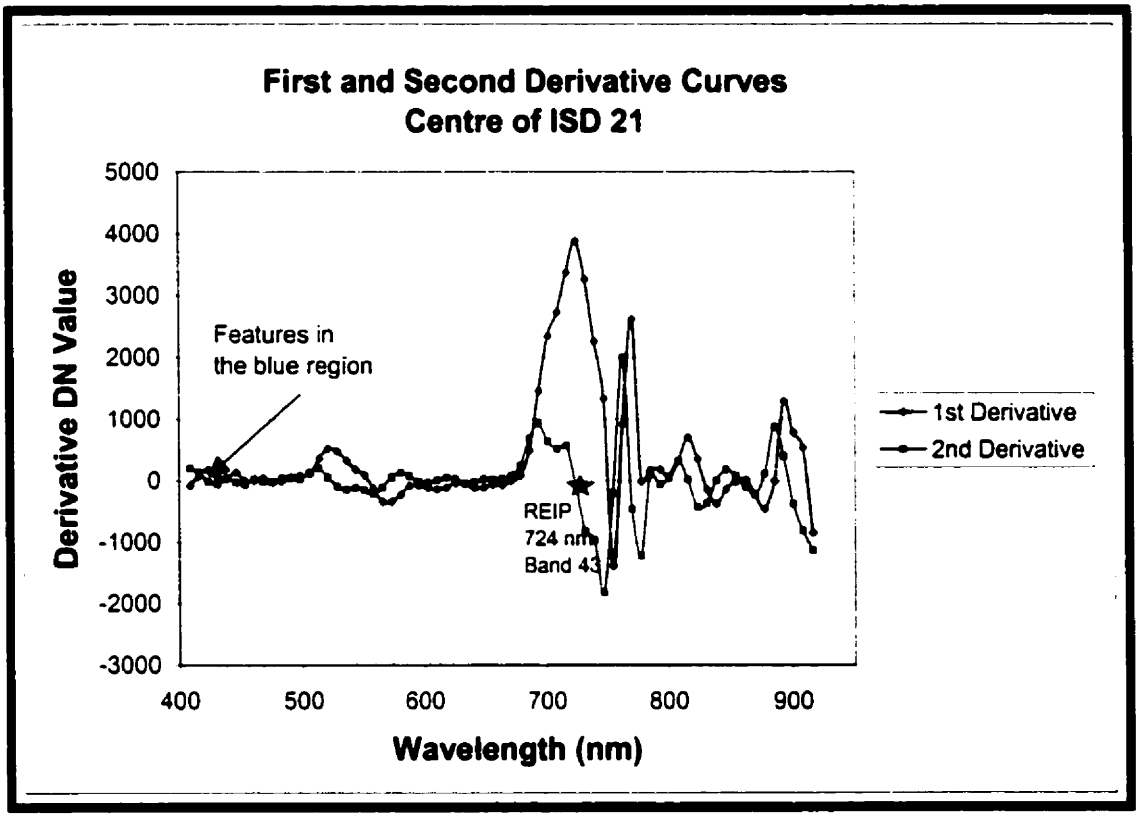

Figure 11: First- and Second-Derivative Curves For Centre of ISD 21

The first-derivative image at 739 nm is shown for the same location in Figure 12. Light areas indicate a larger change in reflectance between the reflectance channel at 739 nm and its adjacent channels (i.e., larger slope on the reflectance curve). Since 739 nm is along the red edge, all vegetated areas (which would have a reflectance curve similar to that shown in Figure 10) should appear brighter in the image.

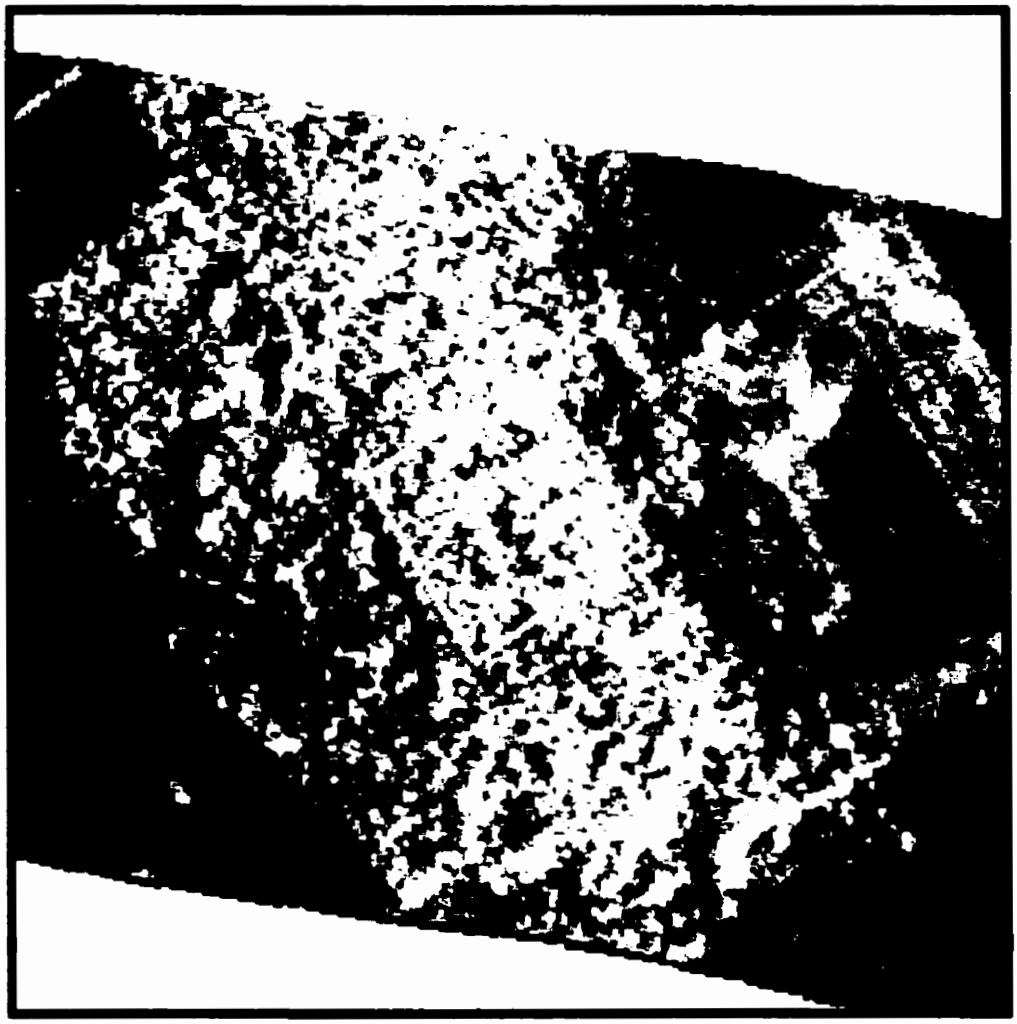

Figure 12: First-Derivative Image , 739 nm – ISD 21

Figure 13 represents the second-derivative image of the same area (739 nm). Visual interpretation of the image is not intuitive, because it contains values describing the rate at which reflection changed from one channel to another (i.e. acceleration on the curve – or the quantity of slope change from one channel to the next). To interpret it requires knowledge of the reflectance curve (Figure 10) and the derivative curve (Figure 11). At this wavelength, darker areas represent vegetation, because there is a large decrease in slope change in this portion of the red edge. In other words, this wavelength (739 nm) is the portion of the red edge that is concave down.

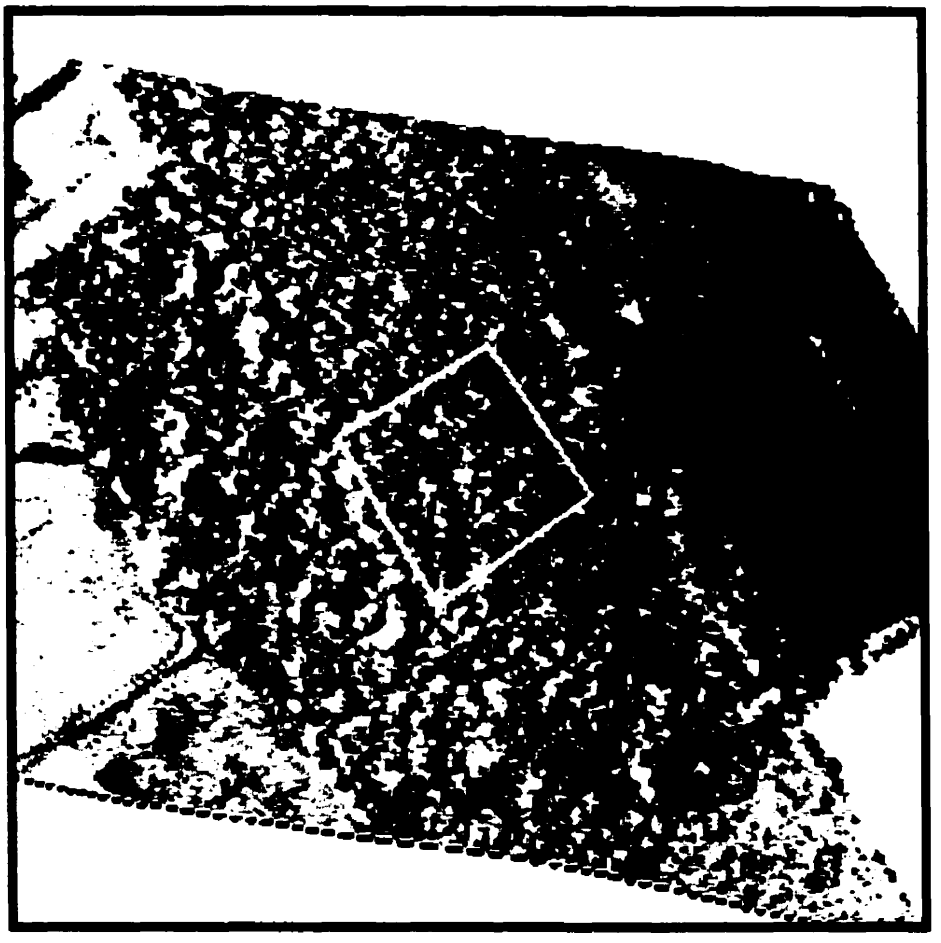

Figure 13: 2nd Derivative Image, 739 nm – ISD 21

The REIP image in Figure 14 was calculated by interpolating the wavelength at which the second derivative was equal to zero. The histogram indicates that most of the REIP wavelengths range from 710 nm – 730 nm. In the REIP image, dark red is normal healthy vegetation. Light orange and yellow represent vegetation for which the REIP was shifted toward the blue end of the EM spectrum. This could be due to stress, different species composition within the pixel, or variable canopy closure (some shadow fraction). Green represents mixed pixels, with vegetation combined with other surface features, as would occur in fields, shadows, etc. Blue and black are non-vegetated surfaces.

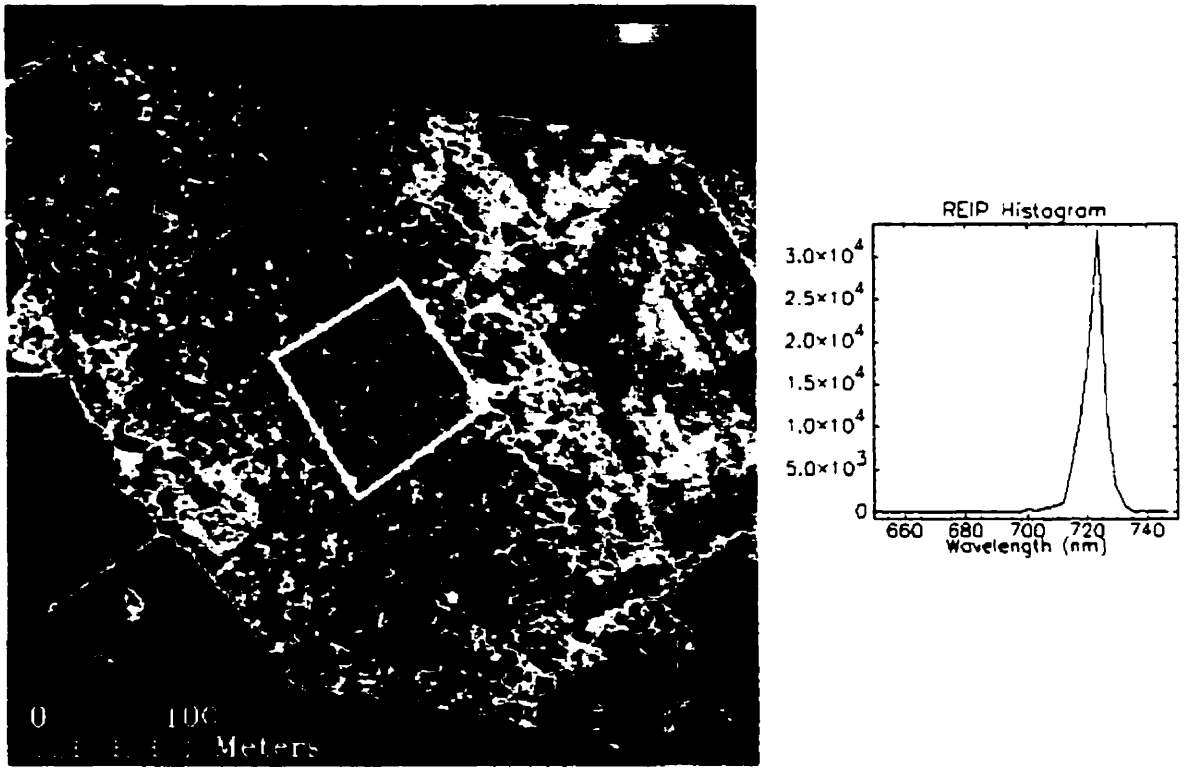

Figure 14: REIP Image and Histogram - ISD 21

Integrating under the spectral curve also resulted in an image for each of the study sites (Figure 15). Because the reflectance curve (Figure 10) contains only positive values, the image can be thought of as the total area under the spectral reflectance curve for each pixel. Darker values indicate a smaller area, meaning the reflectance in each channel is low for that pixel (e.g., shadow and wet areas). Vegetation would tend to exhibit green – red colours, because of the large area under the NIR region of the curve.

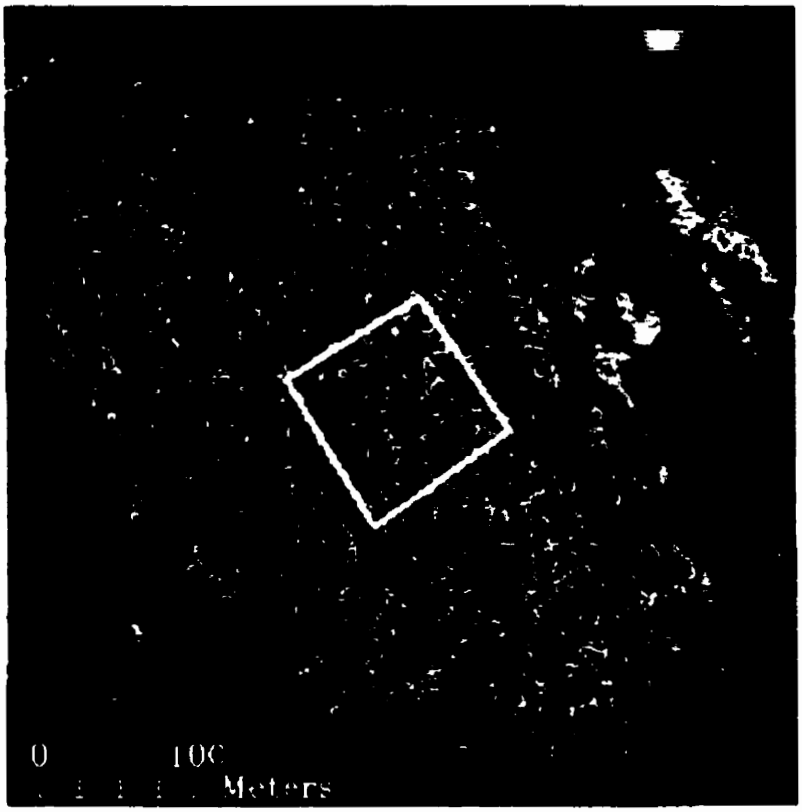

Figure 15: Integral Image for ISD 21

4.2.2 Geostatistical and Texture Indices

To consider anisotropic effects, transects were extracted in two perpendicular directions from each image channel at each ISD and FH site. This equated to

approximately 6,800 semivariograms to be modelled for the extraction of an optimal range in the N-S and E-W directions. Sample N-S and E-W variograms and their spherical models are presented in Figures 16 and 17 for ISD plot 21, at 739 nm. Range values varied with wavelength and direction (i.e., ranging from 2 m to 33 m). Optimal range values for each channel in the two perpendicular directions are presented in Appendix A.5.

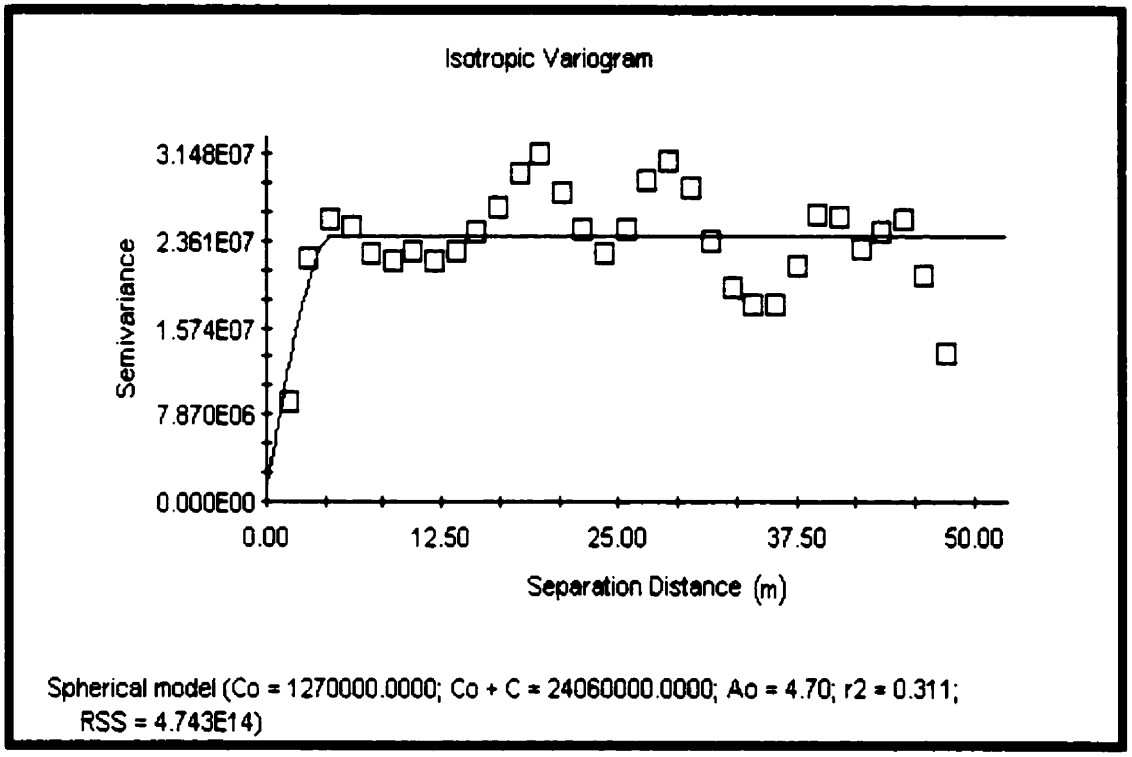

Figure 16: N-S Semivariogram, ISD 21, 739 nm

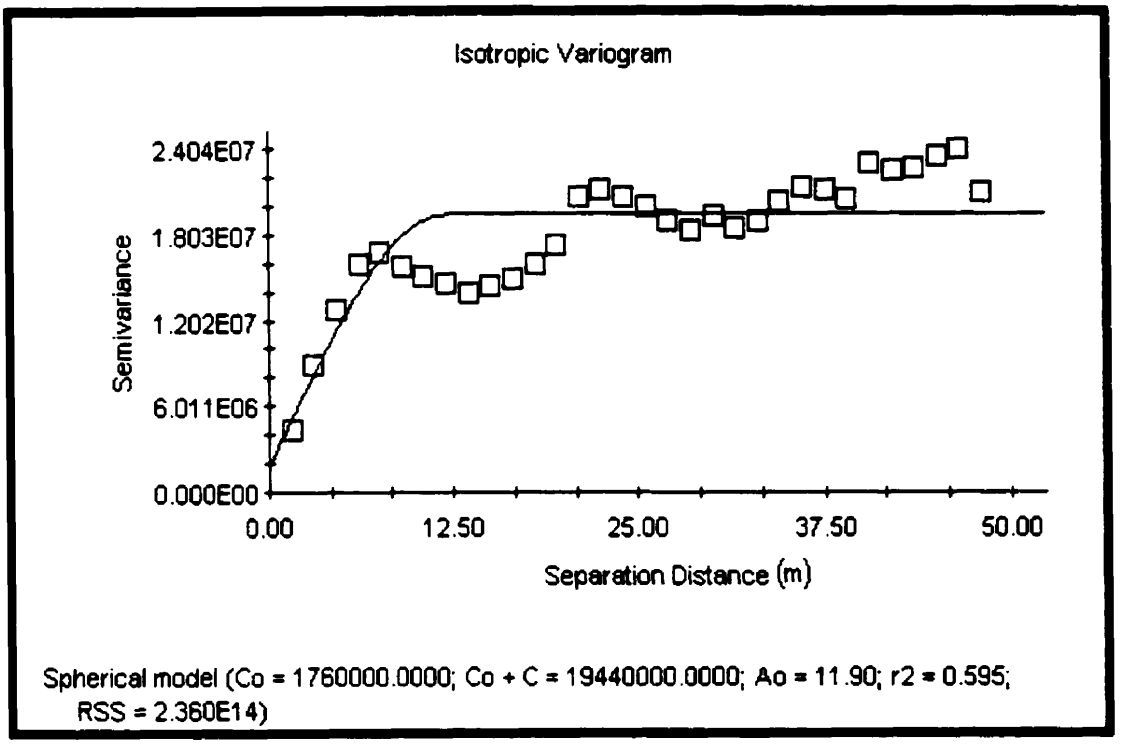

Figure 17: E-W Semivariogram, ISD 21, 739 nm

ISD site 21, at 739 nm, was used to illustrate the calculated texture measures. In this case, five first-order and eight second-order texture features were derived for each of the reflectance images, first- and second-derivative images, the REIP image, and the integral image. Figures 18-21 illustrate examples of the first-order texture images derived from the reflectance, first- and second-derivative, and REIP images at 739 nm for ISD 21 (outlined in purple). In these figures, range, mean, and variance are common first-order statistics that are more intuitive for visual interpretation. Range and variance values are higher in areas that have greater variability, such as the forest canopy (when derived from reflectance at 739 nm), and low in areas that are relatively uniform (i.e. fields). First-order mean resembles the original image, only smoother (this texture feature is commonly used to remove noise). Entropy, a measure of disorder or

randomness in the image, is low when the image is uniform within the filter. Although some variation can be seen in the field areas, the differences between most pixels were very slight, with a few pixels having a dramatic variation. This gave the entropy images a "binary" appearance, making them very difficult to interpret visually. Skew, described in Chapter 3 as lack of symmetry, is low when change is uniform (or symmetrical) within the filter (i.e., within the tree crowns of the reflectance image) and higher where the change is non-symmetrical (i.e., fields with rows, forest plantations, etc.).

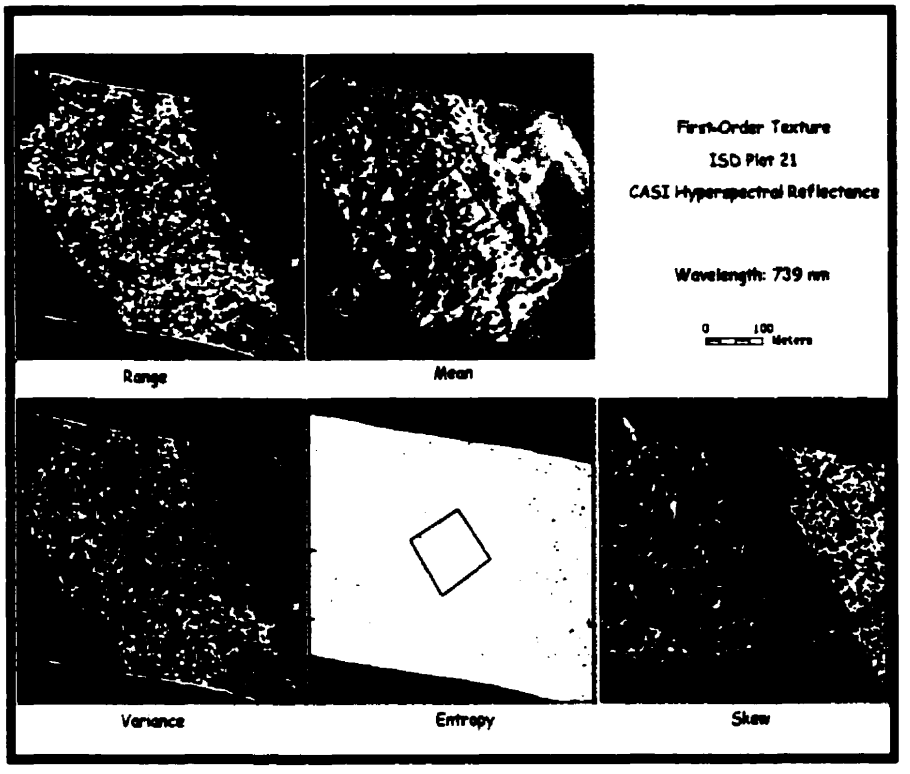

Figure 18: First-Order Texture From Reflectance – ISD 21

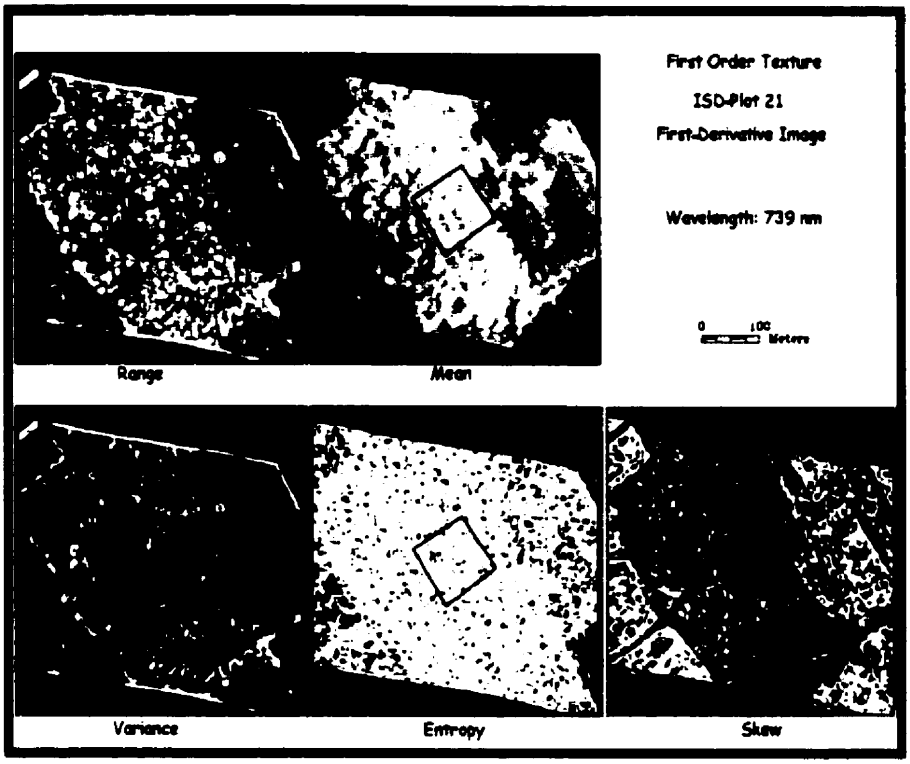

Figure 19: First-Order Texture From First-Derivative Image – ISD 21

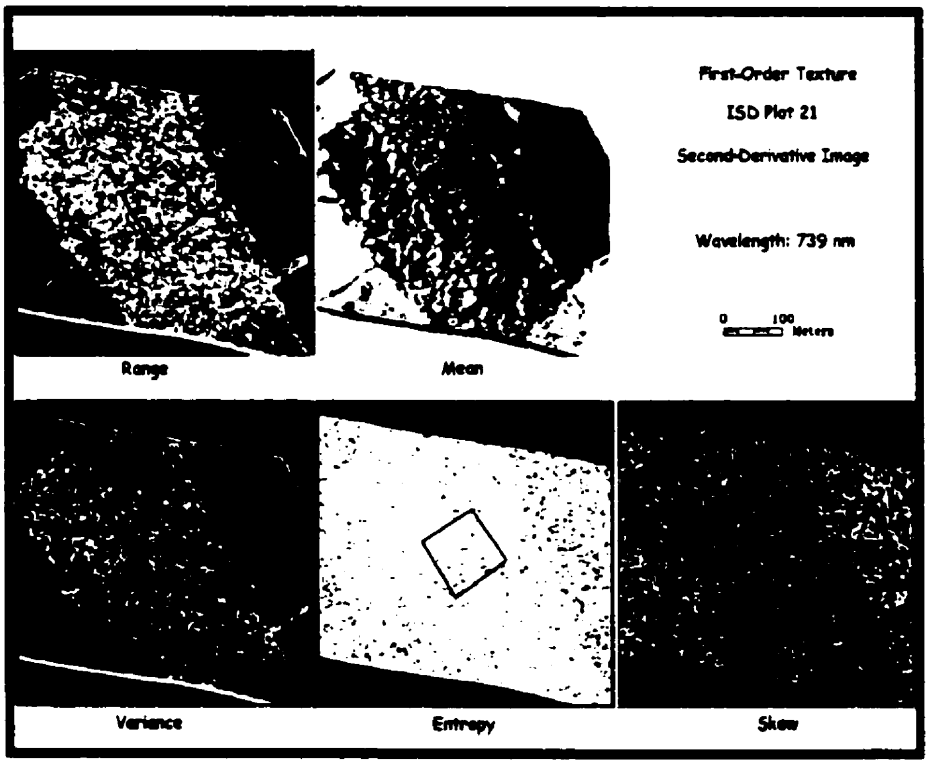

Figure 20: First-Order Texture From Second-Derivative Image– ISD 21

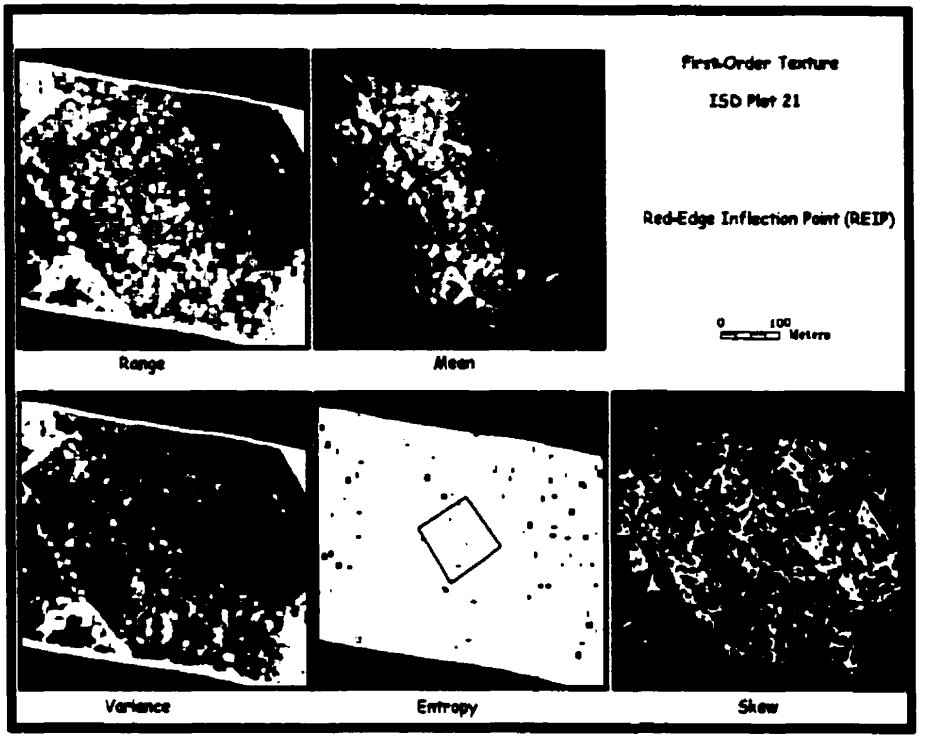

Figure 21: First-Order Texture From REIP - ISD 21

Figures 22 to 25 present examples of the second-order texture features derived from the reflectance, first- and second-derivative, and REIP images at 739 nm for ISD 21. As discussed in Chapters 2 and 3, the second-order texture features are calculated from the GLCM. Second-order mean and variance behave in a very similar manner to first-order mean and variance. Contrast, dissimilarity, and homogeneity are three methods of assessing local variance within the filter. Contrast and dissimilarity have higher values in areas that had possess greater variance (i.e., the forest canopy at 739 nm) and lower values for more uniform areas (i.e., fields). Homogeneity behaves in an opposite manner, with higher values representing a more uniform area. Note that for this texture derivative calculated on the reflectance image, most of the image appears relatively uniform (because an adjacent pixel was specified as the neighbour), resulting in

a dark image, with a few brighter areas (again giving a "binary" appearance). Subtle differences are highlighted in the first- and second-derivative images providing more meaningful results. Entropy and angular second moment are almost opposites of each other. Angular second moment is a measure of certainty within the filter and can be thought of as a measure of the presence of structure or pattern (Yuan *et al.*, 1991). The value will be high if the image is relatively smooth, and low if there is uncertainty or randomness in the filter. At 739 nm (and the distance and direction specified, i.e., 1,1), entropy and angular second moment do not provide any real insight to the study area. This is likely due to multiple scattering within the canopy in the NIR (i.e., increased variability), which make the generation of the GLCM using an adjacent pixel ineffective for these two texture features in the NIR.

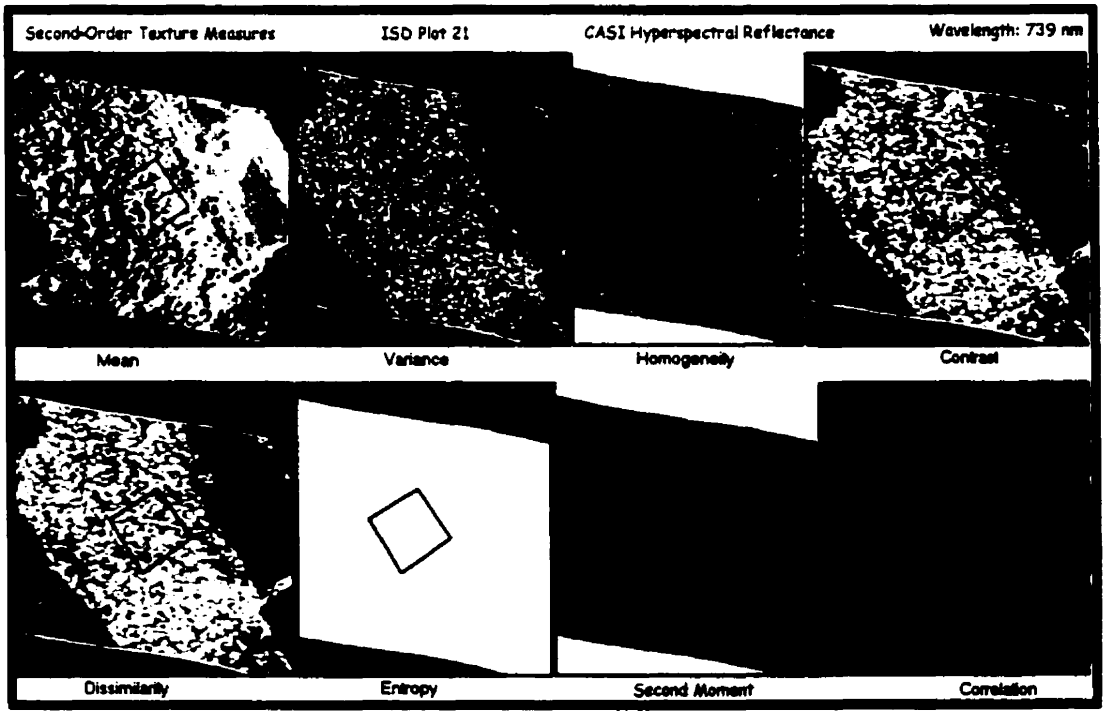

Figure 22: Second-Order Texture From Reflectance – ISD 21

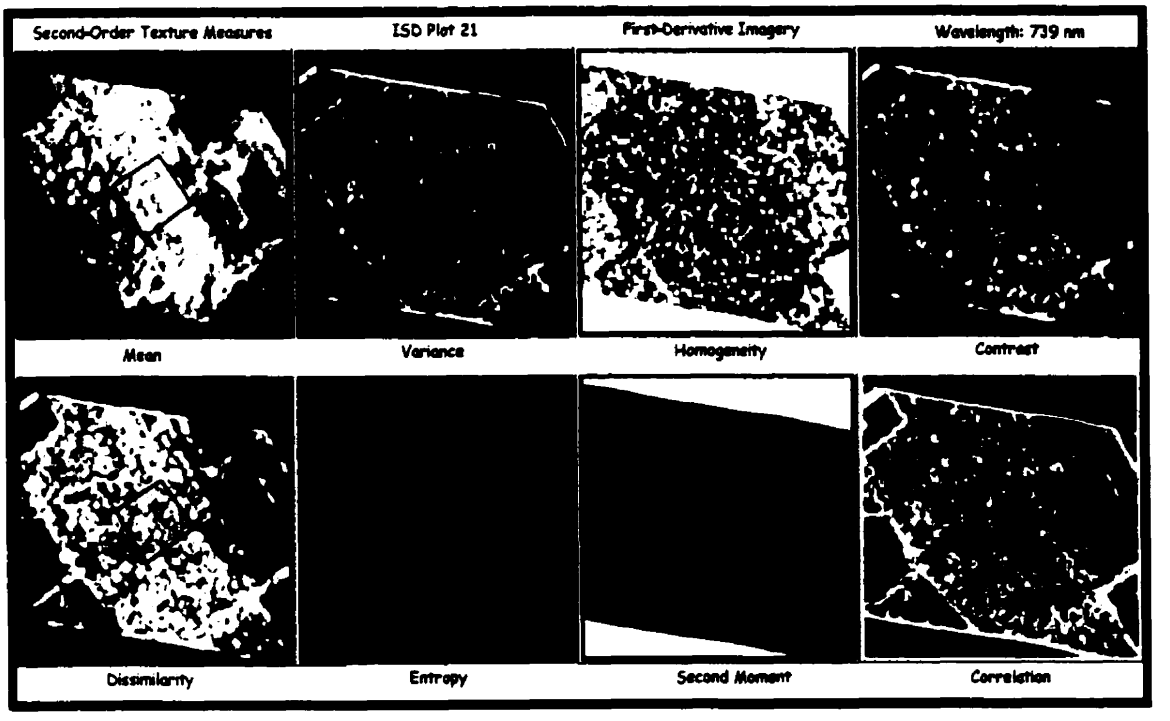

Figure 23: Second-Order Texture From First-Derivative Image – ISD 21

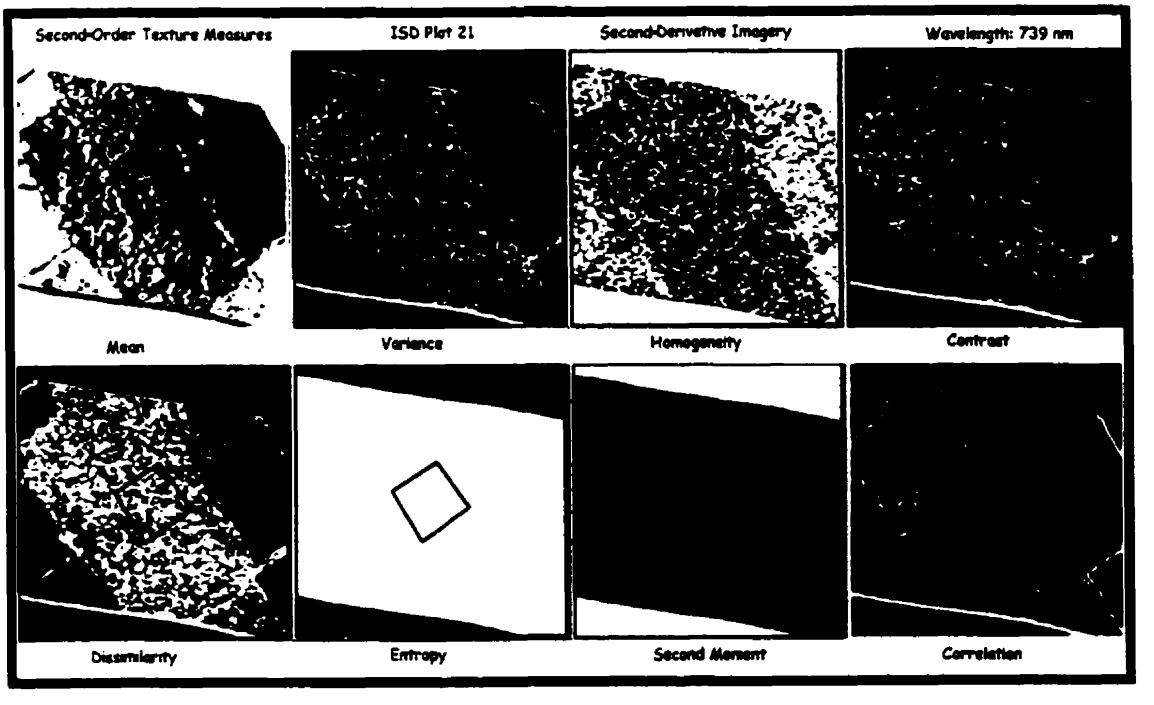

Figure 24: Second-Order Texture From Second-Derivative Image – ISD 21

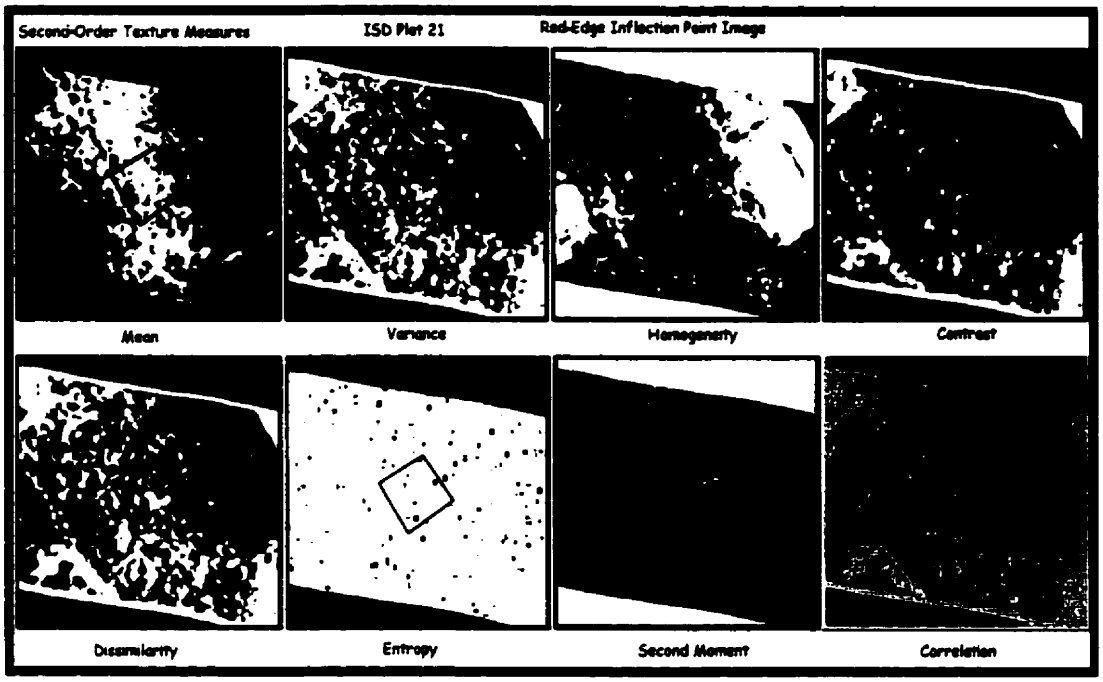

Figure 25: Second-Order Texture From REIP - ISD 21

4.3 Correlation Results – Spectral Indices (Calibration)

One of the challenges in the analysis of field metrics and hyperspectral data was the interpretation of a very large quantity of data/results. To gain an understanding of sources of redundancy within the field data, the first statistical assessment of the data was a multiple correlation analysis to identify how each of the field metrics related to one another. This was done to quantitatively confirm that the ground-based measurements were generally consistent with the expect results for a forest canopy. There are no particularly surprising or unusual results arising from this analysis. The key relationships are shown in Appendix A.7. As expected, both measures of DBH are highly correlated, as are the measures of crown closure. Relationships between metrics that are direct inputs into the calculations of other metrics are high. These included the relationships between

crown diameter / crown width and between crown closure / crown width / crown diameter.

Once the relationships within the field metrics were identified, it was then possible to correlate the field metrics with imagery. By writing computer programs, it was possible to explore thousands of relationships between (i) 246 individual channels (71 CASI channels; 71 first-derivative channels; 71 second-derivative channels; 1 REIP channel; 1 integral channel; and 31 narrow-band index channels), (ii) each of the forest metrics, and (iii) field sites. The total number of relationship calculations exceeded 500,000. Computer programs were written to identify some key results, which are presented below.

Significant relationships for the FH plots are presented in Table 3. At this stage in the analysis, the highest correlation found out of all the wavelengths was extracted and tested for significance, with no consideration given to consecutive channels with high correlations or any patterns in correlation trends across wavelengths. Results demonstrate that in every case, the highest correlations for the metrics are found with the derivative or REIP images. As expected, forest metrics that are highly correlated with each other are also highly correlated to the image at the same wavelengths. This can be seen with perpendicular crown width, major crown width, and crown diameter (all reporting the highest correlation at 498 nm) as well as with stem density and number of trees (854 nm). Note that the sample size for the control sites was very small (n=6), which may have led to inaccuracies in the statistical results (partially accounting for the high correlations).

Table 3: Index Correlations Derived From FH Plots (n=6)

Structural Parameter	r	r^2	INDEX: Image, Wavelength (nm)	Extraction Measure
DBH_{quad}	0.99	0.99	1st Derivative, 535	Mean
Basal Area	-0.93	0.88	1st Derivative, 893	Variance
Crown Closure (circular)	-0.97	0.94	1st Derivative, 671	Variance
Crown Diameter	-0.92	0.85	2nd Derivative, 498	Std. Dev.
Crown Depth	-0.91	0.83	2nd Derivative, 626	Std. Dev.
Crown Width (major)	-0.91	0.83	2nd Derivative, 498	Std. Dev.
Crown Width (perpendicular)	-0.91	0.84	2nd Derivative, 498	Std. Dev.
Stem Density	-0.95	0.89	2nd Derivative, 854	Mean
Height to Crown Base	-0.94	0.88	2nd Derivative, 431	Mean
Tree Height	0.94	0.88	1st Derivative, 431	Mean
Number of trees	-0.95	0.89	2nd Derivative, 854	Mean
LAI 4th ring	-0.88	0.77	REIP	Std. Dev.
LAI 5th ring	0.97	0.93	2nd Derivative, 468	Mean
Percent Opening	-0.98	0.95	2nd Derivative, 656	Std. Dev.

Significant relationships for the ISD plots are presented in Table 4. For these study sites, the openness of the canopy was more variable due to the damage cause by the ice storm. This, combined with a larger sample size (n=10), contributed to the general lowering of correlations. Again, results show that in every case, the highest correlations for the forest metrics are found with the derivative images. Note that for all metrics the wavelength of highest correlation varies from Table 3 to Table 4. This is due to the fact that only the highest correlation was extracted, without consideration of the correlation patterns across wavelengths. Examination of the correlation curves revealed that high correlations do exist for the metrics at both locations, but the wavelength of highest correlation differ. Note that high correlations of a few of the metrics in the visible region (i.e., percent opening, LAI, height, and DBH) are consistent across FH plots (Tables 3) and ISD plots (Table 4).

Table 4: Index Correlations Derived From ISD (n=10)

Structural Parameter	r	r^2	INDEX: Image, Wavelength (nm)	Extraction Measure
DBH_{quad}	0.86	0.74	1st Derivative, 416	Variance
Crown Closure (circular)	0.93	0.86	2nd Derivative, 520	Mean
Crown Diameter	0.88	0.78	2nd Derivative, 595	Mean
Crown Depth	-0.90	0.81	1st Derivative, 878	Variance
Crown Width (major)	-0.92	0.85	2nd Derivative, 870	Std. Dev.
Crown Width (perpendicular)	0.83	0.69	2nd Derivative, 595	Mean
Stem Density	-0.81	0.66	2nd Derivative, 924	Variance
Height to Crown Base	-0.83	0.70	2nd Derivative, 542	Variance
Tree Height	0.86	0.74	Reflectance, 408	Mean
Number of trees	-0.81	0.66	2nd Derivative, 924	Variance
LAI 4th ring	-0.87	0.75	2nd Derivative, 431	Mean
LAI 5th ring	0.93	0.86	2nd Derivative, 446	Mean
Percent Opening	-0.85	0.72	2nd Derivative, 446	Mean

To increase the robustness of the correlations between the field data and hyperspectral features, the FH and ISD plots were pooled and analyzed together. The results of these analyses are presented in Table 5, and demonstrate a general decrease in correlations. Although a pattern in these results is difficult to detect, there are consistencies when examining parameters that are highly correlated (i.e., measures of crown closure, crown diameter and canopy width, and LAI and percent canopy opening). Note the correlation of the derivative images at 498 nm to crown diameter/perpendicular crown width, suggesting a spectral feature within blue/green region. Again, for most metrics, the first- and second-derivative images contain the channel with the highest correlations.

Table 5: Index Correlations Derived From Pooled FH and ISD Plots (n=16)

Structural Parameter	r	r^2	INDEX: Image, Wavelength (nm)	Extraction Measure
DBH_{quad}	0.79	0.63	2nd Derivative, 831	Mean
Basal Area	-0.65	0.42	1st Derivative, 610	Variance
Crown Closure (circular)	0.74	0.55	Reflectance, 431	Mean
Crown Closure (ellipse)	0.76	0.57	Reflectance, 431	Mean
Crown Diameter	-0.83	0.70	1st Derivative, 498	Mean
Crown Depth	-0.73	0.54	Reflectance, 686	Std. Dev.
Crown Width (major)	0.76	0.58	2nd Derivative, 932	Variance
Crown Width (perpendicular)	-0.87	0.75	1st Derivative, 498	Mean
Stem Density	-0.78	0.60	1st Derivative, 916	Mean
Height to Crown Base	-0.85	0.73	1st Derivative, 535	Variance
Tree Height	-0.78	0.61	2nd Derivative, 409	Mean
Number of trees	-0.85	0.72	1st Derivative, 762	Std. Dev.
LAI 4th ring	-0.72	0.51	1st Derivative, 747	Std. Dev.
LAI 5th ring	-0.73	0.54	1st Derivative, 461	Mean
Percent Opening	0.81	0.66	1st Derivative, 747	Std. Dev.

4.4 Correlation Results – Spectral/Spatial Indices (Calibration)

In many cases, geostatistical and texture analysis notably improved relationships between forest metrics and the spectral/spatial indices. The highest correlations found between the forest metrics and the geostatistical/texture indices for the pooled FH and ISD sites are presented in Table 6. At first review, these results do not appear to have a lot in common with Tables 3 to 5, mainly due to the presentation of the highest correlation rather than correlation patterns. However, there are some observations than can made from these results that are consistent amongst metrics. For example, the first- and second-order derivative texture images have higher correlations than the reflectance texture images. Second, texture improves the correlation for most metrics. Third, crown diameter and perpendicular crown width once again have strong correlations for images derived from the 498 nm data, suggesting a "real" feature at this wavelength. Finally, the

results have shown that presentation of the highest correlations found between the image and the structural parameter without consideration of correlation patterns across wavelengths can be very difficult to interpret (and possibly misleading). However, presentation of results in this manner has been reported on multiple occasions (e.g., Merton, 1998; Thenkabail *et al.*, 1999). These results suggest that a more appropriate method to extract "optimal" or robust correlations would be an examination of the correlation patterns across image channels.

Table 6: Index Correlations For Texture Features From Pooled FH and ISD Sites (n=16)

Structural Parameter	r	r^2	INDEX: Image, Texture, Wavelength (nm)	Extraction Measure
DBH_{quad}	0.82	0.67	2nd Derivative, skew, 893	Mean
Basal Area	0.84	0.71	2nd Derivative, skew, 513	Std. Dev.
Crown Closure (circular)	0.90	0.82	1st Derivative, 1st Order Variance, 793	Mean
Crown Closure (ellipse)	0.90	0.81	1st Derivative, 1st Order Variance, 793	Mean
Crown Diameter	-0.83	0.69	1st Derivative, 1st Order Mean, 498	Mean
Crown Depth	0.86	0.73	1st Derivative, homogeneity, 641	Variance
Crown Width (major)	0.89	0.79	1st Derivative, 2nd Order Variance, 939	Mean
Crown Width (perpendicular)	-0.86	0.75	1st Derivative, 1st Order Mean, 498	Mean
Stem Density	-0.77	0.60	1st Derivative, 1st Order Mean, 916	Mean
Height to Crown Base	-0.91	0.82	2nd Derivative, 2nd Order Variance, 513	Mean
Tree Height	0.87	0.75	2nd Derivative, Skew, 808	Std. Dev.
Number of trees	0.84	0.71	1st Derivative, Skew, 641	Mean
LAI 4th ring	-0.85	0.72	2nd Derivative, Dissimilarity, 755	Variance
LAI 5th ring	0.86	0.73	1st Derivative, Skew, 603	Mean
Percent Opening	0.92	0.85	2nd Derivative, Skew, 648	Std. Dev.

4.5 Spectral/Spatial Regions of Correlation

Correlation curves for each metric were examined to extract indices with promising correlations for two or more consecutive channels. These indices (along with

the single highest correlations shown above) were then tested for robustness in the validation analysis. This produced a large volume of information, with more than one wavelength region investigated for each metric. To assist with the interpretation of results, metrics were grouped according to their similarities. Within these groups, only metrics that showed promise for the validation analysis are presented below.

4.5.1 DBH

Both measures used to estimate DBH (arithmetic and quadratic) are similar, with the same general pattern in the correlation curves. Results indicate that quadratic DBH has a slightly higher correlation with the reflectance data and their derivatives. The variations in correlation between quadratic DBH and the reflectance and calculus image channels are illustrated in Figure 26.

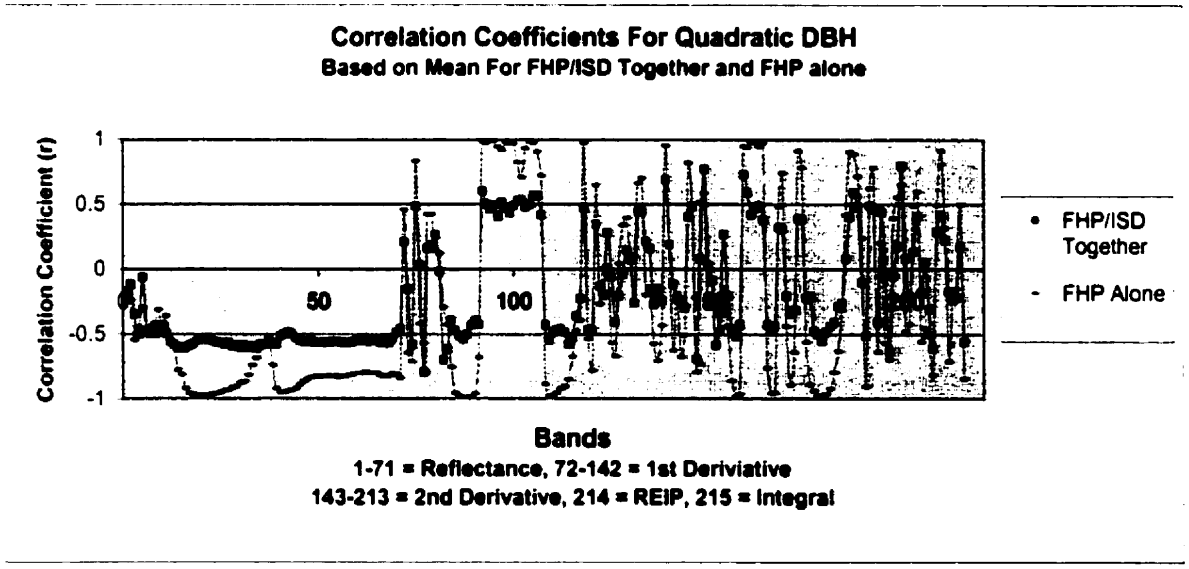

Figure 26: Correlation Curve For Quadratic DBH

Although the magnitude of the correlation coefficients varies for each extraction method, the pattern remains relatively consistent across the entire channel range. When

examining the correlations derived from the pooled sites, no two consecutive channels have a correlation with $r > 0.7$ (Figure 26). However, several regions exhibiting high correlations are observed when examining FH sites, which suggests that there are high correlations between DBH and the images for undamaged, closed canopy conditions. To assess this, wavelength regions were identified where at least two consecutive channels had a correlation of $r > 0.9$ for FH alone (Table 7). Although texture analysis produces a higher correlation for the permutations of interest at a single wavelength (Table 6), none of the texture measures improve the correlations across multiple wavelengths for this metric.

Table 7: Extracted Channel Ranges For Quadratic DBH

Wavelength Range (nm)	Image	Comments
520-618	CASI reflectance	14 channels in the green/red
693-731	CASI reflectance	6 channels in the red edge
505-543	First derivative	6 channels in the green
558-618	First derivative	9 channels in the green/red
641-663	First derivative	4 channels in the red
686-717	First derivative	5 channels in the red edge
513-565	Second derivative	8 channels in the green
663-694	Second derivative	5 channels in the red

4.5.2 Metrics Derived From Measures of Crown Width

There were five metrics derived from field measurements of crown width. These included 1) major crown width; 2) perpendicular crown width; 3) crown diameter; 4) circular crown closure; and 5) elliptical crown closure. Results illustrate two main commonalities amongst the indices for these metrics: 1) channels along the red edge, from the absorption well to approximately the REIP, have the highest correlations, and 2)

use of standard deviation to extract reflectance values from the image result in the highest correlations.

Examination of major and perpendicular crown width indicate that correlations with the original reflectance and derivative images are generally low. Texture improves correlations considerably for both metrics, resulting in strong correlations along the red edge. Somewhat weaker relationships are also found in the blue region for both metrics. Correlations across multiple channels are notably stronger for perpendicular crown width than for major crown width. Examination of both circular and elliptical crown closure reveal multiple wavelengths in the green peak region and along the red edge to have strong correlations with these metrics. Specifically, the original CASI reflectance image is correlated to both metrics in multiple channels of the green region. After geostatistical and texture analysis, the reflectance imagery had multiple channels with high relationships in the blue and red edge. The derivative images are not as highly correlated to these metrics. Circular crown closure relationships are slightly stronger than elliptical relationships, although the two metrics have generally similar results. Crown diameter, which was calculated using the mean of the two crown width measurements, generally has low correlations ($r<0.7$) when examining multiple consecutive image channels. Geostatistical and texture analysis, in particular second-derivative homogeneity, improve the relationships in the NIR to give two consecutive channels with $r>0.7$. However, in comparison with the other crown-width metrics, the relationships with crown diameter are not promising.

To simplify the results for these metrics, only the most promising correlation curves are presented below. It should be noted that there are multiple correlation curves

(i.e. there were multiple indices) for each metric that suggested potentially promising ranges of channels. All indices that showed promise were investigated further in the validation analysis. The range correlation curve for circular crown closure and the first-order mean texture index for perpendicular crown width are illustrated in Figure 27. The first-order mean texture index for perpendicular crown width is also illustrated. The most promising consecutive wavelengths for the five metrics are listed in Table 8 (the lowest correlations in the table were for crown diameter at r=0.7).

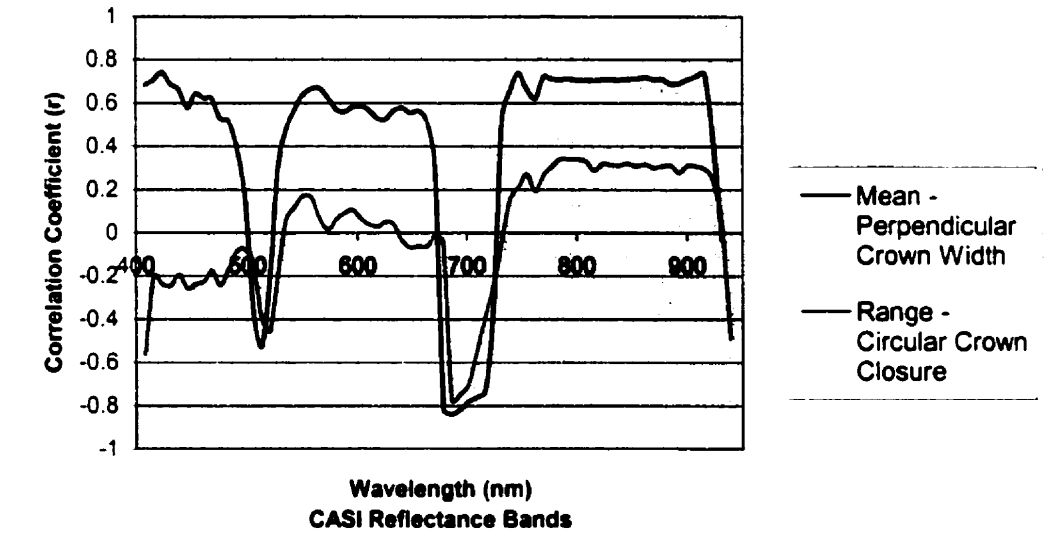

Figure 27: Correlation Curves For Crown Width And Crown Closure

Table 8: Channel Ranges (r>0.7) For Crown-Width Metrics

Metric	Wavelength Range (nm)	Index	Comments
Major Crown Width	520-528	Skew of first derivative	2 channels in the green peak
	932-939	Standard deviation of second derivative	2 channels in the NIR
Perpendicular Crown Width	686-701	First-order mean of CASI reflectance	3 channels in the red edge
	694-701	Dissimilarity of CASI reflectance	2 channels in the red edge
Circular Crown Closure	686-694	Range of CASI reflectance	3 channels in the red edge
Elliptical Crown Closure	483-498	Second-order mean of CASI reflectance	3 channels in the blue
	686-694	Range of CASI reflectance	3 channels in the red/red edge
Crown Diameter	785-793	Homogeneity of second derivative	2 channels in the NIR

4.5.3 Metrics Derived From Measures of Tree Height

The three metrics related to measures of height include: 1) height to the base of the canopy; 2) crown depth; and 3) tree height. For each of these metrics, geostatistics and texture analysis considerably improve the relationships between the indices and the metrics. Results indicated that height to the base of the canopy has notably higher relationships with the data, with several wavelength regions and texture measures giving a correlation coefficient greater than 0.85. Strong correlations for this metric are found in the second-derivative for green wavelengths, and in sections of the red edge on both sides of the inflection point for the reflectance and first-derivative images. Tree height and crown depth indices have lower correlations, although several wavelength ranges were identified that have correlation coefficients between r=0.7-0.8. For tree height and height

to the crown base, first-order mean indices have the strongest relationships with the metrics. Although the strength of the relationships varies, the general shape of the correlation curve for these two metrics is very similar. Crown depth has stronger relationships with second-order indices, including homogeneity and entropy.

The first-order mean index for height to the base of the canopy is the most promising for the height metrics. Figure 28 illustrates the correlation curve for this metric. Table 9 lists the most promising wavelength ranges identified for each of these metrics, each of which is further examined in the validation analysis.

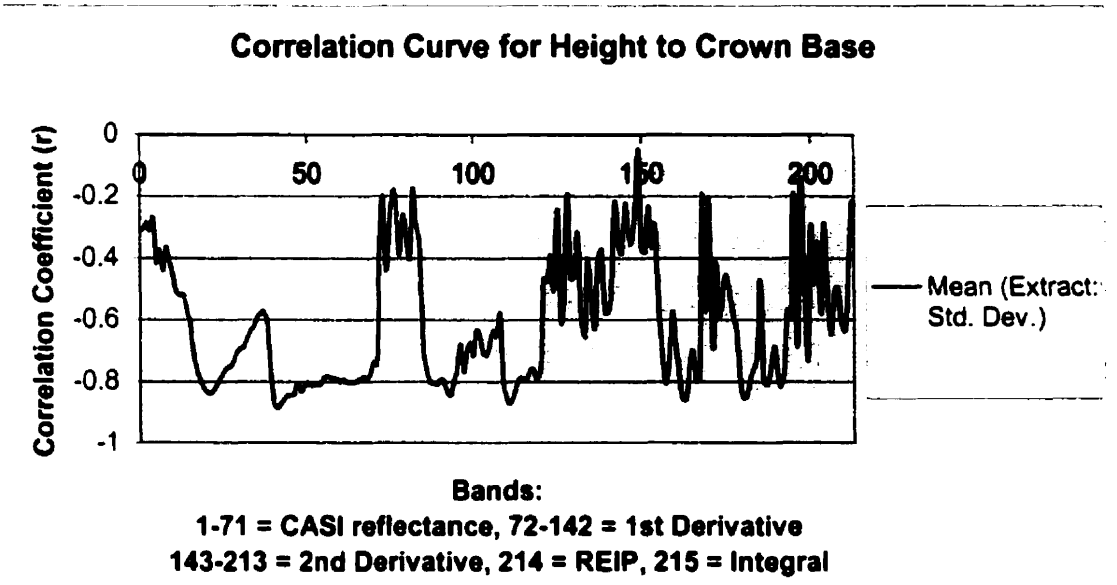

Figure 28: Correlation Curve For Height To The Base Of The Canopy

Table 9: Channel Ranges (r>0.7) For Height Metrics

Metric	Wavelength Range (nm)	Index	Comments
Height to crown base	550-558	First-order mean of second derivative	2 channels in the green
	694-709	First-order mean of first derivative	3 channels on the red edge
	701-724	First-order mean of CASI reflectance	4 channels on the red edge to the REIP
	717-732	Variance of CASI reflectance	3 channels around the REIP
Tree height	558-565	First-order mean of first derivative	2 channels in the green
	694-701	First-order mean of first derivative	2 channels in the red edge
	701-717	First-order mean of CASI reflectance	2 channels in the red edge
Crown depth	595-610	Entropy of first and second derivative	3 channels in the green/red
	626-633	Homogeneity of CASI Reflectance	2 channels in the red
	717-732	Homogeneity of first derivative	3 channels around the REIP
	923-931	Homogeneity of first derivative	2 channels in the NIR

4.5.4 Metrics Derived From Number of Trees

There were three metrics derived from the number of trees in the study plots. These include: 1) basal area (which also incorporates DBH); 2) stem density; and 3) number of trees. Basal area is not well correlated to images across consecutive channels. Although texture does appear to improve the correlations in most wavelengths the relationships are not strong enough to pursue with this multiple wavelength approach ($r<0.7$). More promising are the results from the number of trees, and to a lesser extent stem density. The number of trees within plots has strong correlations in the proximity of the red edge for the reflectance and derivative images. Texture measures of skew and first-order mean further strengthen these relationships, with targeted wavelengths having $r>0.8$. The strongest relationships for stem density ($r>0.7$) occur in the first-order mean

image in the NIR region of the spectrum. The first-order mean correlation curves for number of trees and stem density are presented in Figure 29. The most promising wavelength ranges that were targeted for further investigation are presented in Table 10.

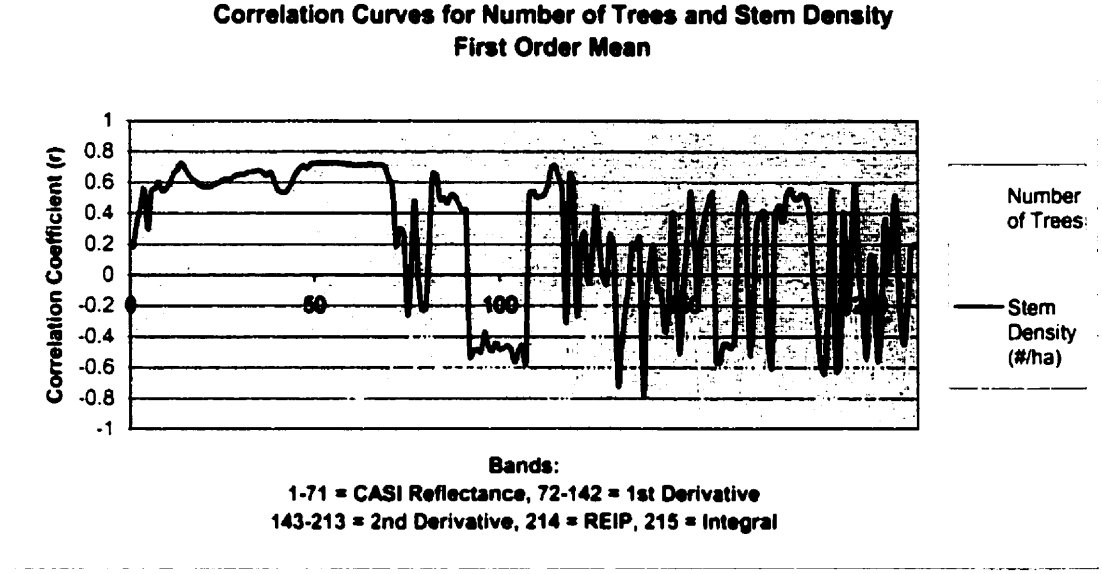

Figure 29: Correlation Curve For Number Of Trees And Stem Density

Table 10: Channel Ranges (r>0.7) For Number Of Trees And Stem Density

Metric	Wavelength Range (nm)	Index	Comments
Number of Trees	694-717	First-order mean of CASI reflectance	4 channels on the red edge
	641-648	Skew of first derivative	2 channels in the red absorption well
	724-747	First-order mean of first derivative	4 channels on the red edge, around the REIP
	739-755	First-order mean of second derivative	2 channels on the red edge
Stem Density (#/ha)	778-831	First-order mean of CASI reflectance	8 channels in the NIR

4.5.5 Metrics Derived From Hemispherical Photographs

The final group of metrics included those that were derived from the hemispherical photographs, including LAI and percent canopy openness. LAI values derived using the five rings (full field of view) have consistently lower correlations than LAI derived from four rings (0-60^0 field of view), and are not discussed further here. When examining LAI derived from the inner four rings, the correlations for the original reflectance and calculus images are generally low. Texture provides notable improvements for all of the metrics derived from hemispherical photos. For LAI, dissimilarity texture indices gives correlations of $r>0.77$ in the NIR of the first-derivative image. Percent canopy openness is well correlated ($r>0.8$) to multiple texture indices and is the most promising of all metrics examined. Figure 30 illustrates the dissimilarity correlation curves for both metrics, while Table 11 lists the more promising indices investigated further in the validation analysis.

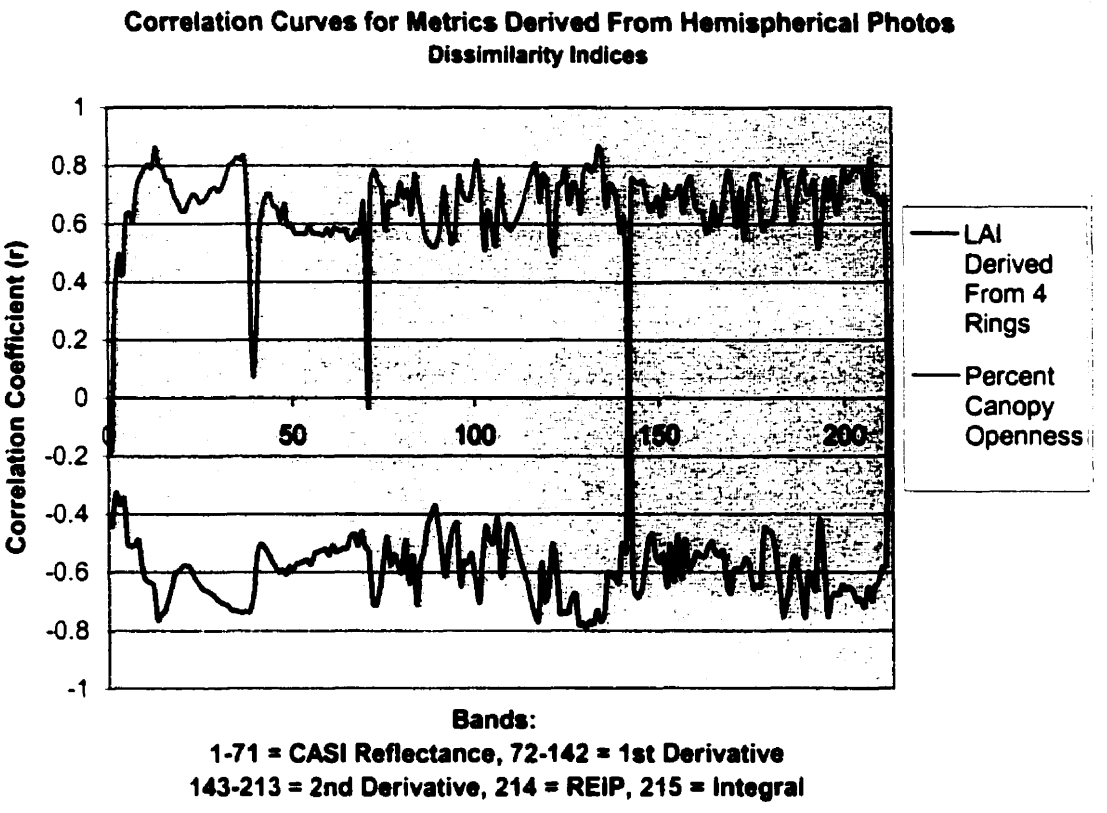

Figure 30: Correlation Curves For Metrics Derived From Hemispherical Photos

Table 11: Channel Ranges (r>0.7) For Metrics Derived From Hemispherical Photos

Metric	Wavelength Range (nm)	Index	Comments
LAI (4 rings)	831-862	Dissimilarity of the 1st derivative	4 channels in the NIR
Percent Canopy Openness	476-483	Range of CASI reflectance	2 channels in the blue
	498-505	Dissimilarity of CASI reflectance	2 channels in the blue/green
	663-686	Dissimilarity of CASI reflectance	4 channels in the red
	603-610	Second Moment of 1st derivative	2 channels in the red
	641-648	Second Moment of 1st derivative	2 channels in the red
	801-808	Dissimilarity of 1st derivative	2 channels in the NIR
	846-862	Dissimilarity of 1st Derivative	3 channels in the NIR
	878-885	Dissimilarity of 1st Derivative	2 channels in the NIR

4.6 Validation of Indices

By examining the extracted wavelength ranges, a number of relationships were discovered that agreed with the validation data from the TLW. All correlations were tested for statistical significance. Only those indices that were statistically significant at 95% confidence intervals are reported here.

Several indices and wavelengths proved to have strong relationships with percent canopy openness calculated from the hemispherical photos. Other metrics with which developed indices are consistent include LAI, crown diameter, perpendicular canopy width, number of trees, and crown depth. These metrics and their relationships for both the calibration and validation sites (ice storm damage/FH and TLW respectively) are presented in Tables 12 to 16. Results from the validation analysis highlight three significant consistencies: 1) standard deviation is the most robust method to extract pixel values from the images; 2) dissimilarity, second moment, and homogeneity appear to be more robust than the other texture features examined; and 3) clear cut conditions are not well correlated to the indices.

Table 12: Validated Indices For Percent Canopy Openness (hemispherical photos)

Index	Calibration Sites (FH and ISD)			Validation Sites (TLW)			Comments
	r	r^2	n	r	r^2	n	
Dissimilarity at 505 nm; extracted by standard deviation	0.83	0.69	16	0.82	0.67	8	Control
Second Moment at 610 nm; extracted by standard deviation	0.80	0.64	16	0.81 0.70	0.66 0.49	8 12	Shelterwood Shelterwood & Selected Cut
Second Moment at 558 nm – 1st Derivative; extracted by standard deviation	0.82	0.67	16	0.86 0.62	0.74 0.39	8 12	Shelterwood Shelterwood & Selected Cut
Second Moment at 648 nm – 1st Derivative; extracted by standard deviation	0.85	0.72	16	0.88 0.75	0.77 0.56	8 12	Shelterwood Shelterwood & Selected Cut

Table 13: Validated Indices For LAI (derived from four inner rings)

Index	Calibration Sites (FH and ISD)			Validation Sites (TLW)			Comments
	r	r^2	n	r	r^2	n	
Dissimilarity at 595 nm – 2nd Derivative; extracted by standard deviation	-0.65	0.43	16	-0.93	0.86	8	Control
Dissimilarity at 717 nm – 2nd Derivative; extracted by standard deviation	-0.71	0.5	16	-0.99	0.98	4	Selected Cut

Table 14: Validated Indices For Crown Diameter

Index	Calibration Sites (FH and ISD)			Validation Sites (TLW)			Comments
	r	r^2	n	r	r^2	n	
Homogeneity at 565 nm – 2nd Derivative; extracted by standard deviation	0.71	0.50	16	0.76	0.58	8	Shelterwood
Homogeniety at 785 nm – 2nd Derivative; extracted by standard deviation	0.70	0.49	16	0.74 0.66	0.55 0.44	8 13	Shelterwood Shelterwood & Selected Cut

Table 15: Validated Indices For Number Of Trees

Index	Calibration Sites (FH and ISD)			Validation Sites (TLW)			Comments
	r	r^2	n	r	r^2	n	
First Order Mean at 732 nm – 1st Derivative; extracted by standard deviation	-0.82	0.67	16	-0.89	0.79	5	Selected Cut
Second Order Mean at 732 nm – 1st Derivative; extracted by standard deviation	-0.81	0.66	16	-0.89	0.79	5	Selected Cut

Table 16: Validated Indices For Crown Depth

Index	Calibration Sites (FH and ISD)			Validation Sites (TLW)			Comments
	r	r^2	n	r	r^2	n	
Entropy at 446 nm – 2nd Derivative; extracted by variance	0.71	0.50	16	0.89 0.68	0.79 0.46	5 11	Selected Cut Clear cut

4.7 Predictive Indices

Percent canopy openness derived from the hemispherical photos possessed the strongest relationships with the indices at both the calibration and validation sites. Dissimilarity at 505 nm of the reflectance image, which has a high correlation with the

pooled calibration sites and held for the control sites in TLW (Table 12), was selected to derive predictive indices. As mentioned in Chapter 3, development of predictive indices is a future stage of research, which would be very useful for deriving structure maps at a regional or provincial scale. For illustrative purposes, the correlation equation was modelled from the scatterplot of the dissimilarity index versus percent canopy openness to derive a predictive index (Figure 31). Results in Table 12 indicate that this predictive index is only valid for control areas (undamaged, closed canopy) as well as the areas in which the index was developed (ISD and FH).

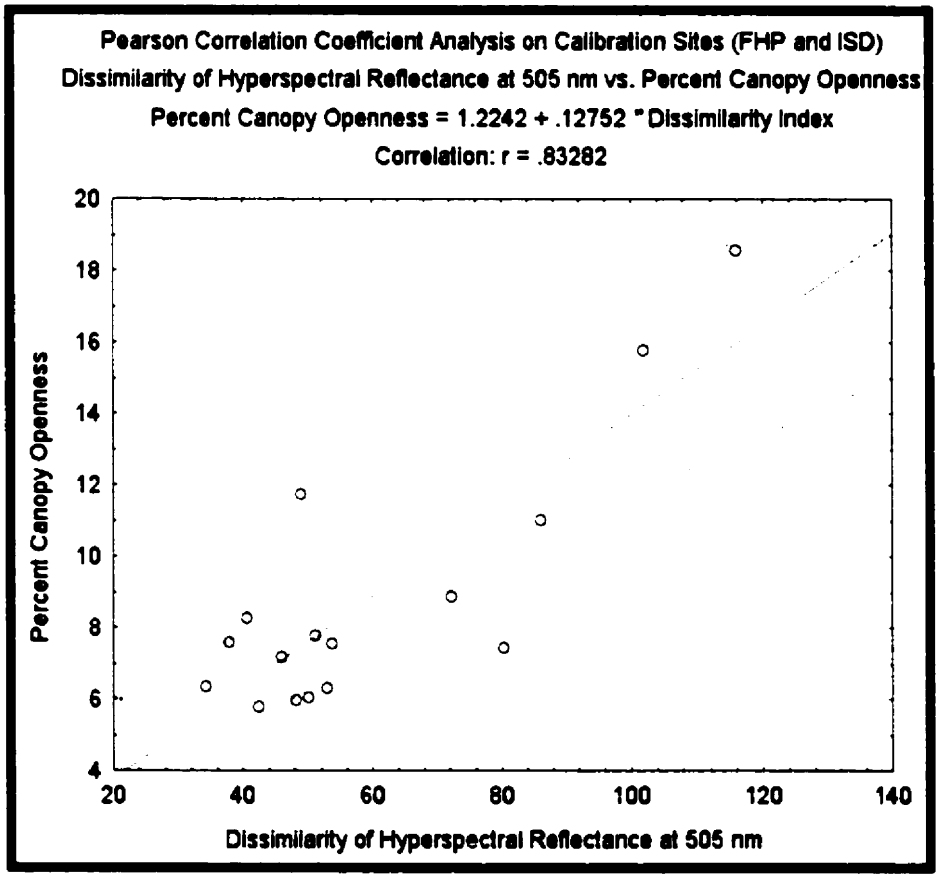

Figure 31: Pearson Correlation For Dissimilarity Index vs. Percent Canopy Openness

With a correlation of r=0.83, the predictive index derived from the calibration sites can be taken as the correlation equation in Figure 31:

% Canopy Openness = 1.2242 + 0.12752*(Dissimilarity of reflectance at 505 nm) (23)

The predictive index for percent canopy openness was then applied to the Turkey Lakes image data to obtain a percent canopy openness map from which percent canopy openness could be quantitatively extracted directly from each pixel for control areas. A percent canopy openness map for two control areas in Turkey Lakes (Area #1 located within the harvest treatment study area and Area #2 located outside of it), with the validation sites outlined is displayed in Figure 32. Table 17 lists the area percentages for openness in the control areas. These values were calculated within a GIS by dividing the number of pixels of each percentage class (Figure 32) by the total number of pixels within the two control areas (each has an area of 4 m^2) and multiplying by 100%. Statistics for the validation sites are included in Table 18. This table compares the mean and maximum values of percent canopy openness predicted in the GIS for the validation sites (Figure 32) with the mean value of percent canopy openness derived from the hemispherical photos. Modelled predictions are within approximately 3-4% of the known value for the validation sites. Again, this is presented as a demonstration of the technique of deriving predictive maps. The results are only valid for the control areas outlined in Figure 32.

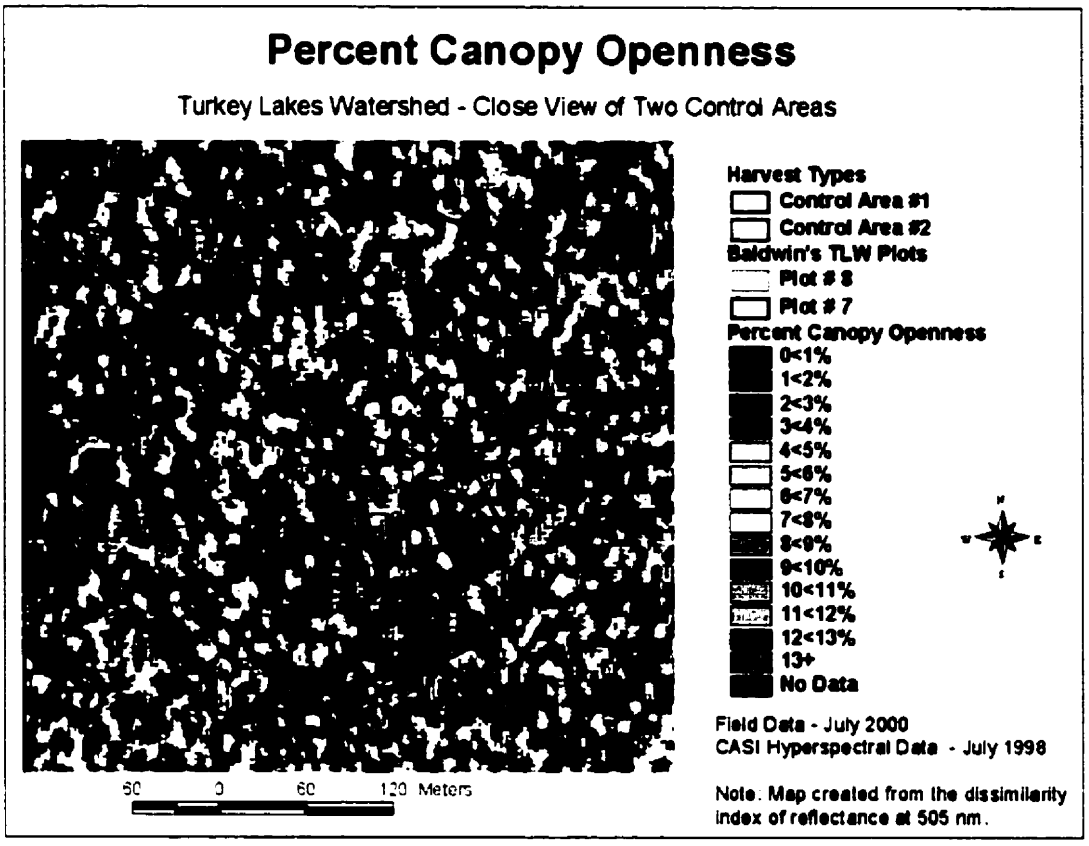

Figure 32: Percent Canopy Openness Map For Two Control Areas In TLW

Table 17: Percentage Area Derived From Modelled Percent Canopy Openness

Percentage Openness (%)	Area of Control Area #1 (%)	Area of Control Area #2 (%)
0 < 1	0.6	0.67
1 < 2	17.5	19.34
2 < 3	37.7	39.71
3<4	26.3	25.39
4<5	12.3	10.54
5<6	3.9	3.35
6<7	1.2	0.76
7<8	0.4	0.2
8<9	0.1	0.04
9<10	0	0.01
10 +	0	0

Table 18: Validation Statistics For Modelled Percent Canopy Openness

Statistics For The Control Areas	
Area of Control Area #1 (m^2)	39532
Percent Canopy Openness Calculated From Hemispherical Photos in Baldwin's Validation Plot #7 (%)	6.19
Mean Extracted Percent Canopy Openness in Validation Site (%)	3.5
Max Extracted Percent Canopy Openness in Validation Site (%)	4.9
Area of Control Area #2 (m^2)	57404
Percent Canopy Openness Calculated From Hemispherical Photos in Baldwin's Validation Plot #8 (%)	8.69
Mean Extracted Percent Canopy Openness in Validation Site (%)	4.7
Max Extracted Percent Canopy Openness in Validation Site (%)	7.0

4.8 Summary of Significant Results

1. The derivative images provide links to structural parameters that would not be detected otherwise, as subtle features on the reflectance curve are emphasized. This supports the notion that hyperspectral techniques may provide additional value to the assessment of forest structure.
2. Texture improves the correlations for most metrics.
3. The red edge and the REIP are common features of interest for several metrics.
4. Percent canopy openness calculated from hemispherical photos shows the greatest modelling potential. Correlations remained strong during validation.
5. Hemispherical photos are an efficient and unbiased method of obtaining canopy measurements.
6. Range values extracted by modelling the semivariograms vary according to wavelength and direction.
7. Use of extracted range values as inputs to texture filter dimensions improve the relationship between the spectral/spatial derivatives and the forest metrics.
8. Strong correlations exist between forest metrics and derivative images, particularly for the undisturbed forest health plots. Correlations decrease when using FH and ISD together.
9. Use of standard deviation to extract values from the remotely sensed image give the most robust relationships.
10. Narrow-band indices did not demonstrate strong relationships to forest structural parameters.

5.0 DISCUSSION

Satellites carrying hyperspectral sensors (e.g., Hyperion, MODIS) are now collecting data of the earth's surface. It is necessary to strive to understand the implications of interpreting detailed spectral data at coarser spatial scales and to develop approaches that will enable us to efficiently utilize such a large quantity of data without having to sacrifice any potentially beneficial trends in the data. Within the next ten years, the amount of data being collected by hyperspectral satellites could easily render current data warehousing facilities ineffective and cause current hyperspectral processing techniques to be unmanageable, particularly for studies at regional, national, or global spatial scales, unless more reliable and accurate automated approaches are developed.

Traditionally, feature extraction techniques are used to reduce the dataset to one or more wavelengths on which to perform analyses. This follows from the multispectral image-processing paradigm. Results from this research demonstrate that meaningful patterns of relationships and wavelengths would have been overlooked if feature extraction had been performed prior to the analysis. With this in mind, it became necessary to devise methods to examine the results in an efficient manner to come up with meaningful indices that could be validated elsewhere. Computer algorithms were developed and applied to identify wavelengths and indices that had high correlations with forest metrics. While it is possible that single channels (≈10 nm bandwidth) with strong correlations were overlooked, notable features on the spectral and derivative curves involving two or more sequential channels were investigated. Future work in this area could involve the development of algorithms to examine additional index/wavelength

permutations (of which there were over 500,000), as well as combinations of multiple wavelengths, for significant relationships.

5.1 Field Data

Design of the field sampling for this research required not only that the mensuration data be collected to capture natural variations occurring on the ground, but also that the scale of variation captured would be detectable on the hyperspectral image. Ideally, knowledge of spatial autocorrelation within the study area could be used to design an appropriate sampling scheme. Unfortunately, this is not usually feasible for remote sensing studies, as the imagery is collected during or after the field campaign and the relationships between the metrics being sampled and the remotely sensed data are unknown prior to the analysis. To address this, the sampling areas were designed to be large enough to include several image pixels, with the objective of capturing the scale of variation expected within the image data.

Semivariance analysis in this study illustrated that extracted range values varied according to wavelength, a result consistent with the work of others (e.g. Sampson, 2000; Treitz and Howarth, 2000; Sampson *et al.*, 2001; Treitz, 2001). This meant that a single optimal field sampling size for the entire hyperspectral dataset did not exist. To effectively capture variance within the field measures that would be applicable to the CASI reflectance data, the minimum sampling size would have to be larger than extracted range values presented in Appendix A.5. For most channels, the extracted range fell between 4-8 metres, suggesting that the "objects" embedded in the CASI data are tree crowns (i.e., the range values indicate a single tree). Sampling an 11.3 m radius (22.6 m

diameter) area would include a significant number of "objects" to capture the variance of the "objects" in the scene.

One of the issues arising from the field data collection was the accuracy of the sampling techniques. The standard measure of DBH was simple and consistent regardless of the time and conditions for sampling. However, estimates of other metrics (e.g., canopy shape, LAI, percent canopy openness) were complicated by weather (i.e., wind) and illumination conditions. Foresters from the Canadian Forest Service (CFS) and the Ontario Forest Research Institute (OFRI) were consulted to ensure the measurement techniques were consistent with standard forestry practices.

Use of the laser vertex (Haglof Vertex Hypsometer models 1 and 3) for measuring tree height proved to be a very efficient technique for sampling the large number of trees considered for this study. Tree height measurements were the most difficult parameter to measure in closed canopies, because of the challenge in identifying the apex of the crown from a location that satisfied the geometrical requirements of the vertex. In addition, occasional windy conditions caused the trees to sway, introducing variability to the measurements. To promote consistency with the technique throughout the season, the same two individuals used the instrument for the entire field season. It should be noted that previously existing tree height measurements for TLW were not collected with the same instrument. The accuracy of the technique was tested during the field season by measuring against objects of a known height, and after the field season by comparing the tree height measurements with previously collected tree heights in some of the same plots. Comparisons confirmed that average height measurements for the sampling sites were consistent between the two measuring techniques.

The measuring of canopy widths had the most room for inconsistency in the results, with at least two people needed to obtain the measurement. It required a judgment as to the longest axis of the tree crown. In closed canopy conditions, it was often difficult to separate one tree crown from the next. As a result, the technique often required a third person to render a judgment from a location further from the tree.

The hemispherical photos provided the most objective view of the canopy at any field site. They captured a permanent record of the canopy from below, intuitively suggesting a direct link to the CASI imagery taken from above. Success achieved with this sampling technique and the strong relationships between the percent canopy openness and CASI imagery, even for the validation sites at TLW, illustrated that hemispherical photos are very powerful tools for assessing forest canopy. Future work on the characterization of forest structure for remote sensing analysis should further explore this technique for estimating canopy conditions.

5.2 Spectral and Spatial Indices

5.2.1 Reflectance, Derivative, Red-Edge Inflection Point (REIP), and Integral Indices

Examination of the initial dataset (prior to geostatistical and texture processing) led to a number of observations that proved helpful in the interpretation of overall results. As mentioned, the spectral reflectance curve illustrated in Figure 10 is consistent with typical vegetation response (Lillesand and Kiefer, 1994). Some notable features observed on the curves include the green peak at approximately 558 nm, the beginning of the red edge at approximately 686 nm, the REIP in the vicinity of 724 nm, and the O_2

absorption feature at 762 nm (Adler-Golden *et al.*, 1999), which also marks the end of the red edge. The first- and second-derivative curves have considerably more variation, with subtle changes in the reflectance curve being much more pronounced (Figure 11). Variations within the red edge are particularly notable in the second-derivative image, which possesses a dip in the curve at 709 nm, as well as a bend in the curve at 739 nm. These features are in addition to the REIP at approximately 724 nm, which explains why results show multiple regions along the red edge that have strong correlations with forest metrics. The shift from positive to negative values in the first- and second-derivative curves also explains the positive and negative correlations illustrated in the correlation curves in Chapter 4 (Figures 26 to 30).

The REIP image (Figure 14) represents a different form of data presentation than the derivative or integral images. This image is a single channel, with each pixel containing the actual wavelength at which the REIP occurred. Variations in the image occur because of shifts in the location of the REIP, which are known to occur because of vegetative stress, species variation, and shadow variability due to canopy structure (Miller *et al.*, 1990; Sampson *et al.*, 1998; Treitz and Howarth, 1999). Conversely, the reflectance and calculus images convey the magnitude of response at specified wavelengths, where variations in the image illustrate changes in magnitude of response. Since one set of images (i.e., reflectance and calculus) contains variations in response at a specific wavelength and the other (i.e., REIP) contains variations in wavelengths, the two types of images are not directly comparable. For example, there are several instances where there are strong correlations with the metrics centreed on the REIP (of which the approximate location is known, $\approx$ 724 nm) (Table 9, Table 10), but comparatively low

correlations with the REIP image itself. Due to the spatial variations shown in the REIP image, there is no actual way to measure the magnitude of response at the REIP. Since the wavelengths around the REIP have strong correlations with the metrics, future work could examine modelling the magnitude of response in this area, rather than modelling the wavelength itself.

The integral image and the images derived from indices previously developed for physiological relationships do not have notable relationships with forest structural metrics. This is not a particularly surprising result, given that the various indices were developed around specific biochemical properties (pigment concentrations, etc.), with no consideration for spatial properties.

A comparison between the FH and ISD sites consistently demonstrated higher correlations for the FH sites, which were chosen for this analysis to serve as natural control sites. Compared to the ISD sites, the canopy of the FH sites are undamaged and the plots themselves are not managed for maple syrup production, meaning that the six FH sites have similar canopy conditions. This may be of particular importance when considering below canopy measures such as DBH. For site-specific studies, relationships between DBH and the crown have been established (Ter-Mikaelian and Lautenschlager, 2000). However, variability in the relationships due to site-specific factors (i.e., broken canopy for the ISD sites) is not currently understood (Ter-Mikaelian and Lautenschlager, 2000). Relationships between DBH and reflectance from a forest with a closed canopy (i.e., FH sites) would not be expected to hold for forests with major limbs broken and visible openings in the canopy in a somewhat random pattern (i.e., ISD sites) or systematic pattern (i.e., TLW).

Many of the highest correlations with metrics occur at wavelengths in the visible portion of the spectral curve (Table 5: crown closure; crown diameter; crown width; tree height; and LAI). This is important to note, since most hyperspectral techniques tend to focus on the red edge (i.e., physiological response). Results illustrate that the visible region, the red edge, and the NIR region all have a significant utility for multiple structural measures (e.g. percent canopy openness: visible and NIR (Table 11); tree height: visible and red edge (Table 9)). This information may prove useful in the future development of multi-band indices, which focus on more than one region of the EM spectrum.

5.2.2 Geostatistics and Texture Indices

Semivariogram analyses illustrate that extracted range values vary according to wavelength (Appendix A.5), a result that is supported by others (e.g., Sampson, 2000; Treitz and Howarth, 2000; Treitz, 2001). Although this has been reported for coarse spectral resolution remote sensing data, it has not been previously demonstrated for all wavelengths in a hyperspectral data cube. In this study, results reveal some cases of consecutive wavelengths where the extracted range values do not change. This suggests that the spectral scale required to detect spatial structure is coarser than the spectral resolution in these regions. Changes in the optimal range do not always occur at the same wavelengths when comparing the reflectance data to the first- and second-derivative data. This illustrates the benefits of calculating semivariance for each channel, rather than assuming a common range across all image channels.

An obvious question stemming from the semivariance analysis is whether or not this type of analysis actually improves the relationship between remote sensing data and forest metrics. Would improved relationships for some of the forest metrics (Table 6) have occurred by simply selecting arbitrary filter dimensions and calculating texture without consideration of semivariance? This question was addressed by comparing the relationships determined from pre-texture indices (Table 5) to those derived from first-order mean/variance texture. In the case of pre-texture analysis, image values were extracted based on the mean, standard deviation, and variance for the entire sampling area of the field site. First-order mean and variance texture calculations incorporate the optimal range. Any case where first-order mean and/or variance texture produce higher correlations than corresponding measures for pre-texture analysis illustrates improvement as a function of incorporating range estimates in the texture calculation. Several examples of first-order mean indices having stronger relationships than the pre-texture indices are presented in Tables 7 to 11. Results for number of trees, stem density, height to the crown base, tree height, crown closure, crown diameter, and crown width show improved correlations with texture features when the optimal range values are incorporated into texture filter definition. This result is significant, in that range extraction in this manner has not been reported in the literature.

A general examination of the texture indices reveals that texture improves the relationships to all forest metrics (with the exception of DBH), particularly when considering consecutive image channels. All forest metrics, with the exception of DBH, tree height, and height to the base of the crown, are derived from some measurement of the tree crown, suggesting a relationship between range and crown. As mentioned

earlier, range was calculated to be between 4 to 8 m for most image channels. Most measurements of crown width also fall within this range, further supporting the link between range and crown. Range is generally associated with the largest element in the scene (in this case along the transect), which corresponds to the tree crown for high spatial resolution imagery (Cohen and Spies, 1990; Treitz and Howarth, 2000; Sampson, 2000).

5.3 Spectral/Spatial Indices and Forest Structure

The ability to develop an index at a given calibration site and later transfer it to imagery at other sites with consistent accuracy was a key goal for this research. Part of the challenge when developing an index to monitor forest structure was the wide variety of canopy conditions that could be encountered in an image, particularly over such an expansive landmass as Ontario. Remote sensing of forest structure, particularly for sugar maple environments, is still relatively new with very few studies having been published where the work has been tested across multiple environments. Some work has been reported relating texture variables (contrast, entropy, angular second moment (ASM)) derived from multispectral video imaging to forest-decline indices extracted from airphoto interpretation, giving correlations of r=0.79 between contrast and the photo-decline index (Yuan *et al.*, 1991). This was expanded to a two-variable model (contrast and principle components) with r=0.85 between the texture and the photo-decline index (Yuan *et al.*, 1991). This work was then compared to ground-based modelling techniques employed by the Ontario Ministry of Environment (OME). Results showed that for most sites, there was a qualitative agreement with the OME model, which meant that both

techniques ordered the sites in a similar fashion in terms of the average sugar maple decline in the area (Yuan *et al.*, 1991). However, there was no quantitative comparison reported between the two methods.

Results from this research are mixed when trying to transfer indices from the calibration sites in southern Ontario to the validation sites at TLW. Even within the calibration sites, results vary when comparing indices developed from the FH sites alone to the ISD sites and to indices developed from the pooling of all of the sites. Deciduous forests are complex ecosystems, with many factors affecting crown architecture and hence spectral reflectance. Other research has attempted to solve this problem by first focusing on forest ecosystems that appear to be simpler to model or characterize. Success has been reported for extracting structural parameters from coniferous forests in flat terrain (Peddle *et al.*, 1999), but considerable difficulty still exists when moving from a coniferous environment to a mixed or deciduous environment (Peddle and Johnson, 2000). This work has shown some success in creating indices where relationships hold for some validation sites, particularly for control, shelterwood, and selected cut sites (e.g., metrics for percent canopy openness, LAI, number of trees, crown depth, crown diameter – Tables 12 to 16). Given the complex nature of the sugar maple ecosystem, the fact that these indices are transferable to TLW is encouraging.

Throughout the analysis, the results demonstrate that for several metrics the first- and second-derivative calculations improve correlations when compared to the reflectance data and texture features applied. This represents a significant result, because it shows that hyperspectral processing techniques contribute additional value to spatial processing for forest structure. The first- and second-derivative calculations accentuate

subtle variations that were insignificant in the original spectral reflectance curve. For example, although an examination of the spectral reflectance curve (Figure 7) does not reveal any notable features in the visible region other than the green peak associated with vegetation, the first- and second-derivative curves (Figure 11) emphasize several small but distinct features in the blue, green, and red wavelengths that are related to forest metrics (e.g., Table 8: 483-498 nm are related to elliptical crown closure). This is further emphasized by the results that demonstrate that most of the visible channel correlations occur in the derivative images (Table 5). These findings raise a few questions as to the nature of the derivative images themselves: 1) Are the subtle changes which are emphasized in the derivative curves a function of atmospheric noise or do they represent real features on the vegetation spectral curve? and 2) Why are the first- and second-derivatives related to the physical properties of the forest?

To address the first of these questions, a clear understanding of the derivative images is required. The information contained in each channel of the first-derivative image could be described as the amount of change in reflectance from one channel to the next, i.e. the slope of the reflectance curve. By definition, the sign of the data values changes from positive to negative at any point on the spectral reflectance curve where the slope changes. This would occur at notable features on the reflectance curve, including the green peak, the absorption well in the red region, the REIP, and the NIR shoulder, causing the correlation coefficient to change signs at these locations as well. This is exaggerated even further for the second-derivative image, which contains values describing the rate at which reflectance changes from one channel to another (i.e. acceleration on the curve – or the quantity of slope change from one channel to the next).

In this case, the change of sign from positive to negative is the result of the detailed shape of the curve, rather than an actual abrupt change in reflectance.

It becomes apparent from the above description that atmospheric noise, which may not be visibly apparent on the spectral reflectance curve, will be emphasized in the derivative curves. It is well known that even with imagery that has been processed to reflectance, like the CASI data used in this research, atmospheric absorption features are not perfectly modelled/removed (Miller, 2001). This is due in part to a lack of understanding of all of the effects of absorption and scattering in the atmosphere as well as to difficulties in modelling the spatial variation of these processes (Miller, 2001). A clear example of an atmospheric absorption effect that is plainly visible on the CASI spectral reflectance curve is the oxygen absorption feature at 762 nm (Figure 10). This feature has a dramatic effect on the first- and second-derivative curves (Figure 11), which, if its atmospheric origins were not known, could easily be confused for a real reflectance feature.

The confusion introduced by atmospheric features (and/or any other noise feature) was addressed in this research by: 1) the multi-pixel approach used to extract pixel values (i.e., within a 14 x 14 pixel study area, 196 pixels would be sampled to obtain a single value for the correlation analysis); and 2) the search for, and extraction of multiple consecutive wavelengths with high correlations. In this manner, features that may have resulted from atmospheric absorption and have high correlations with the forest metrics would not be pursued in the validation analysis unless they affected more than a 20 nm range of the spectral curve (i.e., each channel is approximately 10 nm wide). The chance of any of the final indices being related to forest metrics due to atmospheric artifacts was

further reduced by the validation analysis in TLW. These data were collected in a different year, with inherently different atmospheric conditions.

The question regarding the relationship between forest structural metrics and first- and second-derivative images should be expanded to include consideration of spatial pattern: 1) To what can the relationship between the first- and second-derivative images and the physical properties of the forest be attributed? 2) To what can the relationship between spatial pattern (texture) and the physical properties of the forest be attributed? and 3) How did these combine to produce the relationships found in this research?

Whether the research is addressing questions of forest structure or physiology, that fact remains that the sensor is only detecting one thing – the quantity of EM response that reaches it. To determine what causes relationships between the imagery and the forest metrics, it is necessary to trace the path of short-wave radiation from the sun as it travels through the atmosphere, where it is absorbed, transmitted, and reflected, to the canopy surface where it undergoes the same processes. Incident short-wave radiation reaches the forest canopy (i.e., either direct short-wave radiation from the sun or diffuse short-wave radiation from the sky) and interacts with leaves at the cellular level. Of this, a portion is reflected towards the sensor. Further, energy is transmitted through the canopy to interact with the understory and the ground surface. Portions of this energy will also be reflected towards the sensor. The interaction between EM energy and the leaf has been studied at both the laboratory and canopy scales. Relationships between the first and second derivatives of the spectral curve and cellular biochemical processes have been established in the literature. Many of the existing hyperspectral indices developed for estimating physiological response are summarized in Appendix A.1. By relating the

imagery to forest structure, this research is assessing the spatial distribution and pattern of these cellular processes as well as the pattern of shadow and gaps in the canopy.

To gain an understanding of the structural relationships found in this research and how they can be related back to our understanding of EM interaction with the forest canopy, it is necessary to consider what is actually occurring in the structure of the forest canopy in relation to the various metrics. The variable that was most easily modelled was percent canopy openness. Let us first consider this metric and the relationships to dissimilarity and angular second moment. The strongest relationships were found with these texture features and percent canopy openness in the blue, red, and NIR (>800 nm) wavelengths.

Low values of percent canopy openness (or high values of crown closure) imply a closed canopy, with very few gaps or breaks. From a synoptic vantage point, these areas would appear to be densely vegetated, with some "shallow" shadow features spread rather evenly throughout the canopy as a result of the orientation of the leaves, or as the result of some trees being taller than others, but with very few deep shadow areas that might be associated with gaps in the canopy. Variability (and dissimilarity) would be highest in the NIR region of the EM spectrum, as the amount of reflectance from vegetation is highest in this region. The blue and red regions would appear relatively dark and uniform under closed canopy conditions (a function of chlorophyll absorption). As percent canopy openness increases, more deep shadow areas will occur, increasing the variability (and dissimilarity) of reflectance values likely to occur in the blue and red regions. This effect would also be evident but less pronounced in the NIR region, because multiple scattering in the canopy causes more variability in the amount of

reflectance in the NIR. This explains why percent canopy openness is related to the dissimilarity texture features of reflectance in the visible region, and to the first-derivative image in the NIR (i.e., the first-derivative image emphasizes the subtle differences in the texture features) (Tables 6, 11, and 12). With these physical factors in mind, the dissimilarity texture features would be lowest in closed canopy conditions at each wavelength. However the lowest dissimilarity values in the NIR would be higher than the lowest values in the blue and red regions. As gaps are introduced to the canopy, dissimilarity in all regions of the spectrum would increase, but the most obvious change would occur in the visible wavelengths. Therefore, one would expect that as percent canopy openness increases, the dissimilarity values would increase, resulting in a positive correlation (Figure 30). Note that the opposite is true for crown closure, producing a negative correlation between range and crown closure (Figure 27).

ASM can be considered the opposite of entropy (Hall-Beyer, 2000), and as such can be considered a measure of the presence of distinct structure or organization of patterns within the image (Yuan *et al.*, 1991). Structure or pattern would be expected to increase as gaps and shadows are introduced into the canopy, resulting in a positive correlation between ASM and percent canopy openness. With this description of ASM, the relationships would be expected to weaken in closed canopy or clear-cut conditions, as was shown to be the case in the validation analysis (Table 12). As was the case with dissimilarity, relationships with the percent canopy openness would be most evident in the visible regions, since the multiple scattering effects in the NIR would introduce some confusion to this calculation (Tables 11 and 12).

LAI and crown diameter were found to have relationships with dissimilarity and homogeneity respectively on the green peak and the red edge, which are wavelengths known to be related to vegetation type, photosynthetic capacity, and efficiency of radiation use (Gamon *et al.*, 1995; Zarco-Tejada and Miller, 1999). Dissimilarity has negative correlations with LAI, suggesting that as variability within the filter increases (i.e. as more shadows and gaps are introduced), values for LAI decrease. In other words, as gaps are introduced, a smaller fraction of the pixel is composed of leaf area. Homogeneity can be described as essentially the opposite to dissimilarity (areas with higher variance have lower values of homogeneity), which explains the positive correlations found with crown diameter (Tables 8 and 14). In this case, as the size of the crown increases and gaps are reduced within the filter, homogeneity increases.

First- and second-order mean texture features are negatively correlated with the number of trees. This can be explained by the shadow and illumination effects caused by the edge of individual crowns. More individual crowns cause increased edges between them, introducing more shadowed pixels and bi-directional reflection effects, which would lower the mean reflectance. This idea is supported by conclusions reported by Olthof and King (1998) who suggested that higher texture values (in their case "contrast") occur along edges where two fractions meet, with low values occurring in larger dark or bright areas. This would be expected to happen at all wavelengths, however the variability in reflectance in the NIR would decrease this effect somewhat. Here again, the first derivative of the mean texture feature accentuate the subtle changes in this region, allowing for a stronger correlation than for the reflectance image (Table 10).

Finally, entropy for the second derivative of the blue region is related to crown depth (Tables 9 and 16). Entropy is a measure of uncertainty within the filter and can be thought of as a measure of the lack of structure or pattern (Yuan *et al.*, 1991). The value will be low if the image is relatively smooth, and high if there is more of a pattern. The results indicate that as the pattern increases, crown depth increases as well. This finding is supported by field observations, which note that in the broken canopy conditions of the ISD plots, young trees have grown toward any gap with available sunlight (this would have occurred in the two-year span between the ice storm and field work). Because there is a lot of sunlight reaching lower levels of the forest, many of these trees have small branches all the way down the trunk, making identification of the base of the crown very difficult. This contrasts with the old growth in the TLW, where tree crowns are very distinct, with few branches lower than the main canopy.

All of the relationships described above are strongly influenced by the effects of shadow and variations in illumination. The ability to understand and characterize shadow and its patterns within the image is critical to the extraction of structural information about the forest. This need has been recognized in current research, and attempts to relate shadow to structure have been reported (Yuan *et al.*, 1991). Attempts to extract the shadow component of a pixel have also been reported (Peddle *et al.*, 1999), but the complexity of sugar maple stands has thus far limited the success in this area.

6.0 CONCLUSIONS & RECOMMENDATIONS

Perhaps more significant than the indices that were developed in this research is the notion that the techniques used to develop them have proven to provide beneficial information about the pattern of relationships along the spectral curve. The integration of spatial and hyperspectral techniques do improve relationships with structural measures, which suggests that further research in this area is warranted. Results in this research demonstrate that meaningful relationships along the spectral and derivative curves would have been entirely missed if feature extraction had been performed prior to the analysis, because features on the spectral, and hence the derivative curves, would not have been captured. By accentuating correlation patterns on the spectral and derivative curves that would not have been detectable using multispectral images, it has been demonstrated in this work that hyperspectral imagery has unique and valuable information to add to remote sensing of forest structure.

In many cases, the first- and second-derivative images improve correlations between the hyperspectral data and forest structure metrics (e.g., Table 5). This is due to the fact that subtle features on the spectral reflectance curve are emphasized on the first- and second-derivative curves. This result illustrates the utility of applying hyperspectral techniques to forest structure research. Further supporting this idea are strong correlations with measures of the crown dimensions and the REIP (e.g., Figure 27), a feature known to be related to physiological parameters (Zarco-Tejada *et al.*, 1999).

The visible, red-edge, and NIR regions of the EM spectrum each contain features that are correlated with forest structure. Several forest structural metrics have strong correlations in multiple regions of the spectrum, illustrating a potential for multiband

indices. For example, percent canopy openness (Tables 11 and 12) is highly correlated to texture features in the blue, red, and NIR regions of the EM spectrum. This result demonstrates the importance of investigating all regions of the EM spectrum detected by the hyperspectral sensors, rather than focusing on the red edge as tends to occur for physiological indices (Appendix A.1.4 and A.1.5).

Incorporating geostatistical (i.e., semivariance) results with texture analysis by defining the filter dimensions with estimated range parameter improves the correlation with the texture features and forest structure measures (e.g., for number of trees, stem density, height to the crown base, tree height, crown closure, crown diameter, and crown width). Estimated range values vary according to wavelength and appear to be linked to individual tree crowns (Appendix A.5). This supports the results of previous work (e.g., Sampson, 2000; Treitz and Howarth, 2000; Treitz, 2001).

Texture features improve correlations between the hyperspectral data and all forest structure metrics (except DBH). Most prevalent in the results are: homogeneity; dissimilarity; and mean texture features. Dissimilarity texture features are negatively correlated with estimates of LAI and positively correlated to percent canopy openness (Table 11), suggesting a link with shadow fraction (Yuan *et al.*, 1991; Peddle *et al.*, 1999). Mean texture features are negatively correlated to the number of trees within the plots (Table 15), which is attributed to shadow and illumination effects along the edge of the tree crowns (Olthof and King, 1998). Finally, homogeneity is positively related to crown diameter (Table 14), indicating that as crown size increases and gaps in the canopy are reduced, the image becomes smoother (i.e., more homogenous) within the filter.

To this point, emphasis has been placed on developing indices that are transferable across sugar maple environments across Ontario. However, results indicate that this may be too broad a study area to realistically expect one index to perform well under all conditions. However, when considering the expansive area within south-eastern Ontario over which the indices were developed, predictive indices could potentially provide valuable information for this area. This would first require additional validation sites, to assess the accuracy of the prediction maps. This could prove to be particularly interesting when considering the temporal changes occurring in the canopy affected by the ice storm as the health of the damaged canopies improve.

Although the results from this work show promise, considerable study needs to be undertaken before hyperspectral remote sensing can extract forest structure in a sufficiently practical and reliable way to be useful for forest managers or government reporting agencies. Clearly, use of this data is still very much in the research phase, with limited understanding of how forest ecosystems are characterized or measured by hyperspectral sensors operating at a given spatial resolution. With this in mind, the following recommendations have been developed based on the results and issues encountered within this study.

1.) There is an immediate need to assess the impact of moving to a coarser spatial scale, while still maintaining the fine spectral resolution. A multi-scaled analysis needs to be undertaken both for physiological and structural parameters to gain a better understanding of the scaling phenomenon across landscapes with respect to canopy reflectance.

2.) Greater effort is required to determine the most effective sampling strategy for various structural parameters, particularly for "upscaling" to coarser resolutions. The objective use of field data should also be considered, since linking field data to a remotely sensed image requires different considerations and sampling criteria than currently used by forest managers to obtain stand-level information. This again will require an analysis of the effect of scale on the representation of forest parameters.

   a. This work should be completed with careful consideration of current and anticipated forest management objectives. If hyperspectral satellite technology is going to eventually prove useful to forest managers and government reporting agencies, it must be suitable for addressing problems they are currently considering. An understanding of how variations in structural parameters are linked to ecosystem health at various spatial scales is required. Keeping in mind that remote sensing does not provide causal information, it is necessary to determine what information needs to be extracted at the satellite scale and how that information can actually be used by foresters once it has been demonstrated to be accurate and reliable.

   b. Given the success with hemispherical photography in this study, more work should be completed to assess effective methods of relating above and below canopy images to canopy structure. Hemispherical photos may

prove to be an effective and objective approach to determining canopy shape from the ground.

3.) As knowledge of the spatial and spectral processes occurring at the canopy improves, more efforts should be directed towards automating the computer processing and storage techniques. This will assist in reducing the size of the data sets to be more manageable and eliminate the need for repetitive manual calculations that may introduce error and in general make the use of this technology unattractive to forest managers.

4.) Spectral unmixing, a method to determine the shadow component of the imagery, is a spatial technique that was not incorporated into this research. Work should be completed to improve the effectiveness of spectral unmixing in a sugar maple environment so that the success of the technique can be compared to texture/geostatistical results. Once this has been completed, the potential of combining the two approaches to extract shadow component could be considered. This has significant application to analyzing hyperspectral data at satellite scales.

5.) The REIP has been shown to be a feature of interest for both physiological and structural investigations. A more detailed investigation of REIP spatial variations, particularly when moving across scales should be undertaken. Underlying ecosystem processes that are affecting this parameter need also to be investigated at various scales.

6.) Validation results for percent canopy openness showed that multiple texture features had relationships with calibration and one or more validation sites, indicating that different texture features are more effective than others for characterizing different silviculture treatments. To attempt to characterize a greater range of silviculture treatments in the texture models, a multi-variable relationship should be explored.

7.) Further investigation is required into determining optimal distance and direction parameters for generating the GLCM. The need for this was illustrated in Figures 22 to 25 for ASM and entropy, which were not optimized at this wavelength (739 nm), most likely due to the variability in the NIR (i.e., multiple scattering) as compared to the visible regions. This made the adjacent pixel specified by the distance and direction parameters an inappropriate choice for ASM and entropy in the NIR. The utility of the range and anisotropic information derived from semivariance analysis for these parameters should be determined.

8.) Results indicate that reporting optimal wavelengths for structural parameters based on the highest determined correlation between wavelengths and metrics can be very misleading, because it ignores correlation patterns across wavelengths. Efforts should be made to consider consecutive channels with high correlations when reporting results.

The potential to extract structural information from hyperspectral data is encouraging for the future analysis of satellite hyperspectral data. This potential suggests that the applications of hyperspectral satellites for forest research are more widespread than is commonly considered. If physiological and structural information can both be extracted from the same data, a significant step forward in providing cost effective tools for resource managers and government reporting agencies to repetitively monitor forest ecosystems over large areas can be taken.

REFERENCES

Aber, J.D. and M.E. Martin, 1995. "High Spectral Remote Sensing of Canopy Chemistry," *Summaries of the Fifth Annual JPL Airborne Earth Science Workshop*, NASA Jet Propulsion Laboratory publication 95-1, January 23-26, 1995, Vol. 1, pp. 1-4.

Adler-Golden, S.M., M.W. Matthewa, L.S. Bernsteina, R.Y. Levinea, A. Berka, S.C. Richtsmeiera, P.K. Acharyaa, G.P. Andersonb, G. Feldeb, J. Gardnerb, M. Hokeb, L.S. Jeongb, B. Pukallb, J. Mellob, A. Ratkowskib, and H.-H. Burkec, 1999. "Atmospheric Correction for Short-wave Spectral Imagery Based on MODTRAN4," *Image Spectrometery V, SPIE Proceedings*, July, 1999, Vol. 3753.

Arbia, G., 1989. *Spatial Data Configuration in Statistical Analysis of Regional Economic and Related Problems.* Kluwer Academic Publishers.

Badhwar, G.D., R.B. MacDonald, F.G. Hall, J.G. Carnes, 1986. "Spectral Characterization of Biophysical Characteristics in a Boreal Forest: Relationships Between Thematic Mapper Band Reflectance and Leaf Area Index for Aspen," *IEEE Transactions on Geoscience and Remote Sensing*, Vol. GE-24, No. 3, pp. 322-326.

Baldwin, K, 2000. Personal Communication, Canadian Forest Service, Saulte Ste. Marie, ON.

Baret, F., G. Guyot, and D. Major, 1989. "TSAVI: A vegetation index which minimizes soil brightness effects on LAI or APAR estimation," *Proceedings of the 12th*

Canadian Symposium on Remote Sensing and International Geoscience and Remote Sensing Symposium 1989, Vancouver Canada, July 10-14, 1989, pp. 1355-1358.

Baret, F. and G. Guyot, 1991. "Potentials and limits of vegetation indices for LAI and APAR assessment," *Remote Sensing of Environment*, Vol. 35, pp. 53-70.

Belanger, M.J., J.R.Miller, and M.G. Boyer, 1995. "Comparative Relationships Between Some Red Edge Parameters and Seasonal Leaf Chlorophyll Concentrations," *Canadian Journal of Remote Sensing*, Vol. 21, No. 1, pp. 16-21.

Blackburn, G.A., 1998. "Quantifying chlorophylls and carotenoids from leaf to canopy scales: an evaluation of some hyperspectral approaches," *Remote Sensing of Environment*, Vol. 66, pp. 273-285.

Brack, C.L., 1997. "Measuring Stand Basal Area," *Technical Note: IFA Newsletter*, Vol. 38, No. 5, pp. 16 – 17.

Bowers, W.W., S.E. Franklin, J. Hudak, and G.J. McDermid, 1994. "Forest Structural Damage Analysis Using Image Semivariance," *Canadian Journal of Remote Sensing*, Vol. 20, No. 1, pp. 28-36.

Butson, C.R. and D.J. King, 1999. "Semivariance Analysis of Forest Structure and Remote Sensing Data to Determine and Optimal Sample Plot Size," *Proceedings of the Fourth International Airborne Remote Sensing Conference and Exhibition*, Ottawa, Ontario, Canada, June 21-24, Vol. 2, pp. 155-162.

Canadian Council of Forest Ministers, 1998. "Sustainable Forest: A Canadian Commitment," *National Forest Strategy On-Line Publication*, http://nfsc.forest.ca/strategy4.html.

Carter, G.A. 1994. "Ratios of leaf reflectances in narrow wavebands as indicators of plant stress," *International Journal of Remote Sensing*, Vol. 15, No. 3, pp. 697-703.

Carter, G.A, 1998. "Reflectance Wavebands and Indices for Remote Estimation of Photosynthesis and Stomatal Conductance in Pine Canopies," *Remote Sensing of Environment*, Vol. 63, No. 1,pp. 61-72.

Chen, J.M. 1996. "Evaluation of Vegetation Indices and a Modified simple Ratio For Boreal Applications," *Canadian Journal of Remote Sensing*, Vol. 22, No. 3, pp. 229-242.

Chen, J.M. and J. Chilar, 1996. "Retrieving Leaf Area Index of Boreal Conifer Forests Using Landsat TM Images," *Remote Sensing of Environment*, Vol. 55, pp.153-162.

Clark, R. N., 1999. *Spectroscopy and Principles of Spectroscopy. Manual of Remote Sensing*. John Wiley and Sons, Inc.

Cohen, W.B. and T.A. Spies, 1990. "Semivariograms of Digital Imagery for Analysis of Conifer Canopy Structure," *Remote Sensing of Environment*, Vol. 34, pp. 167-178.

Crippen, R.E., 1990. "Calculating the Vegetation Index Faster," *Remote Sensing of Environment*, Vol. 34, pp. 71-73.

Crist, E.P, and R.C. Cicone, 1984. "Application of the tasseled cap concept to simulated thematic mapper data," *Photogrammetric Engineering and Remote Sensing*, Vol. 50, pp. 343-352.

Curran, P.J., 1988. "The Semivariogram in Remote Sensing: An Introduction", *Remote Sensing of Environment*, Vol. 24, pp. 493-507.

Curran, P.J. and P.M. Atkinson, 1999. "Issues of scale and optimal pixel size," *Spatial Statistics For Remote Sensing*, edited by A. Stein, F. Van Der Meer, and B. Gorte Dordrecht: Kluwar Academic Pulblishers, pp. 115-133.

Davison, D., S. Achal, S. Mah, R. Gauvin, M. Kerr, A. Tam, and S. Preiss, 1999. "Determination of Tree Species and Tree Stem Densities in Northern Ontario Forests Using Airborne CASI Data," *Proceedings of the Fourth International Airborne Remote Sensing Conference and Exhibition*, Ottawa, ON, June 21-24, 1999, Vol. 2, pp. 187–196.

Dawson, T. P., 1998. "Estimating the Foliar Biochemical Content of Forest Canopies Using Physical Models and Aviris Spectra," *Proceedings of the First International Conference on Geospatial Information in Agriculture and Forestry*, Lake Buena Vista, Fl, June 1-3, 1998, Vol. 1, pp. 433–440.

Deering, D. W., J. W. Rouse, R. H. Haas, and J. A. Schell, 1975. "Measuring forage production of grazing units from Landsat MSS data," *Proceedings, 10th International Symposium on Remote Sensing of Environment*, Vol. 2, pp. 1169-1178.

DeWulf, R.R., Gossens, R.E., DeRoover, B.P., and F.C. Borry, 1990. "Extraction of forest stand parameters from panchromatic and multispectral SPOT-1 data," *International Journal of Remote Sensing*, Vol. 11, pp. 1571-1588.

Elvidge, C.D. and Z. Chen, 1995. "Comparison of Broad-Band and Narrow-Band Red and Near-Infrared Vegetation Indices," *Remote Sensing of Environment*, Vol. 54, pp. 38-48.

ENVI, 2000. *ENVI Tutorials*, ENVI Version 3.4, September, 2000 Edition, Research Systems Inc., Colorado. 590 pp.

Estes, J.E., 1997. "Lecture 1: The History of Aerial Photography," *The Remote Sensing Core Curriculum*, An ASPRS Initiative For Space Age International Education, Vol. 1, http://umbc7.umbc.edu/~tbenja1/santabar/vol1/lec1/1lecture.html

Farina, A., 1998. *Principles and Methods in Landscape Ecology*, Chapman & Hall Ltd., New York.

Fleming, R.A., D.B. Lyons, and J.N. Candau, 1999. "Spatial Transmutation and its Consequences in Spatially Upscaling Models of Spruce Budworm Population Dynamics," *Canadian Journal of Remote Sensing*, Vol. 25, No. 4, pp. 388-402.

Frazer, G.W., Canham, C. D., and Lertzman, K. P. 1999. *Gap Light Analyzer (GLA). Version 2.0: Imaging software to extract canopy structure and gap light transmission indices from true-color fisheye photographs, users manual and program documentation*,Simon Fraser University, Burnaby, British Columbia, and the Institute of Ecosystem Studies, Millbrook, New York.

Friedl, M.A., F.W. Davis, J. Michaelsen, and M.A. Moritz, 1995. "Scaling and Uncertainty in the Relationship between the NDVI and Land Surface Biophysical Variables: An Analysis Using a Scene Simulation Model and Data from FIFE," *Remote Sensing of Environment*, Vol. 54, pp. 233-246.

Gamon, J.A., D.A. Roberts, and R.O. Green, 1995. "Evaluation of the Photochemical Reflectance Index in AVIRIS Imagery" *Summaries of the Fifth Annual JPL Airborne Earth Science Workshop*, NASA Jet Propulsion Laboratory publication 95-1, January 23-26, 1995, Vol. 1, pp. 121-124.

Gitelson, A.A. and M.N. Merzlyak, 1997. "Remote estimation of chlorophyll content in higher plant leaves," *International Journal of Remote Sensing*, Vol. 18, No. 12, pp. 2691-2697.

Goetz, A.F.H, G. Vane, J.E. Solomon, and B.N. Rock, 1985. *Imaging spectrometry for earth remote sensing*. Science, Vol. 228, pp. 1147-1153.

Gong, P., Marceau, D.J., and P.J. Howarth, 1992. "A Comparison of Spatial Feature Extraction Algorithms for Land-Use Classification with SPOT HRV Data," *Remote Sensing of Environment*, Vol. 40, pp. 137-151.

Govaertz, Y.M., M.M. Verstraete, B. Pinty, and N. Gobron, 1999. "Designing optimal spectral indices: a feasibility and proof of concept study," *International Journal of Remote Sensing*, Vol. 20, No. 9, pp.1853-1873.

Goward, S. N., 1989. "Satellite bioclimatology." *Journal of Climate*, Vol. 7, No. 2, pp. 710-720.

Goward, S.N., and K.F. Huemmrich, 1992. "Vegetation canopy PAR absorptance and the normalized difference vegetation index: an assessment using the SAIL model," *Remote Sensing of Environment*, Vol. 39, pp. 119-140.

Gray, L., J. Freemantle, P. Shepherd, J. Miller, J. Harron, and C. Hersom, 1997. "Characterization and Calibration of the CASI Airborne Imaging Spectrometer

for BOREAS," *Canadian Journal of Remote Sensing*, Vol. 23, No. 2, pp. 188-195.

Grossman, Y.L., E.W. Sanderson, and S.L. Ustin, 1994. "Relationships Between Canopy Chemistry and Reflectance for Plant Species from Jasper Ridge Biological Preserve, California," *Proceedings of the International Geoscience and Remotes Sensing Symposium IGARSS '94*, California Institute of Technology, August 8-12, 1994, 4 pp.

Hall-Beyer, M., 2000. "GLCM Texture: A Tutorial, Version 2.3," *Remote Sensing Core Curriculum*, Volume 3, Introductory Digital Image Processing, On-Line Publication, http://www.cla.sc.edu/geog/rslab/rsccnew/

Hansen, M.J., S.E. Franklin, C. Woudsma, and M. Peterson, 2001. "Forest Structure Classificatino in the North Columbia Mountains Using the Landsat TM Tasseled Cap Wetness Component", *Canadian Journal of Remote Sensing*, Vol. 27, No. 1, pp. 21-32.

Hay, G.J., K.O. Niemann, and G.F. McLean, 1996. "An Object-Specific Image-Texture Analysis of H-Resolution Forest Imagery," *Remote Sensing of Environment*, Vol. 55, pp. 108-122.

Hershey, R. R., W. H. McWilliams, and G.C. Reese, 1998. "Utilizing the Spatial Structure Available: Creating Maps of Forest Attributes From Forest Inventory Data," *Proceedings of the First International Conference on Geospatial Information in Agriculture and Forestry*, Lake Buena Vista, Fl, June 1-3, 1998, Vol. 1, pp. 64-71.

Hochheim, K.P. and D.G. Barber, 1998. "Spring Wheat Yield Estimation for Western Canada Using NOAA NDVI Data," *Canadian Journal of Remote Sensing*, Vol. 24, No.1, pp. 17-27.

Hoffbeck, J.P. and D.A. Landgrebe, 1996. "Classification of Remote Sensing Images Having High Spectral Resolution," *Remote Sensing of Environment*, Vol. 15, pp. 119-126.

Huete, A.R. and C.J. Tucker, 1991. "Investigation of soil influences in AVHRR red and near-infrared vegetation index imagery," *International Journal of Remote Sensing*, Vol. 12, No.6, pp.1223-1242.

Huete, A.R., H.Q. Liu, K. Batchily, and W. van Leeuwen, 1997. "A comparison of vegetation indices over a global set of TM images for EOS-MODIS," *Remote Sensing of Environment*, Vol. 59, No. 3, pp. 440-451.

Hypannen, H., 1996. "Spatial autocorrelation and optimal spatial resolution of optical remote sensing data in boreal forest environment", *International Journal of Remote Sensing*, Vol. 17, No. 17, pp. 3441-3452.

Jackson, R.D., P.N. Slater, and P.J. Pinter, 1983. "Discrimination of growth and water stress in wheat by various vegetation indices through clear and turbid atmospheres," *Remote Sensing of the Environment*, Vol. 15, pp.187-208.

Jensen, R.J., 1996. *Introductory Digital Image Processing A Remote Sensing Perspective, 2nd Edition*, Prentice Hall, New Jersey, 316 pp.

Jelinski, D.E. and J. Wu, 1996. "The modifiable areal unit problem and implications for landscape ecology", *Landscape Ecology*, Vol. 11, No. 3, pp. 129-140.

Jongman R.H.G., C.J.F. Ter Braak, and O.F.R. Van Tongeren, 1995. *Data Analysis in Community and Landscape Ecology*. Cambridge University Press, New York.

Jordon, C.F., 1969. "Derivation of leaf area index from quality of light on the forest floor," *Ecology*, Vol. 50, pp. 663-666.

Kaufman, Y.J. and D. Tanré, 1992. "Atmospherically Resistant Vegetation Index (ARVI) for EOS-MODIS," *IEEEE Transactions on Geoscience and Remote Sensing*, Vol. 30, No. 2, pp. 261-270.

Kauth, R.J. and G.S. Thomas, 1976. "The tasseled cap – A graphic description of the spectral-temporal development of agricultural crops as seen by Landsat," *Proceedings of the Symposium on Machine Processing of Remotely Sensed Data*, Purdue University, West Layfayette, Indiana, pp. 41-51.

King, D.J., 1997. "Low Cost Multispectral Digital Camera Imaging for Forest Modelling and Topographic Mapping," *Proceedings of the Third International Airborne Remote Sensing Conference and Exhibition*, Copenhagen, Denmark, July 7-10, Vol. 2, pp. 397-404.

Landgrebe, D, 1998. *First Annual Progress Report NASA Grant NAGW5-3975 for the period 2/1/97 to 1/31/98*. School of Electrical and Computer Engineering, Purdue University.

Lambin, E.F. and D. Ehrlich, 1995. "Combining vegetation indices and surface temperature for land-cover mapping at broad spatial scales," *International Journal of Remote Sensing*, Vol. 16, No. 3, pp. 573-579.

Larsen, M., 1999. "Individual Tree Top Position Estimation by Template Voting," *Proceedings of the Fourth International Airborne Remote Sensing Conference*

and Exhibition/21st Canadian Symposium on Remote Sensing, Ottawa, Ontario, Canada, 21-24 June 1999.

Lautenschlager, R.A., 2000. "Can intensive silviculture contribute to sustainable forest management in northern ecosystems?" *The Forestry Chronicle*, Vol. 76, No. 2, pp. 283-295.

Lautenschlager, R.A. and C. Nielsen, 1999. "Ontario's Forest Science Efforts Following the 1998 Ice Storm," *The Forestry Chronicle*, Vol. 75, No. 4, pp. 633-641.

Legendre, P. and M.J. Fortin, 1989. "Spatial Pattern and Ecological Analysis", *Vegetatio*, Vol. 80, pp. 107-138.

Lévesque, J. and D.J. King, 1999. "Airborne Digital Camera Image Semivariance for Evaluation of Forest Structural Damage at an Acid Mine Site," *Remote Sensing of Environment*, Vol. 68, pp. 112-124.

Lillesand, T.M. and R.W. Kiefer, 1994. *Remote Sensing and Image Interpretation, Third Edition*, John Wiley & Sons, Inc., Toronto, 750 pp.

Lichtenhaler, H.K., A.A. Gitelson, A.A., and M. Lang, 1996a. "Non-destructive determination of chlorophyll content of leaves of a green and aurea mutant of tobacco by reflectance measurements," *Journal of Plant Physiology*, Vol. 148, pp. 483-493.

Lichtenhaler, H.K., M. Lang, M. Sowinska, F. Heisel, and J.A. Mieh, 1996b. "Detection of vegetation stress via a new high resolution fluorescence imaging system," *Journal of Plant Physiology*, Vol. 148, pp. 599-612.

Liu, H.Q. and A. Huete, 1995. "A Feedback Based Modification of the NDVI to Minimize Canopy Background and Atmospheric Noise," *IEEE Transactions on Geoscience and Remote Sensing*, Vol. 33, No. 2, pp. 457-465.

Major, D.J., F. Baret, and G. Guyot, 1990. "A ratio vegetation index adjusted for soil brightness," *International Journal of Remote Sensing*, Vol. 11, No. 5, pp. 727-740.

Marceau, D.J., 1999. "The Scale Issue in the Social and Natural Sciences", *Canadian Journal of Remote Sensing*, Vol. 25, No. 4, pp. 347-356.

Merton, R.N. and L.E. Harvey, 1997. "Analysis of seasonal changes in Jasper Ridge vegetation biochemistry and biophysiology using multi-temporal hyperspectral data," *Proceedings of the ASPRS Conference*, Seattle, Washington, USA. 6-10 April 1997.

Merton, R., 1998. "Monitoring Community Hysteresis Using Spectral Shift Analysis and the Red-edge Vegetation Stress Index," *Proceedings of the Seventh Annual JPL Airborne Earth Science Workshop*, NASA, Jet Propulsion Laboratory, Pasadena, California, January 12-16, 1998.

Miller, J.R., 2001, Personal Communication, Department of Physics, York University.

Miller, J.R., E.W. Hare, and J. Wu, 1990. "Quantitative Characterization of the Vegetation Red Edge Reflectance. I: An Inverted-Gaussian Reflectance Model," *International Journal of Remote Sensing*, Vol. 11, No. 10, pp. 1755-1773.

Mohammed, G.H., P.H. Sampson, S.J. Colombo, T.L. Noland, and J.R. Miller, 1997. *Bioindicators of Forest Sustainability: Development of a Forest Condition Rating*

System for Ontario, Forest Research Information Paper No. 137, Queen's Printer for Ontario, 22 pp.

Novo, E., M. Gastil, and J. Melack, 1995. "An Algorithm For Chlorophyll Using First Difference Transformations of AVIRIS Reflectance Spectra," *Summaries of the Fifth Annual JPL Airborne Earth Science Workshop*, NASA Jet Propulsion Laboratory publication 95-1, January 23-26, 1995, Vol. 1, pp. 121-124.

Natural Resources Canada, 1998. "Turkey Lakes Tolerant Hardwoods Ecosystem Research Project (TLHERP)," Unpublished Project Description, Canadian Forest Service, Sault Ste. Marie, ON, *http://www.glfc.forestry.ca/index-en/research-e/forest_ecology-e/turkeylakes-e.html*.

Olthof, I., and D. J. King, 1998. "Determination of Soil Property and Forest Structure Relations With Airborne Digital Camera Images Spectral and Spatial Information," *Proceedings of the 19th Canadian Symposium on Remote Sensing*, Ottawa, ON, May, 1997, pp. 103-106.

Ontario Ministry of Natural Resources (OMNR), 1999. *Ontario's Living Legacy land use strategy*, Queen's Printer for Ontario, Toronto, ON, 136 pp.

Openshaw, S., 1984. *The Modifiable Areal Unit Problem.* Concepts and Techniques in Modern Geography (CATMOG), no. 38. GeoBooks, Norwich, England.

Openshaw, S. and P.J. Taylor, 1979. "A million or so correlation coefficiecnts: three experiments on the modifiable areal unit problem," In *Statistical Applications in the Spatial Sciences*, pp 127-144. Edited by N. Wrigley, Pion, London.

Openshaw, S. and P.J. Taylor, 1981. "The Modifieable Areal Unit Problem," In *Quantitative Geography*: A Britist View, pp 60-69. Edited by N. Wrigley and R Bennett. Routledge and Kegan Paul, London.

Pannatier, Y., 1996. *Statistics and Computing VARIOWIN Software for Spatial Data Analysis in 2D*. Springer-Verlag New York Inc., New York.

PCI, 1998. *Using PCI Software, Volume 1, Version 6.3*, PCI Geomatics, Richmond Hill, ON, 528 pp.

Peddle, D.R., 1999. "Improved Forest Information Extraction Through Integration of a Canopy Reflectance Model and an Evidential Reasoning Classifier," *Proceedings of the Fourth International Airborne Remote Sensing Conference and Exhibition/21st Canadian Symposium on Remote Sensing*, Ottawa, Ontario, June 21-24, 1999, Vol. 2, pp. 115-122.

Peddle, D.R., F.G. Hall and E.F. LeDrew, 1999. "Spectral Mixture Analysis and Geometric Optical Reflectance Modelling of Boreal Forest Biophysical Structure," *Remote Sensing of Environment*, Vol. 67, No. 3, pp. 288-297.

Peddle, D.R. and R.L. Johnson, 2000. "Spectral Mixture Analysis of Airborne Remote Sensing Imagery for Improved Prediction of Leaf Area Index in Mountainous Terrain, Kananaskis Alberta," *Canadian Journal of Remote Sensing*, Vol. 26, No. 3, pp. 177-188.

Phinn, S. R., P. Scarth, and D. Mitchell, 1999. "Estimation of Forest Structural Parameters for Forestry and Koala Habitat Monitoring in South-East Queensland, Australia," *Proceedings of the Fourth International Airborne Remote Sensing Conference and Exhibition*, Ottawa, ON, June 21-24, 1999, Vol. 2, pp. 179-186.

Pinty, B. And M.M. Verstraete, 1991. "GEMI: a non-linear index to monitor global vegetation from satellites," *Vegetatio*, Vol. 101, pp. 15-20.

Prenzel, B., 2000. Personal communication, Department of Geography, York University.

Price, J.C., 1997. "Spectral Band Selection for Visible-Near Infrared Remote Sensing: Spectral-Spatial Resolution Tradeoffs," *IEEE Transactions on Geoscience and Remote Sensing*, Vol. 35, No. 5, pp. 1277-1285.

Qi, J., A. Chehbouni, A.R. Huete, Y.H. Kerr, and S. Sorooshian, 1994. "A Modified Soil Adjusted Vegetation Index," *Remote Sensing of Environment*, Vol. 48, No. 2, pp. 119-126.

Raghu, P.P., R. Poongodi, and Yegnanarayana, 1995. "A Combined Neural Network Approach for Texture Classification," *Neural Networks*, Vol. 8, No. 6, pp. 975-987.

Ray, T.W., 1994. "A FAQ on Vegetation in Remote Sensing: Version 1.0," *On-line publication from the Devision of Geological and Planetary Sciences*, California Institute of Technology, FTP:kepler.gps.caltech.edu - /pub/Terrill/rsvegfaq.txt

Richardson, A.J., and C.L. Wiegand, 1977. "Distinguishing vegetation from soil background information," *Photogrammetric Engineering and Remote Sensing*, Vol. 43, pp. 1541-1552.

Riou, R. and F. Seyler, 1997. "Texture Analysis of Tropical Rain Forest Infrared Satellite Images," *Photogrammetric Engineering and Remote Sensing*, Vol. 63, No. 5, pp. 515-521.

Rotunno, O.C., P.M. Treitz, E.D. Soulis, P.J. Howarth, and N. Kouwen, 1996. "Texture Processing of Synthetic Aperture Radar Data using Second-Order Spatial Statistics," *Computers and Geosciences*, Vol. 22, No. 1, pp. 27-34.

Roujean, J.L. and F.M. Breon, 1995. "Estimating PAR absorbed vegetation from bi-directional reflectance measurements," *Remote Sensing of Environment*, Vol. 51, pp. 375-384.

Rouse, J.W., R.H. Haas, J.A. Schell, and D.W. Deering, 1974. "Monitoring vegetation systems in the Great Plains with ERTS," *NASA/GSFC Type III Final Report*, Greenbelt, Md. 371 pp.

Rozgonyi, G., 1995. *Statistics for Engineers*. University of Wollongong, Australia, On-Line Publication. http://engineering.uow.edu.au/Courses/Stats/index.html

Sampson, P.H., 2000. *Forest Condition Assessment: An Examination of Scale, Structure, and Function Using High Spatial Resolution Remote Sensing Data*, M.Sc. Thesis, York University, 157 pp.

Sampson, P.H., G.H. Mohammed, S.J. Colombo, T.L. Noland, J.R. Miller, and P.J. Zarco-Tejada, 1998. *Bioindicators of Forest Sustainabiligy Progress Report*, Forest Research Information Paper No. 142, Queen's Printer for Ontario, 18 pp.

Sampson, P.H., G.H. Mohammed, P.J. Zarco-Tejada, J.R. Miller, T.L. Noland, D. Irving, P.M. Treitz, S.J. Colombo, and J. Freemantle, 2000. "Bioindicators of Forest Condition: A Physiological, Remote Sensing Approach," *The Forestry Chronicle*, Vol. 76, No. 6, pp. 941-952.

Schmuck, G., J. Verdebout, S.L. Ustin, A.J. Siever, and S. Jacquemoud, 1998. "Vegetation and biochemical indices retrieved from a multitemporal AVIRIS data

set," *Centre for Spatial Technologies and Remote Sensing (CSTARS)*, http://cstars.ucdavis.edu/papers/sustin/agriculture/spieindices/paper.html.

Seed, E. D., and D. J. King, 2000. "Determination of Mixed Boreal Forest Stand Biophysical Structure Using Large Scale Airborne Digital Camera Imagery," Draft paper, Carleton University.

Seed, E. D., D. J. King, P. K. E. Pellikka, 1999. "Multivariate Analysis of Low Cost Airborne CIR Imagery For The Determination of Forest Canopy Structure," *Proceedings of the Fourth International Airborne Remote Sensing Conference and Exhibition*, Ottawa, ON, June 21-24, 1999, Vol. 2, pp. 139-146.

Sellers, P.J., 1985. "Canopy reflectance, photosynthesis, and transpiration," *International Journal of Remote Sensing*, Vol. 6, pp. 1335-1372.

Shapiro, S. S., M.B. Wilk, and H.J. Chen, 1968. "A comparative study of various tests of normality," *Journal of the American Statistical Association*, Vol. 63, pp. 1343-1372.

Spanner, M.A., L.L. Pierce, D.L. Peterson, and S.W. Running, 1990. "Remote sensing of temperate conifierous forest leaf area index. The influence of canopy closure, understory vegetation, and background reflectance," *International Journal of Remote Sensing*, Vol. 11, No. 1, pp. 95-111.

St.-Onge, B., 1999. "Topographic Effects on the Texture of High-Resolution Forest-Stand Image Meaured by the Semivariogram," *Photogrammetric Engineering and Remote Sensing*, Vol. 65, No. 8, pp. 923-935.

Taylor, N.W. (Chair) 1999. "Competing realities: The boreal forest at risk," *Report of the sub-committee on boreal forest of the standing Senate committee on agriculture and forestry*, Ottawa, ON.

Ter-Mikaelian, M. and R.A. Lautenschlager, 2000. "Developing predictive equations for leaf area and biomass for sugar bushes in eastern Ontario," *Ontario Forest Research Institute (OFRI) draft document*, 28 pp.

Thenkabail, P.S., R.B. Smith, and E. De Pauw, 1999. "Hyperspectral Vegetation Indices for Determining Agricultural Crop Characteristics," *CEO Research Publication Series*, Centre for Earth Observation, Yale University, No. 1, 39 pp.

Tian, X. and G.E. Murphy, 1997. "Detection of Trimmed and Occluded Branches on Harvested Tree Stems using Texture Analysis," *International Journal of Forest Engineering*, Vol. 8, No. 2, pp. 65-74.

Treitz, P., 2001. "Variogram Analysis of High Spatial Resolution Remote Sensing Data: An Examination of Boreal Forest Ecosystems," *International Journal of Remote Sensing*, Vol. 22, No. 18, pp. 3895-3900.

Treitz, P.M., and P.J. Howarth, 1999. "Hyperspectral Remote Sensing for Estimating Biophysical Parameters of Forest Ecosystems," *Progress in Physical Geography*, Vol. 23, No. 3, pp. 359-391.

Treitz, P.M., P.J. Howarth, O.R. Filho, and E.D. Soulis, 2000. "Agricultural Crop Classification Using SAR Tone and Texture Statistics," *Canadian Journal of Remote Sensing*, Vol. 26, No. 1, pp. 18-29.

Trimble Navigation Limited, 1996. *GeoExplorer II Operation Manual*, Trimble Navigation Limited, Sunnyvale, CA.

Upton, G.J.G., and B. Fingleton, 1989. *Spatial data analysis by example. Volume 2: Categorical and directional data.* Wiley, Chichester, England.

Ustin, S. L., M. O. Smith, D. A. Roberts, J. A. Gamon, and C. B. Field, 1992. "Using AVIRIS Images to Measure Temporal Trends in Abundance of Photosynthetic and Nonphotosynthetic Canopy Components," *Summaries of the Third Annual JPL Airborne Geoscience Workshop*, Pasadena, CA, June 1-5, 1992, JPL Publication 92-14, pp. 5-7.

Vane, G., J.E. Duval, and J.B. Wellman, 1993. *Imaging spectroscopy of the earth and other solar system bodies.* In Remote Geochemical Analysis: Elemental and Mineralogical Composition. Cambridge University Press, Cambridge, pp. 121-143.

Verstraete, M.M., and B. Pinty, 1996. "Designing Optimal Spectral Indexes for Remote Sensing Applications," *IEEE Transactions on Geoscience and Remote Sensing*, Vol. 34, No. 5, pp. 1254-1265.

Vogelmann, J.E., B.N. Rock, and D.M. Moss, 1993. "Red edge spectral measurements from sugar maple leaves," *International Journal of Remote Sensing*, Vol. 14, No. 8, pp. 1563-1575.

Wang, L. and D. He, 1990. "Texture Unit, Texture Spectrum, and Texture Analysis," *IEEE Transactions on Geoscience and Remote Sensing*, Vol. 28, No. 4, pp. 509-512, 1990.

Waring, R.H. and S.W. Running, 1998. *Forest Ecosystems: Analysis at Multiple Scales*, Second Edition, San Deigo: Academic Press, 1998.

Woodcock, C.E. and Strahler, A.H., 1987. "The factor of scale in remote sensing", *Remote Sensing of Environment*, Vol. 21, pp. 311-312.

Yuan, X., D. King, and J. Vlcek, 1991. "Sugar Maple Decline Assessment Based on Spectral and Textural Analysis of Multispectral Aerial Videography," *Remote Sensing of Environment*, Vol. 37, pp. 47-54.

Xia, L., 1994. "A two-axis adjusted vegetation index (TWVI)," *International Journal of Remote Sensing*, Vol. 15, No. 7, pp. 1447-1458.

Zarco-Tejada, P.J., 2000. *Hyperspectral Remote Sensing of Closed Forest Canopies: Estimation of Chlorophyll Fluorescence and Pigment Content*, PhD Thesis, Earth and Space Science, York University, Toronto, 209 pp.

Zarco-Tejada, P.J., and J. R. Miller, 1999. "Optical Indices as Bioindicators of Forest Condition from Hyperspectral CASI data," *Proceedings of the 19th Symposium of the European Association of Remote Sensing Laboratories (EARSeL)*, Valladolid, Spain, March 31 – June 2, 1999, 6 pp.

Zarco-Tejada, P.J., J.R. Miller, G.H. Mohammed, T.L. Noland, and P.H. Sampson, 1999. "Canopy Optical Indices from Infinite Reflectance and Canopy Reflectance Models for Forest Condition Monitoring: Application to Hyperspectral *CASI* Data," *Proceedings of the IEEE 1999 International Geoscience and Remote Sensing Symposium, IGARSS'99*, Hamburg, Germany, June 28 – July 2, 1999, 5 pp.

Zhou, J. and D. Civco, 1998. "Using the Wavelet Transform to Extract Texture Features From Remote Sensing Images," *Proceedings of the First International*

Conference on Geospatial Information in Agriculture and Forestry, Lake Buena Vista, Florida, USA, June 1-3, 1998, Vol. 1., pp. 574-581).

A.0 APPENDIX

A.1 Spectral Indices

A.1.1 Broad-Band Ratio-Based Indices

General Type	Name	Formula	Comments	Reference
Basic Vegetation Indices	Ratio Vegetation Index (RVI)	ρ_{NIR}/ρ_{red}	Range of 0 to infinity. Often used as a quick estimate of vegetated areas.	Jordan (1969); Rouse *et al.* (1974)
	Normalized Difference Vegetation Index (NDVI)	$(\rho_{NIR} - \rho_{red})/(\rho_{NIR} + \rho_{red})$	Very common and well studied index. Range of –1 to +1. Positive values indicate vegetated areas.	Rouse *et al.* (1974)
	Transformed NDVI (TNDVI)	$(NDVI + 0.5)^{0.5}$	Not reported to have any significant benefit over the NDVI.	Deering *et al.* (1975)
	Infrared Percentage Vegetation Index (IPVI)	$\rho_{NIR}/(\rho_{NIR} + \rho_{red})$	Based on NDVI. Eliminates negative values in the output. Designed to increase speed of calculation. Output values can range from 0 to 1.	Crippen (1990)
	Modified Normalized Difference Vegetation Index (MNDVI)	$MNDVI = NDVI(1+C_2H_2)/(1+C_1H_1) = MNDVI_0(1+C_2H_2)$	Designed to be a feedback system, where H_1 is a function of soil and atmospheric noise, H_2 should approach zero, C_1 and C_2 are empirical coefficients.	Liu and Huete (1995)
	Modified Simple Ratio (MSR)	$\frac{\rho_{NIR}/\rho_{red} - 1}{(\rho_{NIR}/\rho_{red})^{0.5} + 1}$	Not reported to have any significant benefit over the NDVI.	Chen (1996)
	Renormalized Difference Vegetation Index	$\frac{(\rho_{NIR} - \rho_{red})}{(\rho_{NIR} + \rho_{red})^{0.5}}$	Not reported to have any significant benefit over the NDVI.	Roujean and Breon (1995)

Soil Adjusted Indices	Soil Adjusted Vegetation Index (SAVI)	$\frac{\rho_{NIR} - \rho_{red}}{\rho_{NIR} + \rho_{red} + L}(1 + L)$ L = correction factor that ranges from 0 for high vegetation cover to 1 for low vegetation cover. Typically set to 0.5.	Designed to minimize the effects of soil background. Equivalent to NDVI if L=0 (high vegetation cover). Isovegetation lines converge in the negative quadrant. Less sensitive to change in low vegetation cover than NDVI and more sensitive to atmospheric variation.	Huete and Tucker (1991) Qi *et al.* (1994)
	Transformed Soil Adjusted Vegetation Index (TSAVI)	$\frac{s(\rho_{NIR} - s * \rho_{red} - a)}{(a * \rho_{NIR} + \rho_{red} - a * s + X * (1 + s * s))}$ a = soil line intercept s = slope of the soil line X = empirical adjustment factor	Designed to be more sensitive to soil brightness and moisture content than SAVI. Less sensitive to change in low vegetation cover than NDVI and more sensitive to atmospheric variation.	Baret *et al.* (1989); Baret and Guyot (1991).
	$SAVI_2$	$\rho_{NIR}/(\rho_R+0)$ Where: 0 = A/B $A = \rho_{\infty,NIR} + (0.067-\rho_{\infty,NIR})\exp(-k_{NIR}LAI) - 1.16\rho_{\infty,R}\exp[(k_R-k_{NIR})LAI] - \exp(-k_{NIR}LAI)$ $B = 1.16\exp[(k_R - K_{NIR})LAI]$	A special case of Huete's SAVI. Parameters derived using the SAIL model for wheat canopy reflectance. Requires iterations to find the best parameters. Prone to high errors when subject to conditions of low zenith angles combined with erectophile canopies.	Major *et al.* (1990)
	Modified Soil Adjusted Vegetation Index (MSAVI)	$\frac{\rho_{NIR} - \rho_{red}}{\rho_{NIR} + \rho_{red} + L}(1 + L)$ L = 1 – 2*s*NDVI*WDVI S = slope of soil line	Does not require prior knowledge about the vegetation cover to determine L (Unlike SAVI, TSAVI). L can vary across the image.	Qi *et al.* (1994)
	Second MSAVI (MSAVI2)	$0.5(2(\rho_{NIR}+1) - \sqrt{(2\rho_{NIR}+1)^2 - 8(\rho_{NIR} - \rho_{red})})$	Designed based on MSAVI. Does not require calculation of NDVI, WDVI.	Qi *et al.* (1994)
	Two-axis adjusted vegetation index (TWVI)	$((\rho_{NIR} - \rho_{red} - \Delta)/(\rho_{NIR} - \rho_{red} + L))(1+L)$ Where: $\Delta = \sqrt{2}e^{-kLAI}D = \sqrt{2}(1-(l_\lambda)/(l_\infty-1))D$	Designed to compensate for more than one soil type. Δ is the deviation caused by soil distance offset D in the secondary axis.	Xia (1994)

Atmospheric Adjusted Vegetation Indices	Global Environmental Monitoring Index (GEMI)	$H(1-0.25H)-\frac{\rho_{red}-0.125}{1-\rho_{red}}$ $H=\frac{2(\rho_{NIR}^2-\rho_{red}^2)+1.5\rho_{NIR}+0.5\rho_{red}}{\rho_{NIR}+\rho_{red}+0.5}$	Minimizes atmosphere-induced variations. Especially sensitive at high vegetation cover. Non-linear index.	Pinty and Verstraete (1991)
	**Soil adjusted Atmospheric Resistant Vegetation Index (SARVI)	$\frac{\rho_{NIR}-\rho_{rb}(1+L)}{\rho_n+\rho_{rb}+L}$	Designed to minimize both soil and atmospheric noise.	Kaufman and Tanré (1994)
	**Atmosphere Soil Vegetation Index (ASVI)	$0.5(2(\rho_{NIR}+1)-\sqrt{(2\rho_{NIR}+1)^2-8(\rho_{NIR}-\rho_{rb})})$ $\rho_{rb}=\rho_{red}-\gamma(\rho_{blue}-\rho_{red})$	Designed as a modification to MSAVI2 by substituting the red reflectance for the corrected red/blue relationship. Note that any of the modified SAVI equations could be changed with this method.	Qi *et al.* (1994)
	**Atmospherically Resistent Vegetation Index (ARVI)	$\frac{\rho_{NIR}-\rho_{rb}}{\rho_{NIR}+\rho_{rb}}$ $\rho_{rb}=\rho_{red}-\gamma(\rho_{blue}-\rho_{red})$	One of the first indices designed to correct for atmospheric effects.	Kaufman and Tanré (1992).
	Enhanced Vegetation Index (EVI)	$2.5\left\|\frac{\rho^*_{NIR}-\rho^*_{red}}{1+\rho^*_{NIR}+6\rho^*_{red}-7.5/\rho^*_{blue}}\right\|$ p* is apparent reflectance	Based on SARVI. Also called Soil and Atmospheric Resistant Vegetation Index (SARVI2)	Huete *et al.* (1997)
Other	Thermal NDVI	Ts/NDVI	Multi-temporal thermal information was shown to improve AVHRR based classifications incorporating NDVI. Areas with very small NDVI values (e.g. deserts) cause non-linear behavior of this index.	Lambin and Ehrlich (1995)

** Qi *et al.* (1994) compared these atmospheric indices to GEMI and showed that they were very slightly more sensitive to changes in vegetation cover and less sensitive to the atmosphere and the soil than GEMI for moderate to high vegetation cover. Qi *et al.* (1994) also found that the insensitivity to atmospheric influences and soil breaks down violently for low vegetation cover.

A.1.2 Common Broad-Band Orthogonal Indices

Name	Formula	Comments	Reference
Simple Vegetation Index (VI)	NIR – red	High values indicate vegetated areas. Negative values for materials that reflect more in the visible than infrared (water, clouds, snow, etc.) Some discrepancy as to the origin of this index. Difference Vegetation Index (DVI) and Ashburn's Vegetation Index (AVI) are essentially the same.	Richardson and Wiegand (1977); Lillesand and Kiefer (1994); Ray (1994)
Perpendicular Vegetation Index (PVI)	$\sin(a)\rho_{NIR} - \cos(a)\rho_{red}$	Allow for soil lines of different slopes. Very sensitive to atmospheric change.	Richardson and Wiegand (1977); Qi *et al.* (1994)
Weighted Difference Vegetation Index (WDVI)	$\rho_{NIR} - g * \rho_{red}$ g = slope of soil line	Allow for soil lines of different slopes. Very sensitive to atmospheric change.	Clevers (1988)
Green Vegetation Index (GVI)	$C_1\rho_1 + C_2\rho_2 + C_3\rho_3 + C_4\rho_4$ $C_{TM1}\rho_{TM1} + C_{TM2}\rho_{TM2} + C_{TM3}\rho_{TM3} + C_{TM4}\rho_{TM4} + C_{TM5}\rho_{TM5} + C_{TM7}\rho_{TM7}$	Tasseled Cap transformation designed to detect green vegetation. C coefficients are sensor dependent.	Kauth and Thomas (1976); Jensen (1996); Crist and Cicone (1984); Jackson (1983)
Soil Brightness Index (SBI)	$C_1\rho_1 + C_2\rho_2 + C_3\rho_3 + C_4\rho_4$ $C_{TM1}\rho_{TM1} + C_{TM2}\rho_{TM2} + C_{TM3}\rho_{TM3} + C_{TM4}\rho_{TM4} + C_{TM5}\rho_{TM5} + C_{TM7}\rho_{TM7}$	Tasseled Cap transformation designed to detect soil. C coefficients are sensor dependent. Many of the soil indices are based on the concepts of this index.	Kauth and Thomas (1976); Jensen (1996); Crist and Cicone (1984); Jackson (1983)
Yellow Stuff Index (YSI)	$C_1\rho_1 + C_2\rho_2 + C_3\rho_3 + C_4\rho_4$	Tasseled Cap transformation that typically shows the dead vegatation. C coefficients are sensor dependent.	Kauth and Thomas (1976); Jensen (1996)
Non-such Index (NSI)	$C_1\rho_1 + C_2\rho_2 + C_3\rho_3 + C_4\rho_4$	Tasseled Cap transformation that illustrates atmospheric effects. C coefficients are sensor dependent.	Kauth and Thomas (1976); Jensen (1996)

A.1.3 Narrow-Band Ratio-Based Indices

Index	Formula	Comments	Reference
Optimal narrow-band NDVI	$NDVI_{ij} = (R_j-R_i)/(R_j+R_i)$ R_i, R_j = reflectance in bands i and j	All possible band combinations in the red/NIR region are tested for correlation with the biophysical parameter of interest.	Thenkabail *et al.* (1999)
Photochemical Reflectance Index (PRI)	$PRI_1 = (\rho_{528} - \rho_{567})/(\rho_{528} + \rho_{567})$ $PRI_2 = (\rho_{531} - \rho_{570})/(\rho_{531} + \rho_{570})$ $PRI_3 = (\rho_{550} - \rho_{531})/(\rho_{550} + \rho_{531})$ $PRI_4 = (\rho_{570} - \rho_{539})/(\rho_{570} + \rho_{539})$	Four versions of the same index. Varies with vegetation type, photosynthetic capacity, and efficiency of radiation use.	1&2) Gamon *et al.* (1995) 3&4) Zarco-Tejada *et al.* (1999)
Versions of NDVI	a. $NDVI = (\rho_{831} - \rho_{667})/(\rho_{831} + \rho_{667})$ b. $NDVI = (\rho_{774} - \rho_{667})/(\rho_{774} + \rho_{667})$	There have been multiple narrow band versions of this index reported for various applications. b.) used as pigment index	a) Merton and Harvey (1997); Merton (1998) b) Zarco-Tejada *et al.* (1999)
Vogelmann sugar maple indices	$Vog1 = (\rho_{740})/(\rho_{720})$ $Vog2 = (\rho_{734} - \rho_{747})/(\rho_{715} + \rho_{726})$ $Vog3 = (\rho_{734} - \rho_{747})/(\rho_{715} + \rho_{720})$	Indices designed based on the spectral measurements of sugar maple leaves. Vog1-3 are red-edge indices.	Vogelmann *et al.* (1993); Zarco-Tejada *et al.* (1999)
Gitelson and Merzlyak chlorophyll 1&2	$G\_M1 = (\rho_{750})/(\rho_{550})$ $G\_M2 = (\rho_{750})/(\rho_{700})$	Designed for the measurement of chlorophyll content in plant leaves.	Gitelson and Merzlyak (1997)
Lichtenthaler indices 1 to 3	$Lic1 = (\rho_{800} - \rho_{680})/ (\rho_{800} + \rho_{680})$ $Lic2 = (\rho_{440})/(\rho_{690})$ $Lic3 = (\rho_{440})/(\rho_{740})$	Indices designed to detect stress in green vegetation leaves using UV-laser induced fluorescence bands	Lichtenthaler *et al.* (1996a,b)
Simple Ratio Pigment Index (SRPI)	$SRPI = (\rho_{430})/ (\rho_{680})$	*	Zarco-Tejada *et al.* (1999)
Normalized Phaeophytiniz Index (NPQI)	$NPQI = (\rho_{415} - \rho_{435})/ (\rho_{415} + \rho_{435})$	*	Zarco-Tejada *et al.* (1999)

Normalized Pigment Chlorophyll Ratio Index (NPCI)	NPCI = $(\rho_{680} - \rho_{430})/(\rho_{680} + \rho_{430})$	*	Zarco-Tejada *et al.* (1999)
Greenness Index (G)	G = $(\rho_{554})/(\rho_{677})$	*	Zarco-Tejada *et al.* (1999)
Structure Intensive Pigment Index (SIPI)	SIPI = $(\rho_{800} - \rho_{450})/(\rho_{800} + \rho_{650})$	*	Zarco-Tejada *et al.* (1999)
Simple Ratio (SR)	SR = $(\rho_{774})/(\rho_{677})$	*	Zarco-Tejada *et al.* (1999)
Carter Indices	Ctr1 = $(\rho_{695})/(\rho_{420})$ Ctr2 = $(\rho_{695})/(\rho_{760})$	Developed for early and pre-visual detection of stress in pine forests. Proved that imagery at these wavelengths is superior to thermal imagery for this purpose.	Carter (1994) Carter (1998)

* Note: Use and format of these indices reported by Zarco-Tejada *et al.* (1999) in a study to link physiologically-based indicators to optical indices and scale up from leaf-level to canopy level using canopy reflectance models.

A.1.4 Hyperspectral Indices Designed Using Differentiation/Integration

Index	Formula	Comments	Reference
First Difference Transformation	$D\lambda_i = (R_{\lambda i-g} - R\lambda_{i+g})/\Delta\lambda$ $D\lambda_i$ = first difference transformation at band i. g = gap R = reflectance	Used to relate chlorophyll *a* concentration to water reflectance.	Novo *et al.*(1995)
1DL_DGVI	$1DL\_DGVI = \sum_{\lambda_i}^{\lambda_n} \lvert\rho'(\lambda_i) - \rho'(\lambda_i)\rvert\Delta\lambda_i$	First-order derivative green vegetation index derived using local baseline.	Elvidge and Chen (1995)
1DZ_DGVI	$1DZ\_DGVI = \sum_{\lambda_i}^{\lambda_n} \lvert\rho'(\lambda_i)\rvert\Delta\lambda_i$	First-order derivative green vegetation index derived using zero baseline.	Elvidge and Chen (1995)
2DZ_DGVI	$2DZ\_DGVI = \sum_{\lambda_i}^{\lambda_n} \lvert\rho''(\lambda_i)\rvert\Delta\lambda_i$	Second-order derivative green vegetation index derived using zero baseline.	Elvidge and Chen (1995)
Double Peak Ratio Indices 1-4	DPR1 = $D_{\lambda 0[680\text{-}750]}/D_{\lambda 0+12}$ DPR2 = $D_{\lambda 0[680\text{-}750]}/D_{\lambda 0+22}$ DP21 = $D_{\lambda 0[680\text{-}750]}/D_{703}$ DP22 = $D_{\lambda 0[680\text{-}750]}/D_{720}$	*Derivative indices used to correlate with chlorophyll fluorescence and pigments *** (See Note in Table 21)**	Zarco-Tejada *et al.* (1999)
Lichtenthaler 4	$Lic4 = \int_{450}^{680} R$	Indices designed to detect stress in green vegetation leaves using UV-laser induced fluorescence bands	Lichtenthaler *et al.* (1996a,b)
Vogelmann 4	$Vog4 = D_{715}/D_{705}$	Index designed based on the spectral measurements of sugar maple leaves.	Vogelmann *et al.* (1993); Zarco-Tejada *et al.* (1999)
Area Red Edge Peak (ADR)	$ADR = \int_{680}^{760} D$	* Integral over the red edge region.	Zarco-Tejada *et al.* (1999)
λp indices 1-3	lpr = $\lambda_{max[680\text{-}750]}$ lp1g = $\lambda_{max[500\text{-}600]}$ lp2g = $\lambda_{min[500\text{-}600]}$	* Used to correlate with chlorophyll fluorescence and pigments	Zarco-Tejada *et al.* (1999)
R_0	$R_0 = \rho_{min[650\text{-}700]}$	* Used to correlate with chlorophyll fluorescence and pigments	Zarco-Tejada *et al.* (1999)
R_s	$R_s = \rho_{max[700\text{-}770]}$	* Used to correlate with chlorophyll fluorescence and pigments	Zarco-Tejada *et al.* (1999)

A.1.5 Other Hyperspectral Indices

Index	Formula	Comments	Reference
Optimal Multiple Narrow-Waveband Reflectivity (OMNBR)	$BP = \sum_{J=1}^{N} a_{ij} R_j$ BP = Biophysical parameter of interest R = reflectance in band j a = coefficient for reflectance in band j for i^{th} variable	These indices were derived for crop variables using the MAXR algorithm in SAS. They describe the amount of variability for a biophysical parameter of interest that is explained by the band(s). Significance testing can be used to prevent over-fitting when increasing the number of bands.	Thenkabail *et al.* (1999)
Red-Edge Vegetation Stress Index (RVSI)	$RSVI = \left(\frac{\rho_{714} + \rho_{752}}{2} \right) - \rho_{733}$	Designed as a general index to measure stress in disparate vegetation communities (at the Jasper Ridge Biological Preserve, Palo Alto, California), based on upper red-edge geometry.	Merton (1998)
Green Vegetation Fraction (GVF)	$GVF = a_v/(a_v + a_s)$ a_s = abundance of soil in pixel spectrum a_v = abundance of vegetation in pixel spectrum	Created based on the inversion of a non-linear model of ground reflectance.	Ustin *et al.* (1992); Schmuck *et al.* (1998)
% Nitrogen	$0.486 + (0.001\rho_{781}) + (0.003\rho_{1640})$	Used to estimate canopy nitrogen content from AVIRIS data.	Aber and Martin (1995)
% Lignin	$33.36 - (0.048\rho_{822}) + (0.106\rho_{627}) + (0.005\rho_{756}) + (0.052\rho_{1660})$	Used to derive a canopy lignin content from AVIRIS data in temperate forests of diverse types.	Aber and Martin (1995)

A.2 Calibration Field Metrics (FH and ISD Sites)

A.2.1 Quadratic DBH

Units of Measure: cm

Study Site	Plot a	Plot b	Plot c	Plot d	Centre	Total
FH A02	-	-	-	-	26.52	26.52
FH A063	-	-	-	-	30.61	30.61
FH A064	-	-	-	-	35.71	35.71
FH A065	-	-	-	-	23.58	23.58
FH A066	-	-	-	-	33.5	33.5
FH A067	-	-	-	-	31.43	31.43
ISD 12	34.20	36.13	34.56	37.55	34.76	35.36
ISD 14	22.10	34.92	30.08	33.78	43.04	33.11
ISD 15	37.38	37.18	19.46	46.65	25.06	31.27
ISD 19	18.10	27.41	26.65	31.71	-	24.18
ISD 21	24.28	23.13	24.85	26.69	20.69	24.01
ISD 23	25.95	22.04	32.99	24.82	31.05	26.75
ISD 3	31.38	30.15	23.13	24.08	24.88	26.46
ISD 31	27.38	31.55	31.47	34.37	-	31.57
ISD 40	25.72	32.24	38.79	27.49	-	29.8
ISD 5	31.87	33.33	21.36	30.01	25.46	28.28

A.2.2 Arithmetic DBH

Units of Measure: cm

Study Site	Plot a	Plot b	Plot c	Plot d	Centre	Total
FH A02	-	-	-	-	25.16	25.16
FH A063	-	-	-	-	28.36	28.36
FH A064	-	-	-	-	32.91	32.91
FH A065	-	-	-	-	21.99	21.99
FH A066	-	-	-	-	30.40	30.40
FH A067	-	-	-	-	29.67	29.67
ISD 12	31.66	33.19	32.75	34.88	31.74	32.72
ISD 14	21.28	33.75	27.89	32.33	38.74	30.41
ISD 15	36.65	33.92	17.29	45.76	21.04	27.39
ISD 19	17.05	23.22	25.12	28.27	-	21.49
ISD 21	22.66	22.18	23.24	24.57	19.43	22.46
ISD 23	23.53	17.84	28.90	21.85	27.69	23.01
ISD 3	30.43	28.93	21.98	23.30	23.95	25.28
ISD 31	25.02	28.72	29.90	30.94	-	28.80
ISD 40	22.21	29.40	35.88	21.99	-	25.55
ISD 5	30.36	28.32	20.18	27.69	23.23	25.57

A.2.3 Tree Height

Units of Measure: m

Study Site	Plot a	Plot b	Plot c	Plot d	Centre	Total
FH A02	-	-	-	-	22.18	22.18
FH A063	-	-	-	-	22.43	22.43
FH A064	-	-	-	-	30.18	30.18
FH A065	-	-	-	-	16.76	16.76
FH A066	-	-	-	-	18.40	18.40
FH A067	-	-	-	-	23.94	23.94
ISD 12	22.76	23.22	21.61	21.81	22.48	22.41
ISD 14	17.25	21.15	19.21	20.43	22.76	20.04
ISD 15	17.73	17.04	13.98	19.18	14.53	15.83
ISD 19	15.79	18.19	22.95	23.77	-	18.86
ISD 21	17.48	18.13	20.74	16.58	16.22	18.08
ISD 23	17.05	14.36	18.09	17.35	20.32	16.93
ISD 3	20.53	18.08	18.03	18.68	20.42	19.18
ISD 31	19.90	22.76	23.28	21.56	-	21.77
ISD 40	17.21	21.14	19.05	16.19	-	18.16
ISD 5	21.86	20.47	19.54	20.21	21.41	20.68

A.2.4 Crown Diameter

Units of Measure: m

Study Site	Plot a	Plot b	Plot c	Plot d	Centre	Total
FH A02	-	-	-	-	4.65	4.65
FH A063	-	-	-	-	4.88	4.88
FH A064	-	-	-	-	5.90	5.90
FH A065	-	-	-	-	5.13	5.13
FH A066	-	-	-	-	5.76	5.76
FH A067	-	-	-	-	6.64	6.64
ISD 12	5.31	4.80	6.64	5.98	6.73	5.90
ISD 14	4.78	5.92	5.67	6.45	5.59	5.67
ISD 15	8.51	7.62	5.48	9.66	5.89	6.90
ISD 19	5.06	5.63	6.13	7.68	-	5.75
ISD 21	6.51	5.04	4.81	5.57	5.77	5.47
ISD 23	6.32	4.95	7.11	6.50	6.46	6.07
ISD 3	5.49	5.77	4.88	5.62	5.04	5.33
ISD 31	6.17	5.61	6.26	7.50	-	6.51
ISD 40	6.19	8.10	8.53	6.25	-	6.99
ISD 5	8.90	8.55	6.24	7.45	6.24	7.33

A.2.5 Crown Closure – Circular

Units of Measure: unitless fraction

Study Site	Plot a	Plot b	Plot c	Plot d	Centre	Total
FH A02	-	-	-	-	1.36	1.36
FH A063	-	-	-	-	0.96	0.96
FH A064	-	-	-	-	1.04	1.04
FH A065	-	-	-	-	1.08	1.08
FH A066	-	-	-	-	0.62	0.62
FH A067	-	-	-	-	1.23	1.23
ISD 12	0.88	0.71	1.16	0.81	1.63	1.04
ISD 14	0.53	0.78	1.50	0.90	0.80	0.90
ISD 15	1.16	1.39	1.10	1.01	1.03	1.14
ISD 19	1.04	1.41	1.54	1.73	-	1.32
ISD 21	2.64	2.00	1.86	1.61	1.75	1.97
ISD 23	1.97	1.51	1.46	1.20	1.28	1.48
ISD 3	1.05	1.16	0.97	1.40	1.31	1.18
ISD 31	2.44	1.86	2.23	1.97	-	2.08
ISD 40	2.28	4.37	1.53	3.44	-	2.91
ISD 5	2.50	2.51	1.57	2.14	1.85	2.11

A.2.6 Crown Closure - Ellipse

Units of Measure: unitless fraction

Study Site	Plot a	Plot b	Plot c	Plot d	Centre	Total
FH A02	-	-	-	-	1.35	1.35
FH A063	-	-	-	-	0.95	0.95
FH A064	-	-	-	-	1.03	1.03
FH A065	-	-	-	-	1.05	1.05
FH A066	-	-	-	-	0.62	0.62
FH A067	-	-	-	-	1.21	1.21
ISD 12	0.85	0.68	1.05	0.74	1.54	0.97
ISD 14	0.50	0.73	1.29	0.81	0.72	0.81
ISD 15	1.14	1.38	1.05	0.96	1.01	1.11
ISD 19	1.02	1.37	1.51	1.68	-	1.29
ISD 21	2.45	1.92	1.80	1.51	1.67	1.87
ISD 23	1.95	1.37	1.44	1.19	1.23	1.43
ISD 3	1.00	1.09	0.92	1.29	1.27	1.12
ISD 31	2.35	1.82	2.11	1.90	-	2.00
ISD 40	2.21	4.32	1.52	3.15	-	2.80
ISD 5	2.44	2.49	1.55	2.11	1.83	2.08

A.2.7 Crown Depth

Units of Measure: m

Study Site	Plot a	Plot b	Plot c	Plot d	Centre	Total
FH A02	-	-	-	-	8.41	8.41
FH A063	-	-	-	-	9.26	9.26
FH A064	-	-	-	-	9.67	9.67
FH A065	-	-	-	-	8.04	8.04
FH A066	-	-	-	-	9.85	9.85
FH A067	-	-	-	-	10.47	10.47
ISD 12	10.77	12.04	10.86	10.30	11.02	11.03
ISD 14	9.50	10.16	9.72	9.20	10.54	9.83
ISD 15	10.80	11.23	7.54	11.76	9.32	9.64
ISD 19	8.09	8.85	11.59	12.15	-	9.53
ISD 21	8.95	9.28	10.50	9.55	9.54	9.60
ISD 23	10.46	8.05	10.67	10.81	12.99	10.19
ISD 3	9.39	8.48	8.35	8.21	7.68	8.33
ISD 31	9.06	12.24	11.22	9.84	-	10.46
ISD 40	8.81	12.49	9.33	8.51	-	9.82
ISD 5	11.26	10.97	10.22	10.35	11.31	10.81

A.2.8 Crown Width (major)

Units of Measure: m

Study Site	Plot a	Plot b	Plot c	Plot d	Centre	Total
FH A02	-	-	-	-	4.66	4.66
FH A063	-	-	-	-	5.01	5.01
FH A064	-	-	-	-	5.87	5.87
FH A065	-	-	-	-	5.16	5.16
FH A066	-	-	-	-	5.69	5.69
FH A067	-	-	-	-	6.88	6.88
ISD 12	4.61	3.94	4.85	4.60	5.41	4.70
ISD 14	3.90	4.55	3.93	4.74	3.94	4.15
ISD 15	7.46	6.96	4.49	7.90	5.02	5.92
ISD 19	4.60	4.88	5.40	6.78	-	5.12
ISD 21	5.14	4.20	4.06	4.49	4.90	4.51
ISD 23	5.77	3.85	6.43	5.89	5.41	5.25
ISD 3	4.65	4.78	4.00	4.37	4.32	4.40
ISD 31	5.14	4.98	5.16	6.37	-	5.52
ISD 40	5.29	7.32	7.94	4.97	-	6.02
ISD 5	7.83	7.89	5.63	6.76	5.62	6.62

A.2.9 Crown Width (perpendicular)

Units of Measure: m

Study Site	Plot a	Plot b	Plot c	Plot d	Centre	Total
FH A02	-	-	-	-	4.64	4.64
FH A063	-	-	-	-	4.75	4.75
FH A064	-	-	-	-	5.94	5.94
FH A065	-	-	-	-	5.09	5.09
FH A066	-	-	-	-	5.83	5.83
FH A067	-	-	-	-	6.40	6.40
ISD 12	6.01	5.66	8.43	7.36	8.05	7.10
ISD 14	5.66	7.29	7.40	8.16	7.23	7.18
ISD 15	9.56	8.28	6.46	11.42	6.77	7.87
ISD 19	5.76	6.38	6.86	8.57	-	6.50
ISD 21	7.88	5.88	5.55	6.65	6.64	6.43
ISD 23	6.86	6.06	7.79	7.10	7.50	6.89
ISD 3	6.33	6.76	5.77	6.87	5.77	6.27
ISD 31	7.20	6.23	7.36	8.63	-	7.50
ISD 40	7.08	8.87	9.11	7.53	-	7.97
ISD 5	9.98	9.21	6.86	8.14	6.85	8.05

A.2.10 Stem Density

Units of Measure: #/ha

Study Site	Plot a	Plot b	Plot c	Plot d	Centre	Total
FH A02	-	-	-	-	700	700
FH A063	-	-	-	-	460	460
FH A064	-	-	-	-	350	350
FH A065	-	-	-	-	480	480
FH A066	-	-	-	-	210	210
FH A067	-	-	-	-	330	330
ISD 12	350	350	325	275	400	340
ISD 14	275	275	550	250	300	330
ISD 15	200	275	400	125	300	260
ISD 19	440	500	500	325	-	440.91
ISD 21	725	900	925	600	625	755
ISD 23	575	700	350	325	350	460
ISD 3	375	400	475	525	600	475
ISD 31	750	675	625	410	-	559.0909
ISD 40	625	750	250	950	-	643.75
ISD 5	375	375	475	450	525	440

A.2.11 Height to the Base of the Crown

Units of Measure: m

Study Site	Plot a	Plot b	Plot c	Plot d	Centre	Total
FH A02	-	-	-	-	13.77	13.77
FH A063	-	-	-	-	13.17	13.17
FH A064	-	-	-	-	13.36	13.36
FH A065	-	-	-	-	8.72	8.72
FH A066	-	-	-	-	8.54	8.54
FH A067	-	-	-	-	13.46	13.46
ISD 12	11.99	11.19	10.75	11.51	11.46	11.38
ISD 14	7.75	10.98	9.50	11.23	12.22	10.21
ISD 15	6.93	5.81	6.44	7.42	5.21	6.19
ISD 19	7.70	9.34	11.37	11.62	-	9.34
ISD 21	8.53	8.85	10.24	7.03	6.68	8.48
ISD 23	6.59	6.31	7.41	6.55	7.33	6.74
ISD 3	11.14	9.61	9.68	10.47	12.74	10.85
ISD 31	10.84	10.52	12.06	11.72	-	11.31
ISD 40	8.40	8.65	9.72	7.68	-	8.33
ISD 5	10.60	9.49	9.32	9.86	10.10	9.86

A.2.12 LAI – Derived From Four Inner Rings

Units of Measure: unitless

Study Site	Plot a	Plot b	Plot c	Plot d	Centre	Total
FH A02	-	-	-	-	3.428	3.428
FH A063	-	-	-	-	3.094	3.094
FH A064	-	-	-	-	3.114	3.114
FH A065	-	-	-	-	3.218	3.218
FH A066	-	-	-	-	2.896	2.896
FH A067	-	-	-	-	3.1275	3.1275
ISD 12	2.49	1.56	1.94	2.15	2.41	2.11
ISD 14	1.86	1.7	1.58	1.8	1.85	1.758
ISD 15	2.22	3.61	2.98	4.55	4.06	3.484
ISD 19	3.18	3.71	2.96	3.53	-	3.386
ISD 21	2.32	2.4	2.55	2.55	2.52	2.468
ISD 23	2.45	3.14	4.43	2.81	3.21	3.208
ISD 3	2.18	2.3	2.92	2.4	2.49	2.458
ISD 31	3.19	4.06	3.43	3.02	-	3.5
ISD 40	3.14	3.73	3.98	3.42	-	3.482
ISD 5	3.33	3.41	2.97	2.86	2.73	3.06

A.2.13 LAI – Derived From Five Rings

Unit of Measure: unitless

Study Site	Plot a	Plot b	Plot c	Plot d	Centre	Total
FH A02	-	-	-	-	2.954	2.954
FH A063	-	-	-	-	3.512	3.512
FH A064	-	-	-	-	2.744	2.744
FH A065	-	-	-	-	2.874	2.874
FH A066	-	-	-	-	2.632	2.632
FH A067	-	-	-	-	2.7425	2.7425
ISD 12	2.36	1.51	1.9	2.08	2.29	2.028
ISD 14	1.92	1.66	1.58	2	1.77	1.786
ISD 15	2.13	3.03	2.98	4.01	3.71	3.172
ISD 19	2.96	3.27	2.89	3.27	-	3.116
ISD 21	2.19	2.3	2.38	2.38	2.14	2.278
ISD 23	2.31	2.85	3.86	2.72	2.67	2.882
ISD 3	2.31	2.47	2.65	2.22	2.62	2.454
ISD 31	2.77	3.37	3.37	2.68	-	3.108
ISD 40	2.86	3.08	3.28	3.48	-	3.108
ISD 5	2.89	2.91	2.47	2.46	2.46	2.638

A.2.14 Percent Canopy Openness Derived From Hemispherical Photos

Units of Measure: unitless

Study Site	Plot a	Plot b	Plot c	Plot d	Centre	Total
FH A02	-	-	-	-	6.36	6.36
FH A063	-	-	-	-	5.764	5.764
FH A064	-	-	-	-	7.766	7.766
FH A065	-	-	-	-	7.182	7.182
FH A066	-	-	-	-	8.856	8.856
FH A067	-	-	-	-	7.5825	7.5825
ISD 12	12.32	22.48	16.15	16.48	11.46	15.778
ISD 14	18.39	19.31	21.14	16.72	17.22	18.556
ISD 15	12.19	6.06	6.56	8.47	3.89	7.434
ISD 19	6.13	4.75	9.02	4.8	-	5.962
ISD 21	12.61	11.74	11	10.91	12.47	11.746
ISD 23	11.01	6.53	2.94	9.32	7.9	7.54
ISD 3	13.78	11.19	9.23	11.98	8.97	11.03
ISD 31	8.14	5.01	5.42	8.33	-	6.306
ISD 40	7.07	5.81	4.7	4.67	-	6.028
ISD 5	6.53	6.02	9.03	9.49	10.34	8.282

A.2.15 Number Of Trees

Units of Measure: unitless

Study Site	Plot a	Plot b	Plot c	Plot d	Centre	Total
FH A02	-	-	-	-	70	70
FH A063	-	-	-	-	46	46
FH A064	-	-	-	-	35	35
FH A065	-	-	-	-	48	48
FH A066	-	-	-	-	21	21
FH A067	-	-	-	-	33	33
ISD 12	14.00	14.00	13.00	11.00	16.00	68.00
ISD 14	11.00	11.00	22.00	10.00	12.00	66.00
ISD 15	8.00	11.00	16.00	5.00	12.00	52.00
ISD 19	44.00	20.00	20.00	13.00	-	97.00
ISD 21	29.00	36.00	37.00	24.00	25.00	151.00
ISD 23	23.00	28.00	14.00	13.00	14.00	92.00
ISD 3	15.00	16.00	19.00	21.00	24.00	95.00
ISD 31	30.00	27.00	25.00	41.00	-	123.00
ISD 40	25.00	30.00	10.00	38.00	-	103.00
ISD 5	15.00	15.00	19.00	18.00	21.00	88.00

A.2.16 Basal Area

Units of Measure: m^2/ha

Study Site	Plot a	Plot b	Plot c	Plot d	Centre	Total
FH A02	-	-	-	-	38.68	38.68
FH A063	-	-	-	-	33.84	33.84
FH A064	-	-	-	-	35.34	35.34
FH A065	-	-	-	-	20.95	20.95
FH A066	-	-	-	-	18.51	18.51
FH A067	-	-	-	-	25.61	25.61
ISD 12	32.15	35.88	30.49	30.45	37.95	33.39
ISD 14	10.55	26.34	39.10	22.40	43.65	28.41
ISD 15	21.95	29.86	11.89	21.36	14.80	19.97
ISD 19	11.32	29.50	27.88	25.66	-	20.25
ISD 21	33.58	37.83	44.88	33.57	21.01	34.17
ISD 23	30.41	26.72	29.93	15.73	26.51	25.86
ISD 3	29.00	28.55	19.95	23.91	29.17	26.11
ISD 31	44.16	52.78	48.63	38.05	-	43.76
ISD 40	32.46	61.22	29.55	56.40	-	44.91
ISD 5	29.91	32.72	17.02	31.82	26.72	27.64

A.3 Validation Metrics (TLW)

A.3.1 Field Metrics - Hemispherical Photographs and DBH

#	Treatment	Percent Canopy Openness	LAI From 4 Rings	LAI From 5 Rings	Arithmetic DBH (cm)	Quadratic DBH (cm)
1	clear cut	46.1	0.8	0.7	11.4	11.4
2	shelterwood	12.0	2.8	2.3	28.4	31.9
3	control	26.2	2.4	2.1	23.0	27.5
4	clear cut	21.3	2.2	1.7	18.7	19.1
5	clear cut	20.2	2.0	1.6	15.6	16.2
6	clear cut	6.7	3.3	3.0	21.2	21.2
7	control	6.2	3.5	3.0	21.1	23.0
8	out	8.7	3.0	2.7	22.9	24.9
9	clear cut	47.9	0.7	0.6	11.7	12.6
10	clear cut	31.3	1.5	1.3	19.1	19.9
11	clear cut	-	-	-	12.0	12.2
12	clear cut	53.7	0.5	0.5	16.3	17.1
13	clear cut	37.5	0.9	0.9	14.9	15.5
14	control	5.8	3.6	3.1	23.2	25.5
15	out	9.4	2.9	2.6	27.6	31.2
16	control	4.7	3.8	3.3	24.1	27.0
17	selection	13.6	2.6	2.2	19.6	20.6
18	shelterwood	14.4	2.3	2.0	22.3	25.7
19	shelterwood	10.7	2.7	2.3	17.3	18.7
20	selection	17.0	2.3	1.9	27.6	29.9
21	control	6.2	3.5	3.0	21.7	25.7
22	shelterwood	8.4	3.0	2.7	23.3	28.0
23	shelterwood	26.7	1.5	1.3	21.2	25.2
24	selection	22.1	1.7	1.6	24.9	25.7
25	selection	19.5	1.9	1.7	27.4	30.6
26	shelterwood	20.7	1.9	1.5	14.8	16.3
27	shelterwood	13.0	2.4	2.2	21.0	23.4
28	shelterwood	8.7	2.9	2.6	27.4	29.2
29	control	-	-	-	22.8	27.2
30	clear cut	54.7	0.5	0.5	13.9	14.3
31	clear cut	54.6	0.5	0.5	14.0	14.5
32	selection	-	-	-	25.2	26.3
33	control	-	-	-	29.3	32.1
34	control	9.2	3.1	2.6	20.5	23.3
35	shelterwood	-	-	-	23.0	25.9
36	out	6.9	3.4	2.9	27.5	30.4

A.3.2 Field Metrics - Crown-Width Measurements

#	Treatment	Major Crown Width (m)	Perpendicular Crown Width (m)	Crown Diameter (m)	Crown Closure (circular)	Crown Closure (ellipse)
1	clear cut	4.1	3.6	3.8	0.1	0.1
2	shelterwood	7.1	5.8	6.4	1.0	1.0
3	control	5.7	4.6	5.1	1.2	1.2
4	clear cut	5.9	4.0	4.9	0.3	0.3
5	clear cut	4.8	3.4	4.1	0.5	0.5
6	clear cut	4.5	3.0	3.8	0.0	0.0
7	control	5.6	4.4	5.0	1.0	1.0
8	out	6.3	5.0	5.6	1.3	1.3
9	clear cut	4.5	3.6	4.0	0.3	0.3
10	clear cut	5.2	4.0	4.6	0.5	0.5
11	clear cut	5.5	4.0	4.7	0.3	0.3
12	clear cut	3.9	3.6	3.8	0.1	0.1
13	clear cut	4.8	4.2	4.5	0.3	0.3
14	control	6.2	4.6	5.4	1.2	1.1
15	out	7.8	6.5	7.1	1.8	1.8
16	control	7.1	5.6	6.3	1.7	1.7
17	selection	6.2	4.8	5.5	0.6	0.6
18	shelterwood	6.7	5.5	6.1	1.4	1.3
19	shelterwood	5.6	4.0	4.8	1.0	0.9
20	selection	6.0	5.0	5.5	1.1	1.0
21	control	6.5	4.8	5.7	1.6	1.6
22	shelterwood	5.5	4.4	5.0	1.2	1.2
23	shelterwood	4.9	3.7	4.3	0.7	0.7
24	selection	5.9	4.4	5.2	0.5	0.5
25	selection	7.4	5.2	6.3	0.9	0.9
26	shelterwood	4.8	3.4	4.1	0.9	0.8
27	shelterwood	6.0	4.7	5.4	0.9	0.9
28	shelterwood	6.8	5.2	6.0	1.3	1.2
29	control	6.3	5.4	5.8	1.4	1.4
30	clear cut	4.8	3.4	4.1	0.3	0.2
31	clear cut	6.2	4.6	5.4	0.4	0.4
32	selection	7.4	5.7	6.5	1.0	1.0
33	control	8.2	6.8	7.5	2.0	2.0
34	control	6.6	5.3	6.0	1.5	1.4
35	shelterwood	6.1	4.9	5.5	1.0	0.9
36	out	6.9	5.4	6.1	1.5	1.4

A.3.3 Field Metrics - Measurements of Height

#	Treatment	Tree height (m)	Base height (m)	Crown Depth (m)
1	clear cut	13.4	2.8	10.6
2	shelterwood	19.0	8.5	10.5
3	control	16.7	7.8	8.9
4	clear cut	15.6	6.3	9.3
5	clear cut	16.3	6.1	10.2
6	clear cut	14.0	7.1	6.9
7	control	18.1	8.0	10.1
8	out	17.3	7.1	10.2
9	clear cut	15.3	7.2	8.1
10	clear cut	15.8	7.6	8.2
11	clear cut	15.4	5.2	10.2
12	clear cut	17.2	9.2	7.9
13	clear cut	13.1	5.9	7.2
14	control	17.2	6.9	10.3
15	out	19.8	9.4	10.4
16	control	18.3	8.2	10.1
17	selection	17.8	7.3	10.6
18	shelterwood	18.0	7.9	10.1
19	shelterwood	16.4	7.6	8.8
20	selection	18.1	8.7	9.4
21	control	18.0	8.6	9.4
22	shelterwood	16.3	7.4	8.8
23	shelterwood	14.6	7.6	7.0
24	selection	19.5	9.9	9.5
25	selection	18.4	8.2	10.2
26	shelterwood	16.9	8.3	8.7
27	shelterwood	16.7	8.5	8.2
28	shelterwood	16.9	7.7	9.1
29	control	17.4	8.8	8.6
30	clear cut	14.1	6.8	7.3
31	clear cut	15.2	7.3	7.8
32	selection	21.4	9.9	11.5
33	control	19.9	9.0	10.9
34	control	19.6	8.0	11.6
35	shelterwood	18.4	9.2	9.3
36	out	20.8	9.3	11.5

A.3.4 Field Metrics - Based on Number of Trees

#	Treatment	Basal Area (m^2/ha)	# Trees	Stem Density (#/ha)
1	clear cut	0.5	2.0	49.9
2	shelterwood	16.0	11.0	274.3
3	control	31.1	21.0	523.7
4	clear cut	4.3	6.0	149.6
5	clear cut	8.2	16.0	399.0
6	clear cut	0.9	1.0	24.9
7	control	18.8	18.0	448.9
8	out	20.0	19.0	473.8
9	clear cut	2.5	8.0	199.5
10	clear cut	8.5	11.0	274.3
11	clear cut	2.1	7.0	174.6
12	clear cut	1.7	3.0	74.8
13	clear cut	3.8	8.0	199.5
14	control	24.2	19.0	473.8
15	out	32.4	17.0	423.9
16	control	27.1	19.0	473.8
17	selection	8.3	10.0	249.4
18	shelterwood	18.2	16.0	399.0
19	shelterwood	13.7	20.0	498.8
20	selection	28.2	16.0	399.0
21	control	29.7	23.0	573.6
22	shelterwood	30.8	20.0	498.8
23	shelterwood	20.0	16.0	399.0
24	selection	11.6	9.0	224.4
25	selection	18.4	10.0	249.4
26	shelterwood	12.5	24.0	598.5
27	shelterwood	16.2	15.0	374.1
28	shelterwood	28.5	17.0	423.9
29	control	27.6	19.0	473.8
30	clear cut	2.8	7.0	174.6
31	clear cut	2.9	7.0	174.6
32	selection	15.0	11.0	274.3
33	control	34.4	17.0	423.9
34	control	20.2	19.0	473.8
35	shelterwood	18.4	14.0	349.1
36	out	32.6	18.0	448.9

A.4 DGPS Information

A.4.1 FH and ISD Plot Centres

FH Projection: UTM Zone 17FH Datum: WGS 84
ISD Projection: UTM Zone 18 ISD Datum: WGS84

Study Site	EASTING	NORTHING
FH A02	645759.74	5048495.00
FH A063	716543.07	4958944.73
FH A064	700505.80	4982318.38
FH A065	679128.93	4997341.99
FH A066	659720.83	4992028.98
FH A067	666661.24	5002380.17
ISD 12	458515.20	4980876.92
ISD 14	378476.62	4975366.33
ISD 15	449778.72	4949192.79
ISD 19	354164.26	4908623.72
ISD 21	490899.14	5004752.87
ISD 23	513439.24	5008704.54
ISD 3	405227.77	4955086.17
ISD 31	487943.49	5044784.66
ISD 40	467015.98	5037278.97
ISD 5	368100.05	4914876.60

A.4.2 TLW Plot Centres

TLW Projection: UTM Zone 16 TLW Datum: WGS 84

Plot #	EASTING	NORTHING
1	695365.96	5215973.40
2	695351.95	5216083.62
3	695563.48	5216068.69
4	695310.71	5215740.57
5	695388.88	5215745.37
6	695381.99	5215869.70
7	695224.75	5215851.08
8	695175.90	5215715.02
9	695302.12	5215472.29
10	695255.35	5215493.54
11	695259.34	5215538.30
12	695544.65	5215605.13
13	695527.55	5215523.66
14	695601.59	5215486.97
15	695631.71	5215614.95
16	696149.70	5215147.92
17	696184.75	5215209.36
18	696206.70	5214894.31
19	696292.17	5214829.58
20	695963.43	5214998.19
21	696043.90	5214995.31
22	695835.05	5215123.93
23	695835.04	5215198.57
24	695856.83	5215164.96
25	695877.31	5215261.26
26	696550.24	5214744.74
27	696570.39	5215330.50
28	696562.09	5215386.05
29	696151.15	5214996.35
30	695278.24	5215586.81
31	695392.25	5215662.67
32	695056.91	5215970.14
33	695119.50	5215881.51
34	695699.95	5216130.11
35	695815.12	5216305.71
36	695773.05	5215549.60

A.5 Semivariance Analysis - Optimal Extracted Range Values Per Band

Optimal Range in Metres Extracted from the Ice Storm Damage and Forest Health Plot Sites

Wavelength (nm):	409	416	424	431	438	446	453	461	468	476	483	490	498
Reflectance Image: E-W	5	5	6	7	6	7	8	7	7	9	8	6	8
1st Derivative: E-W	4	4	4	4	5	4	4	4	4	5	4	4	5
2nd Derivative: E-W	4	4	4	5	4	4	4	4	5	5	4	4	5
Reflectance Image: N-S	15	8	8	12	8	7	9	9	8	8	7	8	6
1st Derivative: N-S	5	6	9	5	7	8	5	4	4	6	6	6	6
2nd Derivative: N-S	9	6	6	10	6	5	6	6	5	4	9	5	6

Wavelength (nm):	505	513	520	528	535	543	550	558	565	573	580	588	595
Reflectance Image: E-W	9	7	7	7	7	7	7	7	7	7	7	7	7
1st Derivative: E-W	5	6	7	7	7	7	6	6	7	7	6	7	6
2nd Derivative: E-W	6	6	5	6	6	6	7	7	7	6	6	5	4
Reflectance Image: N-S	6	6	6	6	6	6	5	5	6	6	6	6	6
1st Derivative: N-S	5	6	6	6	5	6	5	6	6	6	7	7	5
2nd Derivative: N-S	8	7	5	7	5	4	6	6	5	4	5	5	3

Wavelength (nm):	603	610	618	626	633	641	648	656	663	671	679	686	694
Reflectance Image: E-W	7	8	8	8	8	7	7	8	8	8	8	8	8
1st Derivative: E-W	7	7	6	6	6	6	8	7	6	5	5	8	8
2nd Derivative: E-W	5	4	5	4	5	5	5	6	5	6	8	8	7
Reflectance Image: N-S	6	6	6	6	6	5	5	5	6	6	6	6	6
1st Derivative: N-S	5	5	6	5	5	6	6	5	5	5	8	6	6
2nd Derivative: N-S	5	3	5	3	5	4	5	5	5	6	6	7	7

Wavelength (nm):	701	709	717	724	732	739	747	755	762	770	778	785	793
Reflectance Image: E-W	7	7	7	7	7	8	7	4	8	4	4	4	4
1st Derivative: E-W	7	7	8	8	9	10	10	7	9	8	4	4	3
2nd Derivative: E-W	7	10	12	9	8	8	8	8	8	7	8	4	4
Reflectance Image: N-S	6	6	6	6	6	5	5	4	6	4	4	4	3
1st Derivative: N-S	7	6	7	7	10	11	17	5	16	8	2	2	2
2nd Derivative: N-S	8	8	15	9	6	6	7	24	6	9	7	3	3

Wavelength (nm):	801	808	816	824	831	839	847	854	862	870	878	885	893
Reflectance Image: E-W	4	4	4	3	4	4	4	4	3	4	5	4	4
1st Derivative: E-W	3	6	8	4	5	4	3	3	4	4	4	3	8
2nd Derivative: E-W	5	7	5	7	5	4	4	4	4	4	4	8	4
Reflectance Image: N-S	3	3	5	4	4	5	5	5	5	4	4	4	4
1st Derivative: N-S	2	5	7	3	3	3	3	3	3	4	3	3	7
2nd Derivative: N-S	4	5	4	6	4	3	3	2	4	3	5	6	4

Wavelength (nm):	901	908	916	924	932	939
Reflectance Image: E-W	3	4	4	4	4	5
1st Derivative: E-W	5	4	4	5	6	11
2nd Derivative: E-W	4	5	6	6	10	6
Reflectance Image: N-S	5	5	5	5	5	6
1st Derivative: N-S	5	4	6	6	7	33
2nd Derivative: N-S	4	6	7	7	33	27

A.6 CASI Image Wavelength Specifications

Number of Image Channels: 72

Units	nanometres	
Channel	Wavelength	Half-Bandwidth
1	408.7283	4.2739
2	416.1284	4.2761
3	423.5341	4.2782
4	430.9455	4.2803
5	438.3626	4.2825
6	445.7854	4.2846
7	453.2138	4.2867
8	460.6478	4.2888
9	468.0874	4.2909
10	475.5325	4.2930
11	482.9832	4.2950
12	490.4395	4.2971
13	497.9012	4.2992
14	505.3684	4.3012
15	512.8411	4.3033
16	520.3192	4.3053
17	527.8026	4.3073
18	535.2915	4.3093
19	542.7858	4.3113
20	550.2853	4.3134
21	557.7903	4.3153
22	565.3005	4.3173
23	572.8159	4.3193
24	580.3367	4.3213
25	587.8627	4.3232
26	595.3938	4.3252
27	602.9302	4.3271
28	610.4717	4.3290
29	618.0184	4.3310
30	625.5702	4.3329
31	633.1271	4.3348
32	640.6890	4.3367
33	648.2560	4.3386
34	655.8281	4.3405
35	663.4052	4.3423
36	670.9872	4.3442
37	678.5742	4.3461
38	686.1661	4.3479
39	693.7629	4.3497
40	701.3647	4.3516
41	708.9713	4.3534
42	716.5828	4.3552
43	724.1991	4.3570
44	731.8202	4.3588
45	739.4461	4.3606
46	747.0768	4.3624
47	754.7122	4.3641
48	762.3523	4.3659
49	769.9971	4.3677
50	777.6466	4.3694
51	785.3007	4.3712
52	792.9595	4.3729
53	800.6228	4.3746
54	808.2908	4.3763
55	815.9633	4.3780
56	823.6404	4.3797
57	831.3219	4.3814
58	839.0080	4.3831
59	846.6985	4.3848
60	854.3935	4.3865
61	862.0929	4.3881
62	869.7968	4.3897
63	877.5049	4.3914
64	885.2175	4.3930
65	892.9344	4.3947
66	900.6556	4.3962
67	908.3811	4.3979
68	916.1108	4.3994
69	923.8448	4.4010
70	931.5831	4.4026
71	939.3256	4.4042
72	947.0723	4.4058

A.7 Multiple Correlation Analysis Between the Field Metrics

N = 16	Crown Closure (circ)	Crown Closure (ellipse)
Crown Closure (circ)		R=0.998, p=0.000
Num Trees	R=0.71 p=0.002	R=0.69 p=0.003
Basal Area	R=0.62 p=0.011	R=0.61 p=0.013
Stem Density	R=0.67 p=0.005	R=0.66 p=0.005

n=16	DBH_{QUAD}	DBH_{ARITH}
DBH_{ARITH}	R=0.97 p=0.000	
Num Trees	R=-0.51 p=0.044	R=-0.53 p=0.033
Tree Hgt	R=0.56 p=0.025	R=0.65 p=0.007
Crown Depth	R=0.55 p=0.029	
Stem Density	R=-0.61 p=0.012	R=-0.58 p=0.019

n=16	Base Hgt	Stem Density (under-story)	Stem Density	Canopy Width (Major)	Crown Diam.
Num Trees			R=0.74 p=0.001		
Basal Area			R=0.63 p=0.008		
Tree Hgt	R=0.84 p=0.00	R=-0.58 p=0.017			
Base Hgt		R=-0.78 p=0.000			
Crown Depth				R=0.67 p=0.005	R=0.70 p=0.003

A.8 Test For Normality Of Field Data

The Shapiro-Wilk test is the most commonly used quantitative test for normality when $n<50$. If the data is normal, the value for W will be high and not significant (Shapiro *et al.*, 1968). The test uses the following hypotheses:

H_O: there is no difference between the distribution of the data set and a normal one

H_A: there is a difference between the distribution of the data set and normal

If the P-Value is below 0.05 reject the H_O.

The following field metrics where shown to approximate normal distributions according to the Shapiro-Wilk W statistic: basal area; crown depth; crown diameter, height to the crown base; LAI 5th ring, major crown width, number of trees, tree height, perpendicular crown width; quadratic DBH; stem density. The distribution of these metrics, as well as the Shapiro-Wilkes test results are shown below.

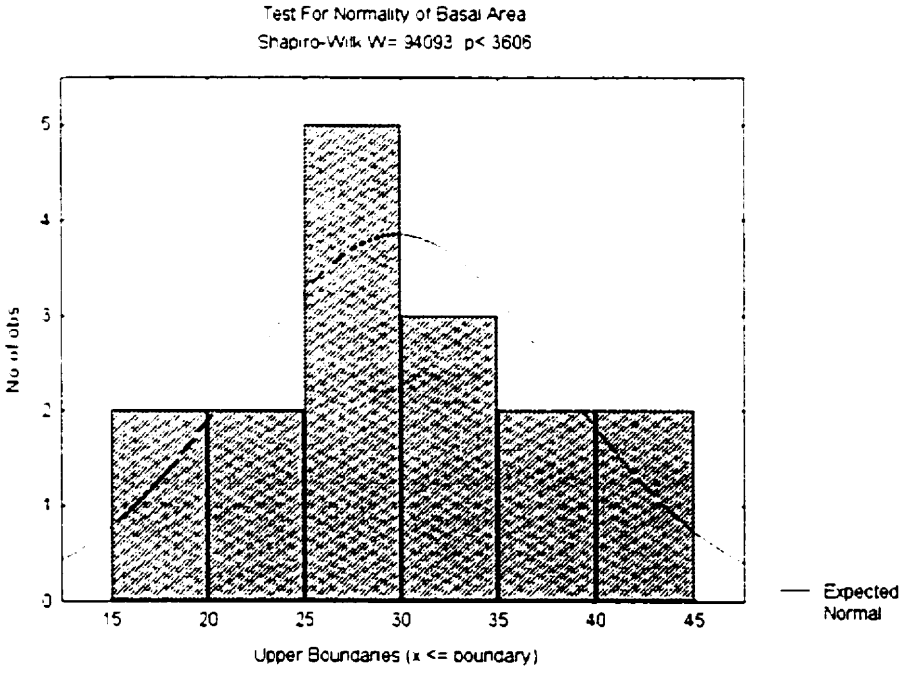

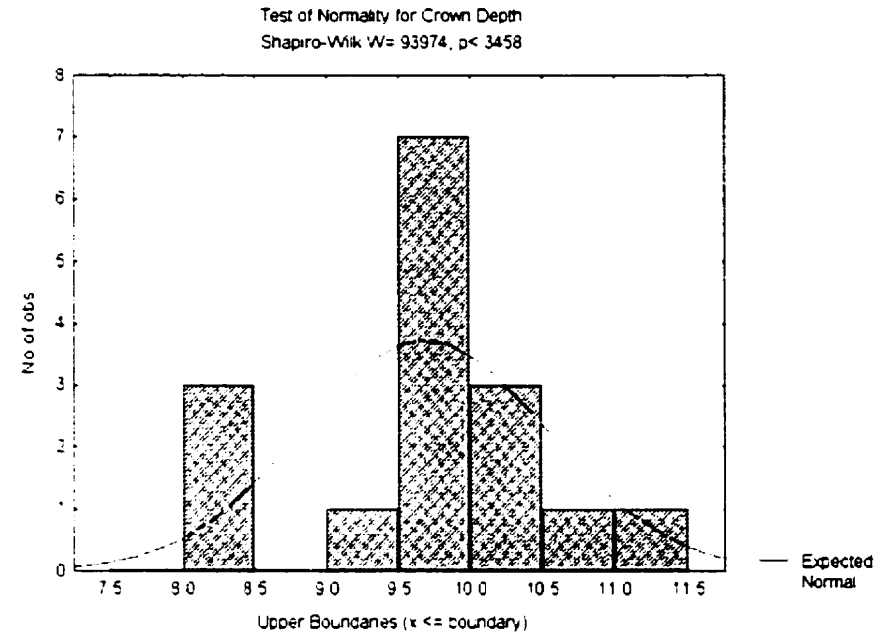
Test of Normality for Crown Depth
Shapiro-Wilk W= 93974, p< 3458
No of obs
0
1
2
3
4
5
6
7
8
75
80
85
90
95
100
105
110
115
Upper Boundaries (x <= boundary)
Expected
Normal

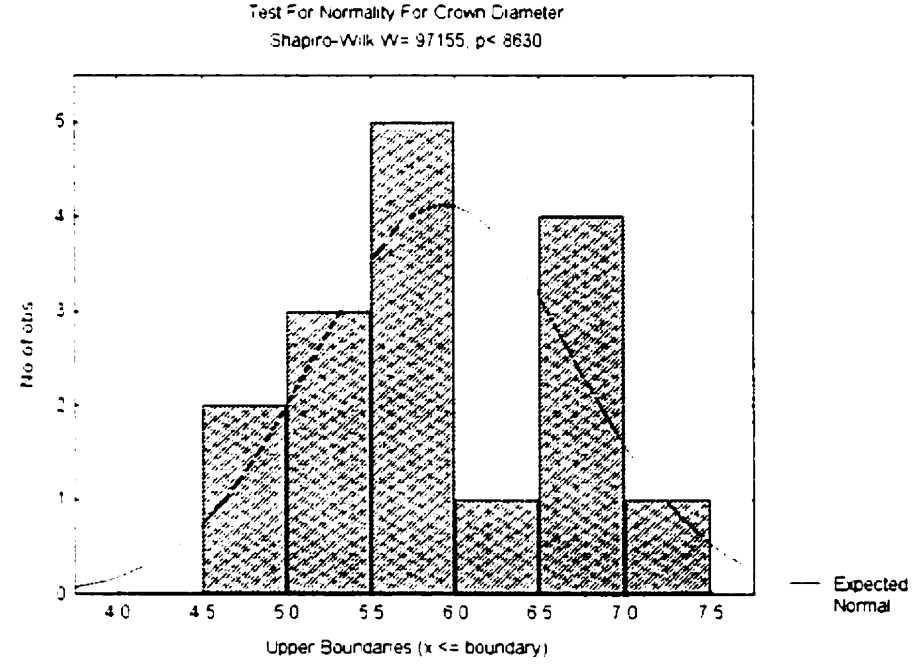
Test For Normality For Crown Diameter
Shapiro-Wilk W= 97155, p< 8630
No of obs
0
1
2
3
4
5
40
45
50
55
60
65
70
75
Upper Boundaries (x <= boundary)
Expected
Normal

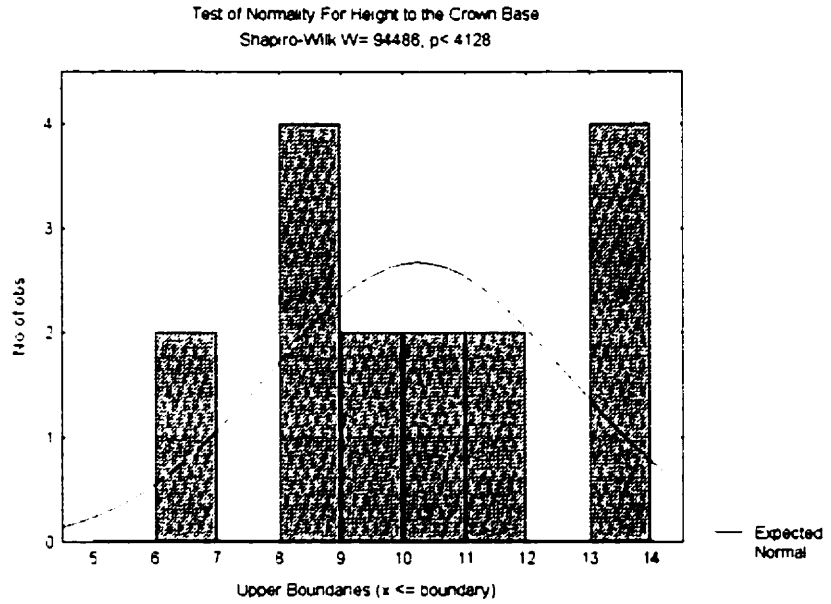
Test of Normality For Height to the Crown Base
Shapiro-Wilk W= 94486, p< 4128
No of obs
0
1
2
3
4
5
6
7
8
9
10
11
12
13
14
Upper Boundaries (x <= boundary)
Expected
Normal

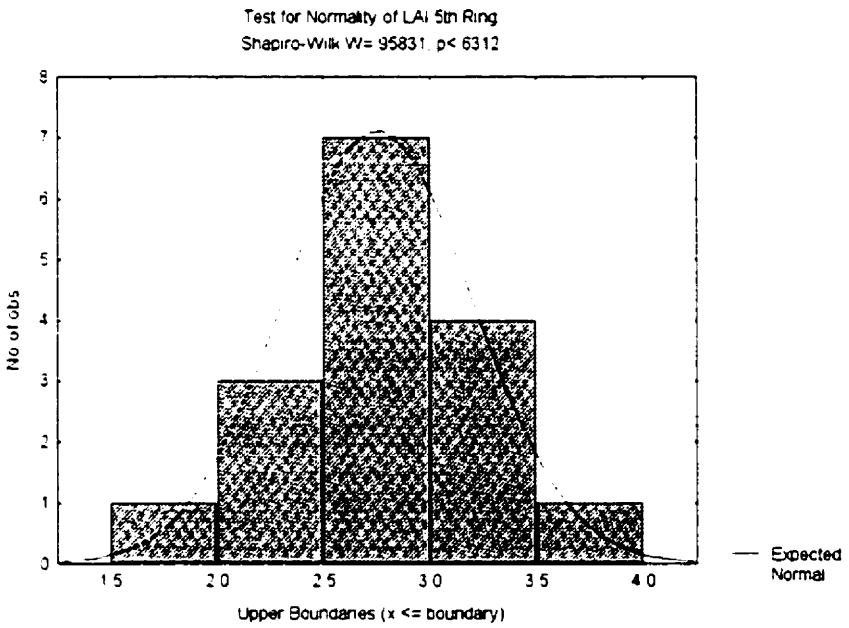
Test for Normality of LAI 5th Ring
Shapiro-Wilk W= 95831, p< 6312
No of obs
0
1
2
3
4
5
6
7
8
15
20
25
30
35
40
Upper Boundaries (x <= boundary)
Expected
Normal

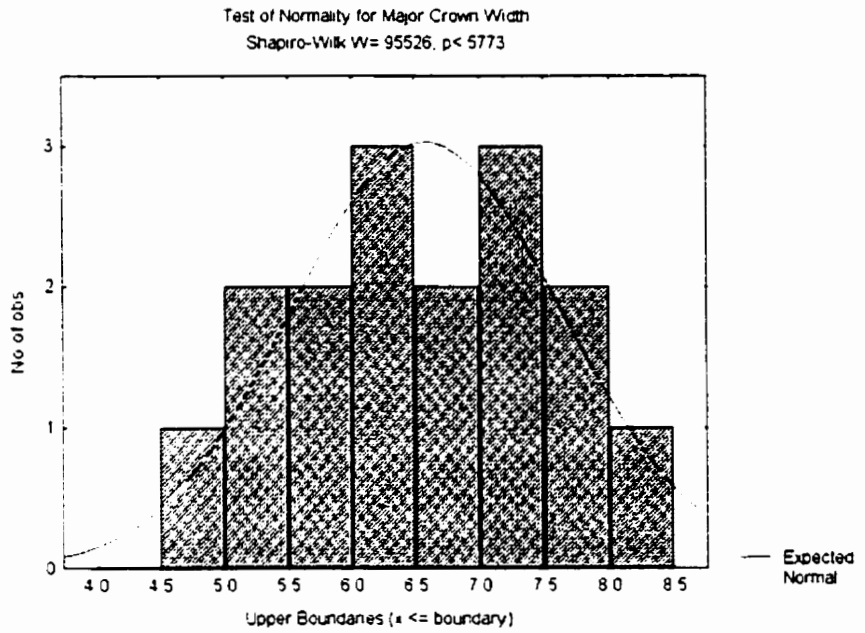
Test of Normality for Major Crown Width
Shapiro-Wilk W= 95526, p< 5773
No of obs
0
1
2
3
40
45
50
55
60
65
70
75
80
85
Upper Boundaries (x <= boundary)
Expected
Normal

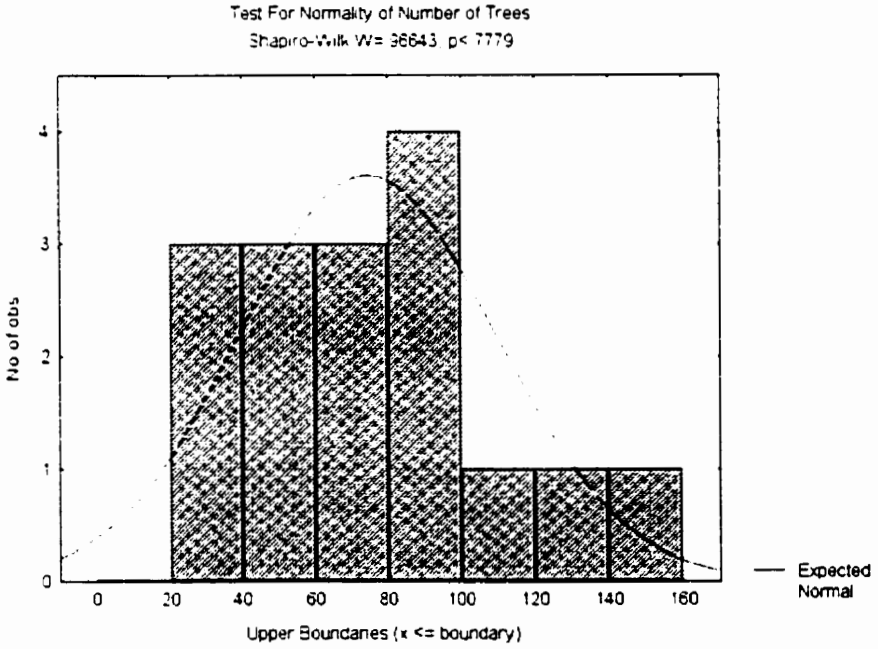
Test For Normality of Number of Trees
Shapiro-Wilk W= 86643, p< 7779
No of obs
0
1
2
3
4
0
20
40
60
80
100
120
140
160
Upper Boundaries (x <= boundary)
Expected
Normal

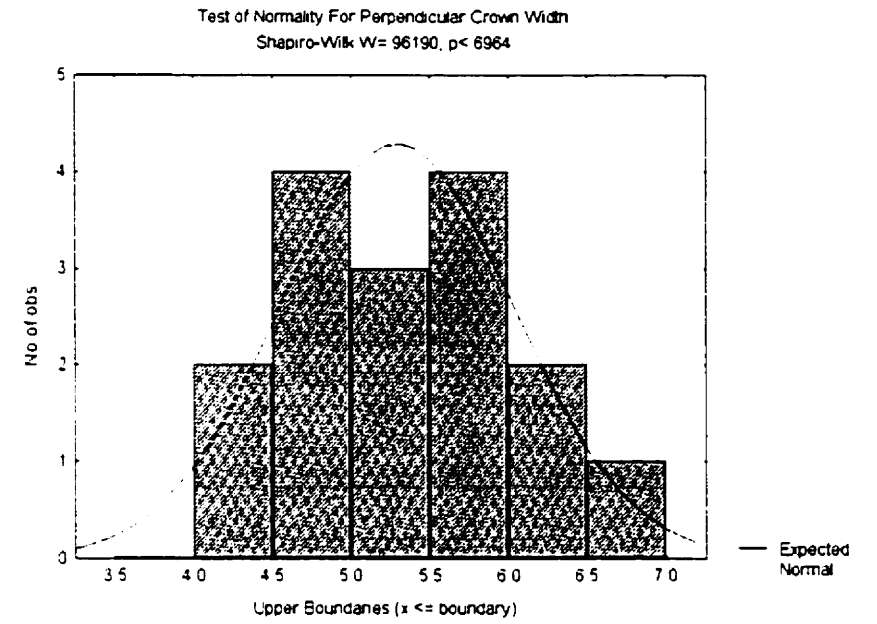
Test of Normality For Perpendicular Crown Width
Shapiro-Wilk W= 96190, p< 6964
No of obs
0
1
2
3
4
5
35
40
45
50
55
60
65
70
Upper Boundaries (x <= boundary)
Expected
Normal

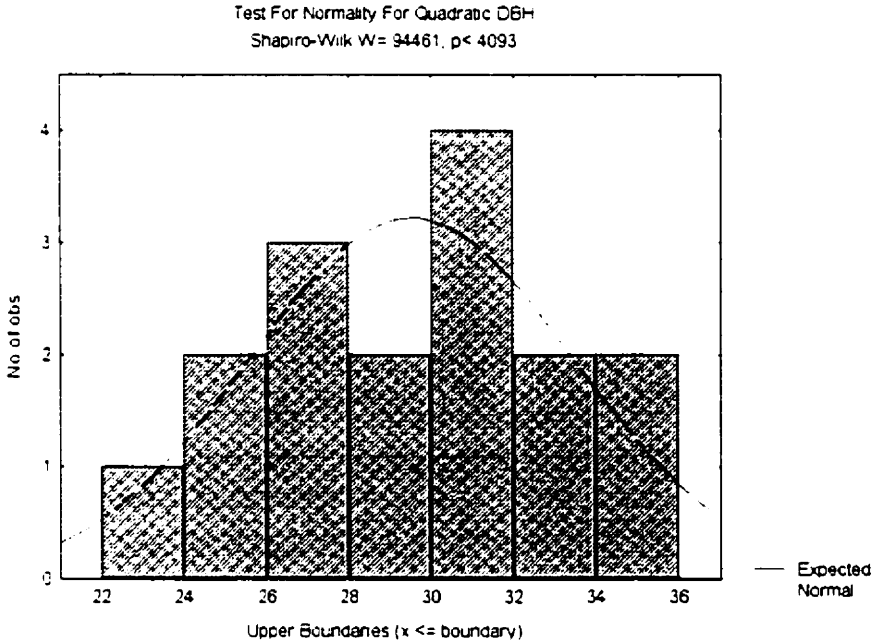
Test For Normality For Quadratic DBH
Shapiro-Wilk W= 94461, p< 4093
No of obs
0
1
2
3
4
22
24
26
28
30
32
34
36
Upper Boundaries (x <= boundary)
Expected
Normal

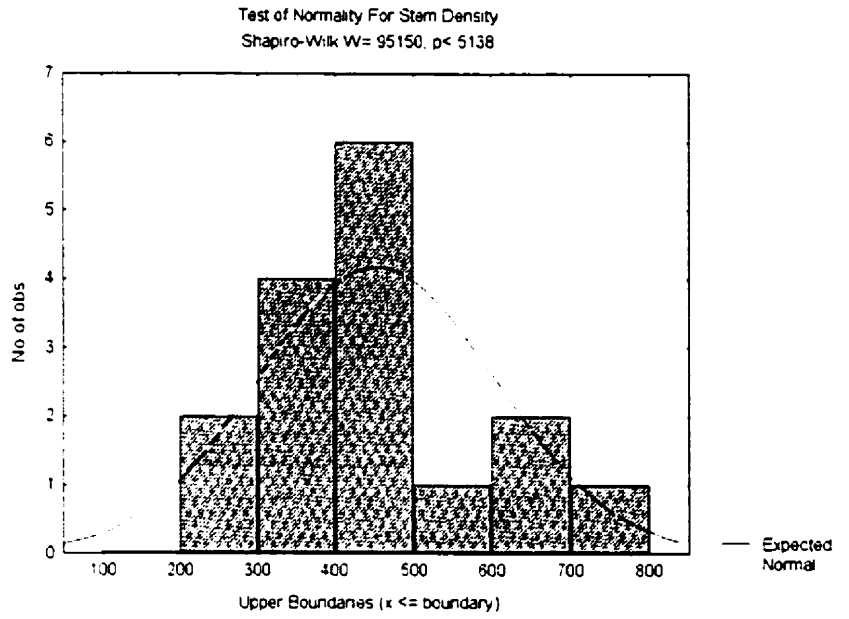
Test of Normality For Stem Density
Shapiro-Wilk W= 95150, p< 5138
No of obs
0
1
2
3
4
5
6
7
100
200
300
400
500
600
700
800
Upper Boundaries (x <= boundary)
Expected
Normal

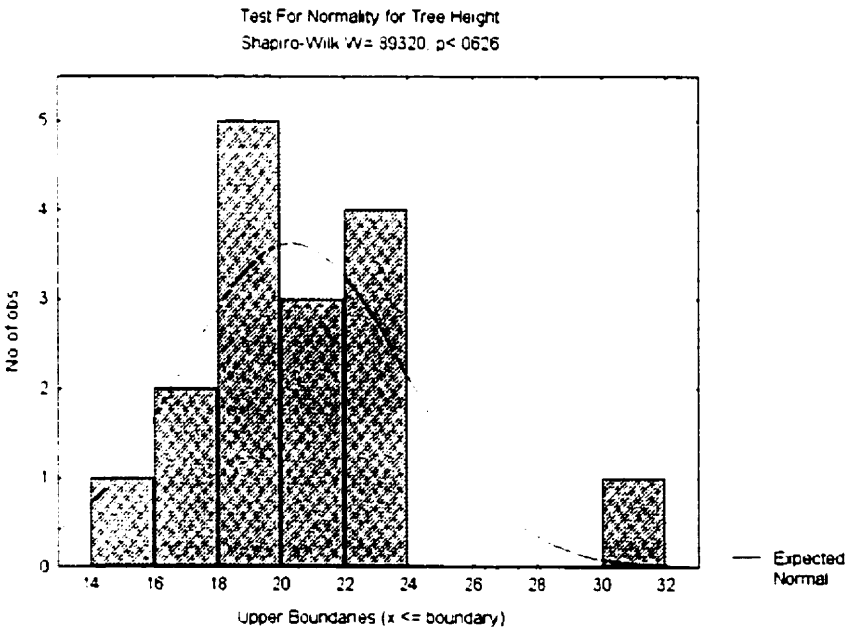
Test For Normality for Tree Height
Shapiro-Wilk W= 89320, p< 0626
No of obs
0
1
2
3
4
5
14
16
18
20
22
24
26
28
30
32
Upper Boundaries (x <= boundary)
Expected
Normal

A8.1 Field Data Requiring Transformations

The following field metrics were shown not to approximate normal distributions: circular crown closure; elliptical crown closure; LAI 4th ring; and percent canopy openness. The original distributions and the transformed normalized distributions are shown below.

Circular Crown Closure

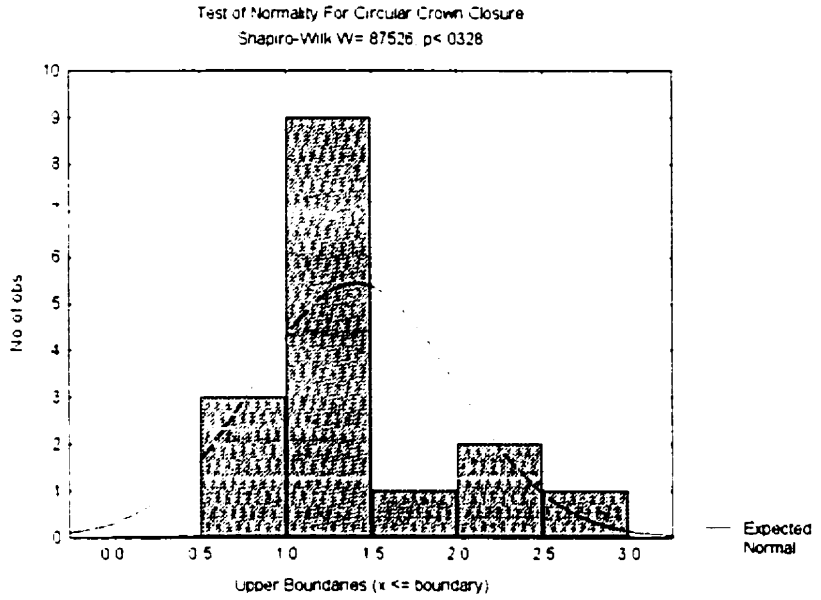

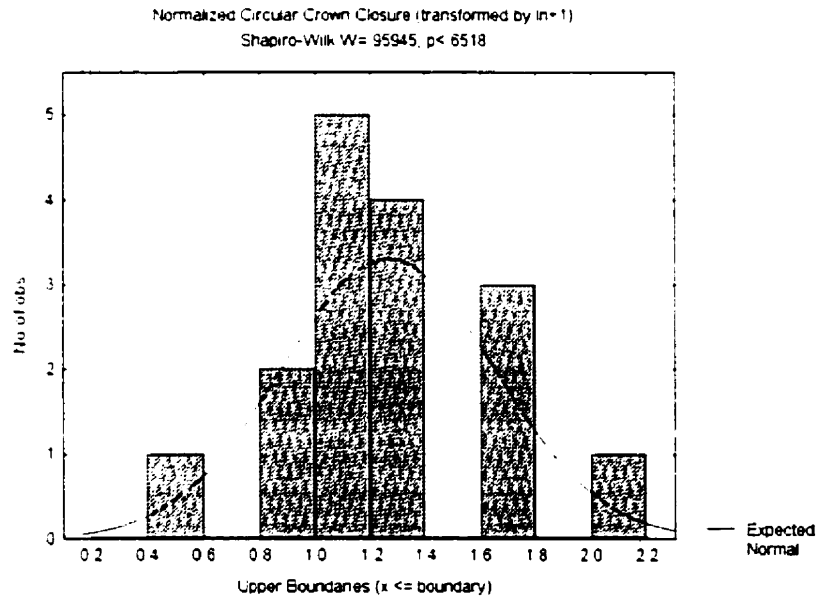

Percent Canopy Openness

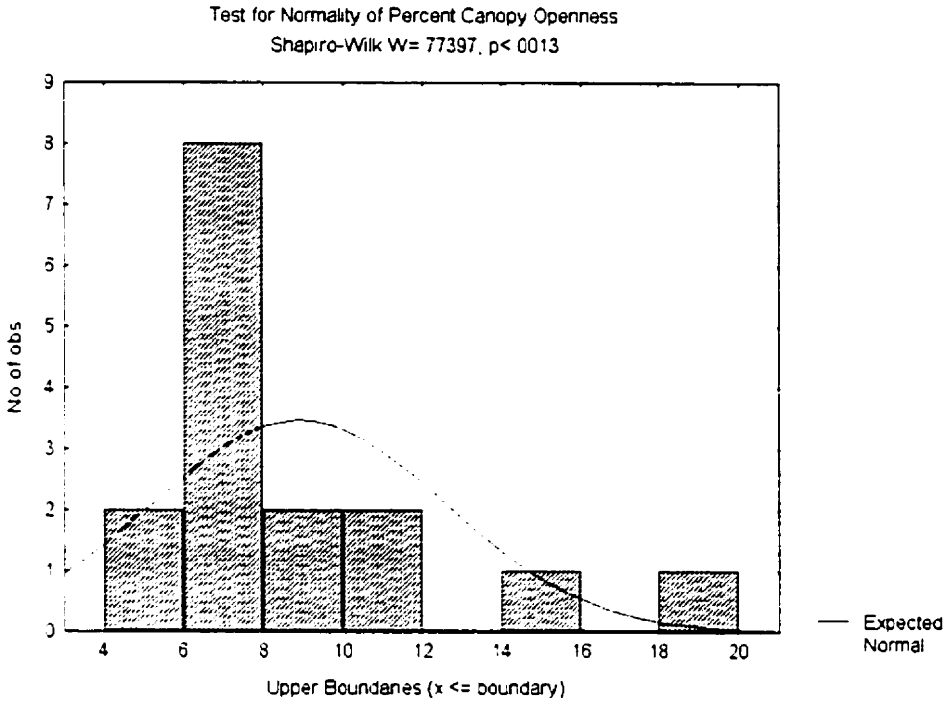

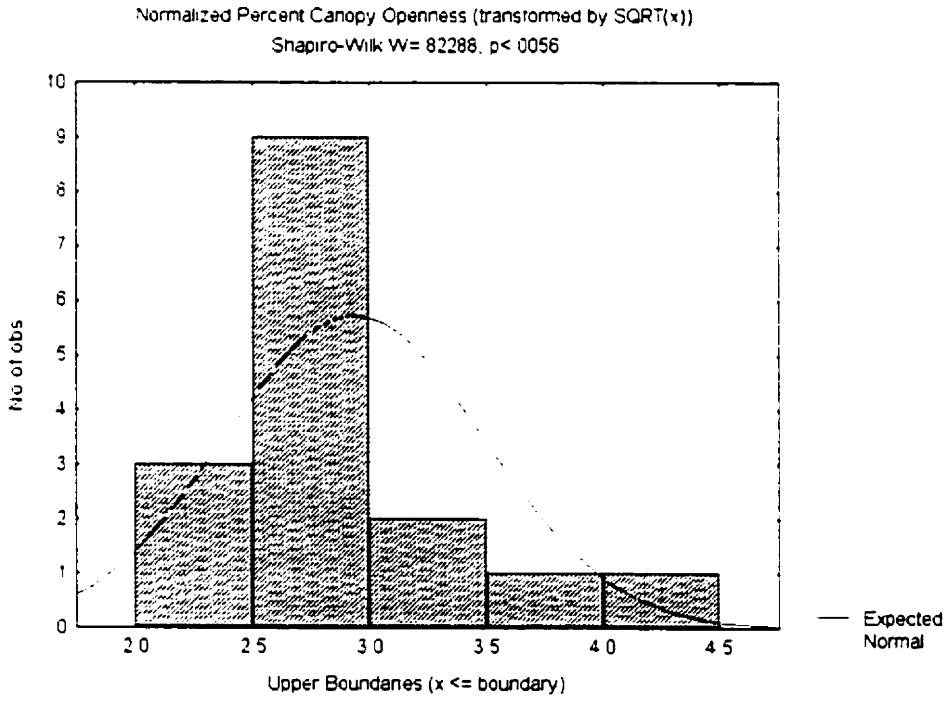

LAI 4th Ring

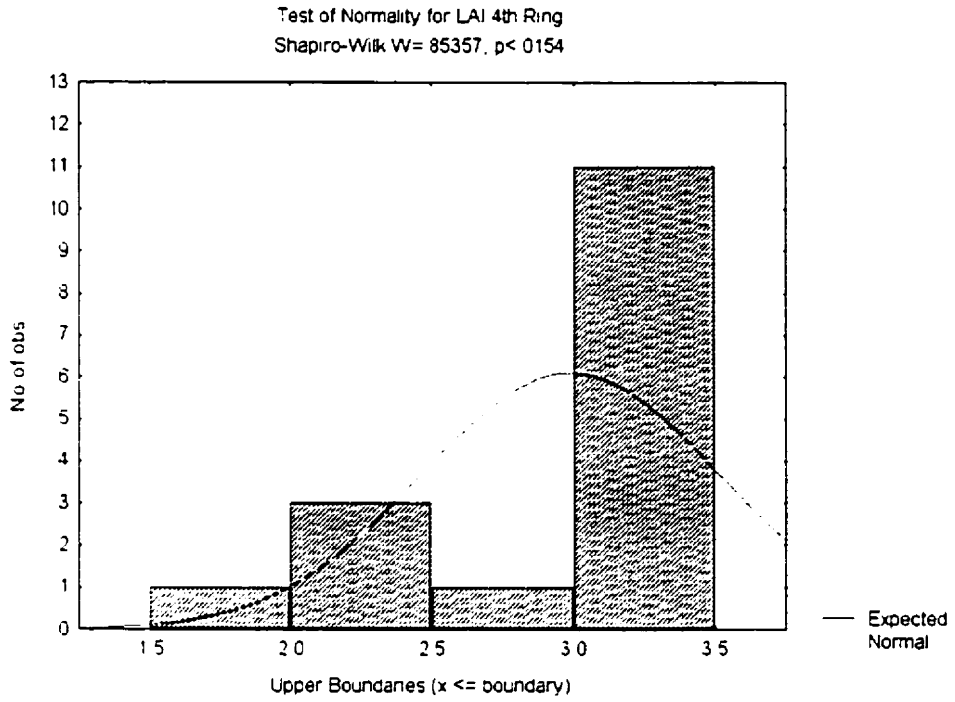
Test of Normality for LAI 4th Ring
Shapiro-Wilk W= 85357, p< 0154
No of obs
Upper Boundaries (x <= boundary)
Expected
Normal

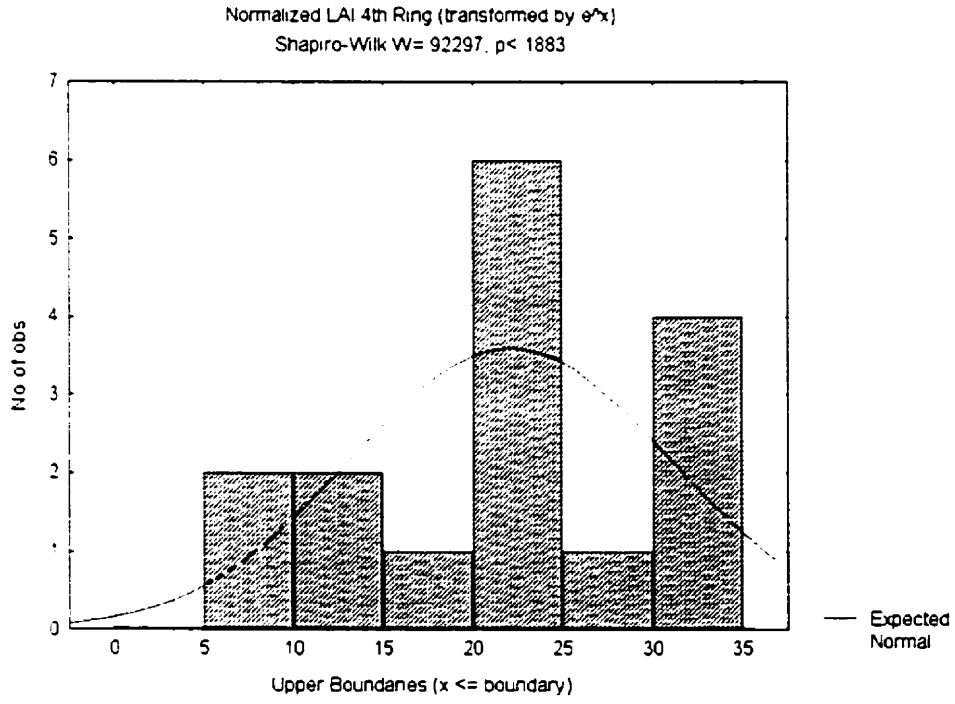
Normalized LAI 4th Ring (transformed by e^x)
Shapiro-Wilk W= 92297, p< 1883
No of obs
Upper Boundaries (x <= boundary)
Expected
Normal

Elliptical Crown Closure